

**Metallurgical Process Simulation Laboratory
Department of Mechanical and
Industrial Engineering
University of Illinois at
Urbana-Champaign
Urbana, IL 61801**



MPSL-88-01

APPLICATION OF MATHEMATICAL MODELS TO INVESTIGATE DEFECT FORMATION DURING HOT-CHARGING OF CONTINUOUSLY-CAST STEEL SLABS

**Glen Haegele
and
Brian G. Thomas**

**Final Report to
Engineering Foundation
345 East 47th Street
New York, NY 10017
for Research Conducted under
Grant RI-A-86-4**

September 1988

ACKNOWLEDGEMENTS

The authors would like to thank the Engineering Foundation (AIME) for their support of this research project. Additional thanks is extended to the staff of the National Center for Supercomputer Application who provided time on the ALLIANT and CRAY-XMP/48 computers for some of the mathematical model runs. Finally, the work of Bill Storkman in development of the programs is also acknowledged.

TABLE OF CONTENTS

	PAGE
INTRODUCTION.....	1
1. PREVIOUS WORK.....	6
1.1 CONTINUOUS CASTING SIMULATIONS.....	6
1.2 STRESS MODELS.....	11
1.3 METALLURGICAL DEFECTS.....	12
1.4 HOT CHARGING.....	18
2. MODEL DEVELOPMENT.....	20
2.1 HEAT TRANSFER FORMULATION.....	20
2.2 STRESS FORMULATION.....	26
2.3 OVERALL SIMULATION PROCEDURE.....	33
2.4 POSTPROCESSING.....	35
3. MODEL VERIFICATION.....	38
4. APPLICATION TO HOT CHARGING.....	44
4.1 MATERIAL PROPERTIES.....	49
4.2 BOUNDARY CONDITIONS.....	54
5. SIMULATION RESULTS.....	67
5.1 MOLD.....	67
5.2 SPRAYS.....	70
5.3 TRANSFER.....	82
5.4 REHEAT.....	97
5.5 DISCUSSION.....	108
6. CONCLUSION AND RECOMMENDATIONS.....	117

REFERENCES.....	120
------------------------	------------

APPENDICES

A: Analytical solution to verification problem.....	125
B: Location of rollers.....	133
C: Determination of roll contact.....	136
D: Natural convection calculations.....	139

INTRODUCTION

Continuous slab casting has emerged as the premier process for economic large scale production of quality steel in the world. As shown in Figure 1, the fraction of steel produced in the United States via continuous casting has increased from 12.5 percent in 1977 to over 55 percent in 1986. [1] To save energy and increase productivity, many companies are implementing or considering the further process of "hot charging." Thus, there is a growing need to find optimum operating conditions for the hot charging process and to understand their relationship to steel quality.

The process of continuous casting of steel slabs using hot charging involves several steps, illustrated in Figure 2. The liquid steel is poured from the ladle (50-200 tons) into a small reservoir (10 - 25 tons), called a tundish. The steel then passes through ceramic shrouds attached to the tundish bottom and out a bifurcated, submerged nozzle into the mold. The water-cooled, copper walls of the mold extract heat from the molten steel, forming a thin shell around the liquid core. This shell is slowly extracted from the mold and cools in the spray zones as it is guided and supported by rollers. Both the water flux (or recently "air-water mist") and the rolls extract heat from the steel surface. Because the steel solidifies in an arc, initiating in the generally curved walls of the mold, some of the later rolls in the casting machine must unbend the metal strand to straighten it.

After the steel has completely solidified, the strand is then cut into individual slabs of roughly 15 meters in length. With conventional continuous casting, the slabs are then allowed to cool in an open area of the steelmaking shop. When enough slabs have accumulated, they are usually

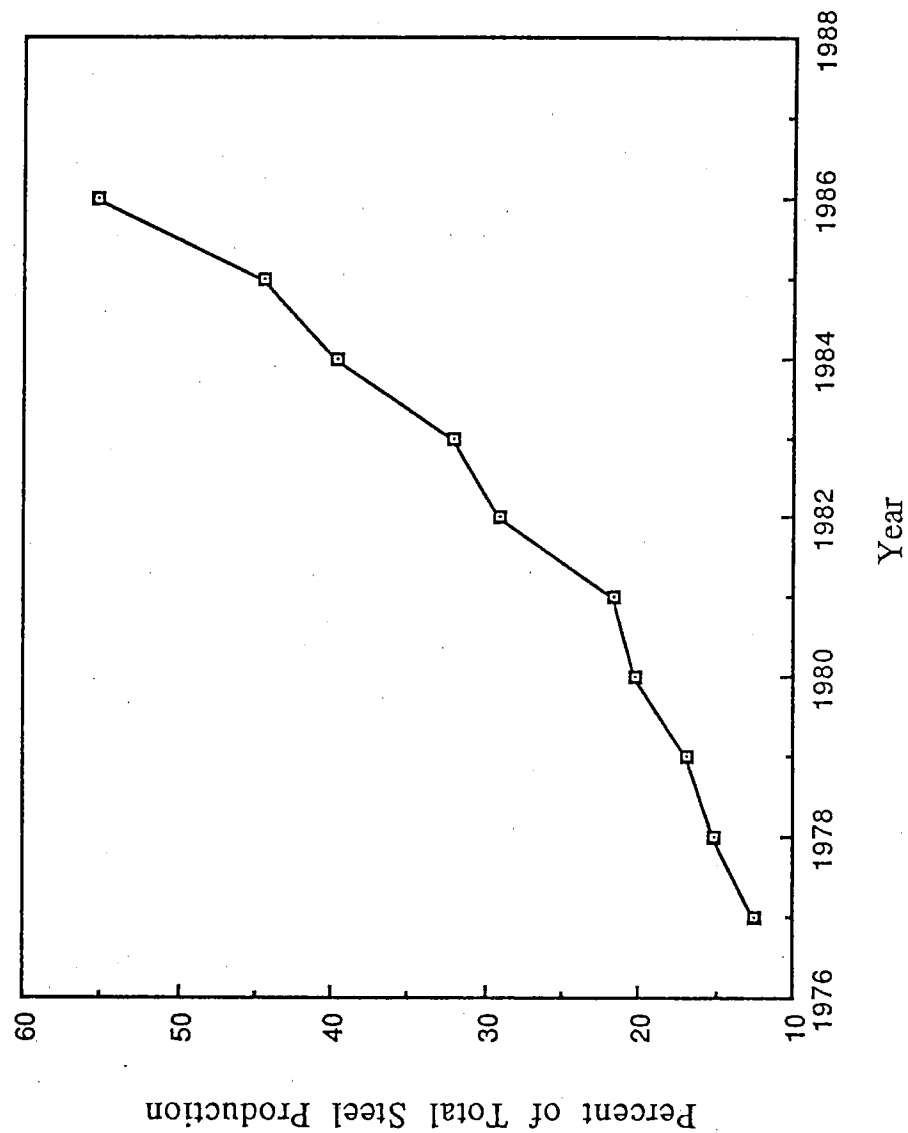


Figure 1. Graph showing percentage of steel produced by the continuous casting process in the United States for the past 10 years.

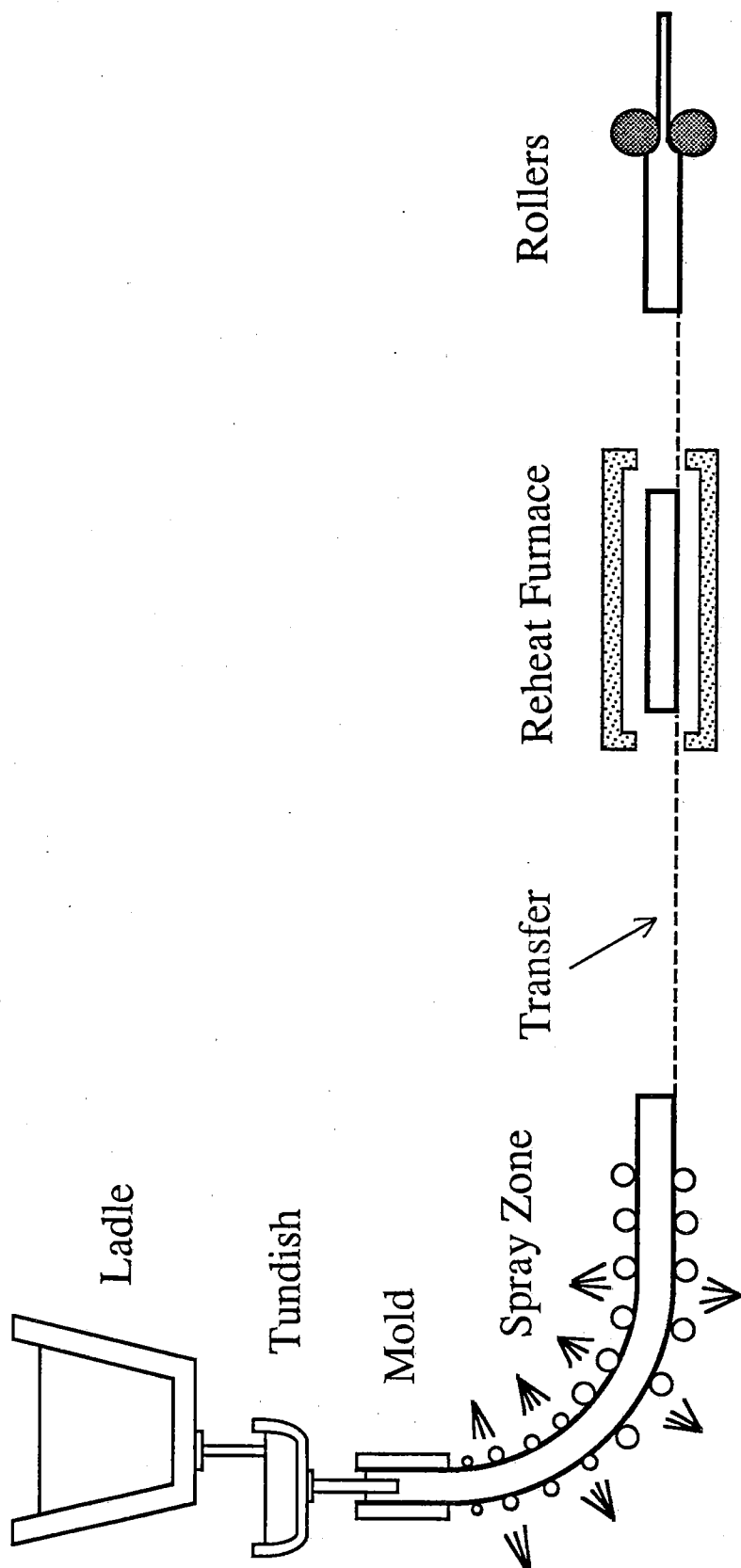


Figure 2. Schematic diagram showing the different stages of the continuous casting/hot charging process

transferred by rail car to the rolling mill. Along the way, the slabs may wait in a switching yard, and may end up quite cold. Prior to rolling, the slabs are reheated in a furnace to the uniform high temperatures required for rolling.

However, the process of hot charging attempts to keep the slab as hot as possible. After exiting the casting machine and the torch cut-off, the slab is transported to the reheating furnace as fast as possible, usually using an insulated transfer car. This process should be distinguished from direct rolling, in which only the edges of the slab are reheated prior to rolling, and the reheat furnace is eliminated from the process.

Through hot charging, the slab retains much of its thermal energy, and the furnace uses less energy. Energy savings in excess of 300% have been reported [2]. Also, the process reduces handling costs and increases productivity. For example, approximately 100 hours are needed to process a cold charged slab from tapping of the ladle to coiling of the final product, whereas a hot charged slab requires only 6 hours [3]. However, these benefits can only be achieved if product quality is maintained.

Unfortunately, the continuously-cast strand is subject to a variety of defects, ranging from cracks and depressions that arise in the mold region to defects that initiate much later in the process. Transverse facial cracks or longitudinal cracks may not be detected prior to rolling, due in part to the limited time available for inspection during the hot charging process. The steel must be reconditioned, and may be scrapped if the defects are too serious. These defects arise through a combination of tensile stresses and reduced hot ductility in the solidifying shell. The tensile stresses may arise from initial solidification in the mold, bulging of the shell between support rollers, from

the unbending of the slab, and from the high and rapidly changing temperature gradients arising within the slab during cooling. The metallurgical aspects of reduced high temperature ductility have been the subject of several recent studies, reviewed in [4]. However the generation of stresses in the steel shell has received relatively less attention. This lack of attention is not due to a failure to recognize the importance of the stresses but is an indication of the complexity of the problem. Only with the advent of recent sophistication of finite element methods and the existence of large computational facilities is the problem now feasible to tackle.

In an attempt to address this problem, the present research develops and utilizes a finite element model which can predict temperature, strain, and stress development within the steel strand from the onset of solidification in the mold, through all processing stages until the start of hot rolling. The model simulates a two-dimensional, transverse slice of the strand, allowing the effects of the narrow face to be examined more closely. The simulation includes solidification in the mold, cooling of the strand by the water sprays and rollers in the casting machine, cooling of the slab during transfer, and reheating of the slab in the furnace prior to rolling. This simulation does not directly include the strain caused by the unbending of the strand, or by the bulging of the strand between the rollers. By examining different cooling practices and handling sequences, this project aims to elucidate the potential role of thermal stresses in defect formation during the hot charging process. As a side benefit, the model allows improved understanding and prediction of other casting parameters of interest, such as ideal machine taper. The goal is to find processing parameters for continuous slab casting and hot charging that save energy while avoiding potential problems.

1. PREVIOUS WORK

1.1 CONTINUOUS CASTING HEAT FLOW SIMULATION

Several models have been developed to simulate the continuous casting process. These efforts have focussed mainly on predicting heat transfer within the slab in the mold region and secondary cooling zones. They are briefly summarized below.

The mold region of the continuous caster clearly has a great influence on steel quality. Accordingly, very extensive research has been conducted in this area [5-10]. These analyses have included effects such as gap formation, mold distortion, mold powder influences, liquid pool convection, and ferrostatic pressure. Because of the scope and complexity of these effects, they will not be discussed in detail here. The present work uses the results from concurrent research which investigates the mold in much greater detail.

Substantial research has also gone into modelling heat transfer in the secondary cooling spray zones. To characterize heat transferred by water jets impinging on the hot steel surface, several studies involved monitoring a heated plate being sprayed with various nozzle configurations [11-13]. A correlation was then found for the heat transfer coefficient of the water spray. These findings have been tabulated elsewhere [14]. Some important conclusions can be made from these investigations. The spray water flux (l/m^2s) has the largest effect on the heat transfer coefficient, whereas the spray water temperature has little effect [11]. The highest heat transfer occurs when the surface becomes "wetted". Above a critical temperature, known as the Leidenfrost temperature, a stable water vapor layer forms, which shields the slab surface from direct impingement

of the water sprays. This transition from the stable layer to the wetted surface is quite unstable and can produce sharp cooling in certain areas where the vapor layer has been penetrated. This penetration is readily visible as dark spots form on the surface where wetting has occurred, and are unstable in time and location [11]. Jacobi et al reports that the Leidenfrost transition occurs over a wider temperature range than was reported by Mizikar [12]. In any case, this condition should be avoided to eliminate the high localized stresses associated with the sudden heat transfer change due to wetting.

"Air mist" cooling is also being examined as an efficient, more uniform means of cooling the strand surface [3,11,13]. This method of spraying an air-water mixture, combined with smaller spraying angles, helps avoid the cracking problems associated with uneven cooling, while not appreciably affecting the amount of heat removed from the surface. This also has the side benefit of helping to reduce effluent and backwater buildup in the roller gap [11], and prevents overcooling of edges since little water flows down the slab edge as in conventional water sprays. Surface temperature fluctuations have been shown to decrease by one-fourth using "air-mist" cooling [15]. Lastly, the air-water mixing arrangement within the nozzle allows larger nozzle openings, reducing the chance of clogging [16], requiring fewer nozzles and thus reduced maintenance.

The interaction of cooling sprays and support rollers on heat transfer from the slab has also been examined. Wiesinger et al [17] used a finite difference heat transfer model to determine the different percentages of heat extracted by each heat transfer mechanism (i.e. direct spraying, radiation, roll contact, etc.). These percentages were back-calculated from thermocouple measurements from an operating caster. These measurements showed a double peak in the surface temperature between the rollers. This is illustrated

schematically in Figure 3. The middle valley is caused by the direct spray impingement. The second peak is lower than the first; this is likely caused by the accumulation of water ahead of the roller. These large temperature swings are confined to a thin surface layer, and thus are important when analyzing surface cracking. Wiesinger also emphasized the importance of the two-dimensional (i.e. transverse slice) modeling of the heat flow and its corresponding acceleration of solidification in the last stages. This leads to increased shrinkage and thus increased strain and stress near the crater end (metallurgical length of the caster).

Etienne et al [18], using a laboratory model, calculated the different heat extraction percentages of the various mechanisms. These data were then used in a two-dimensional, explicit finite difference model. The resulting shell thickness and surface temperatures were found to agree well with industrial measurements.

Other research into the interaction of the rollers and sprays have shown reversed trends from Wiesinger above. Krüger et al [15] also measured the strand surface temperature, but found the strand to be coldest under the water sprays. The strand was hottest in the roller "shadow" zone area where the roller shades the strand from the water spray, with roller cooling accounting for 20-60% of the heat removal.

Kojima et al [19] also reported the trends observed by Krüger above. Heat loss to the roll was cited at 30-60% of all heat loss between rolls. Thermocouple measurements from the slab surface were used in a two-

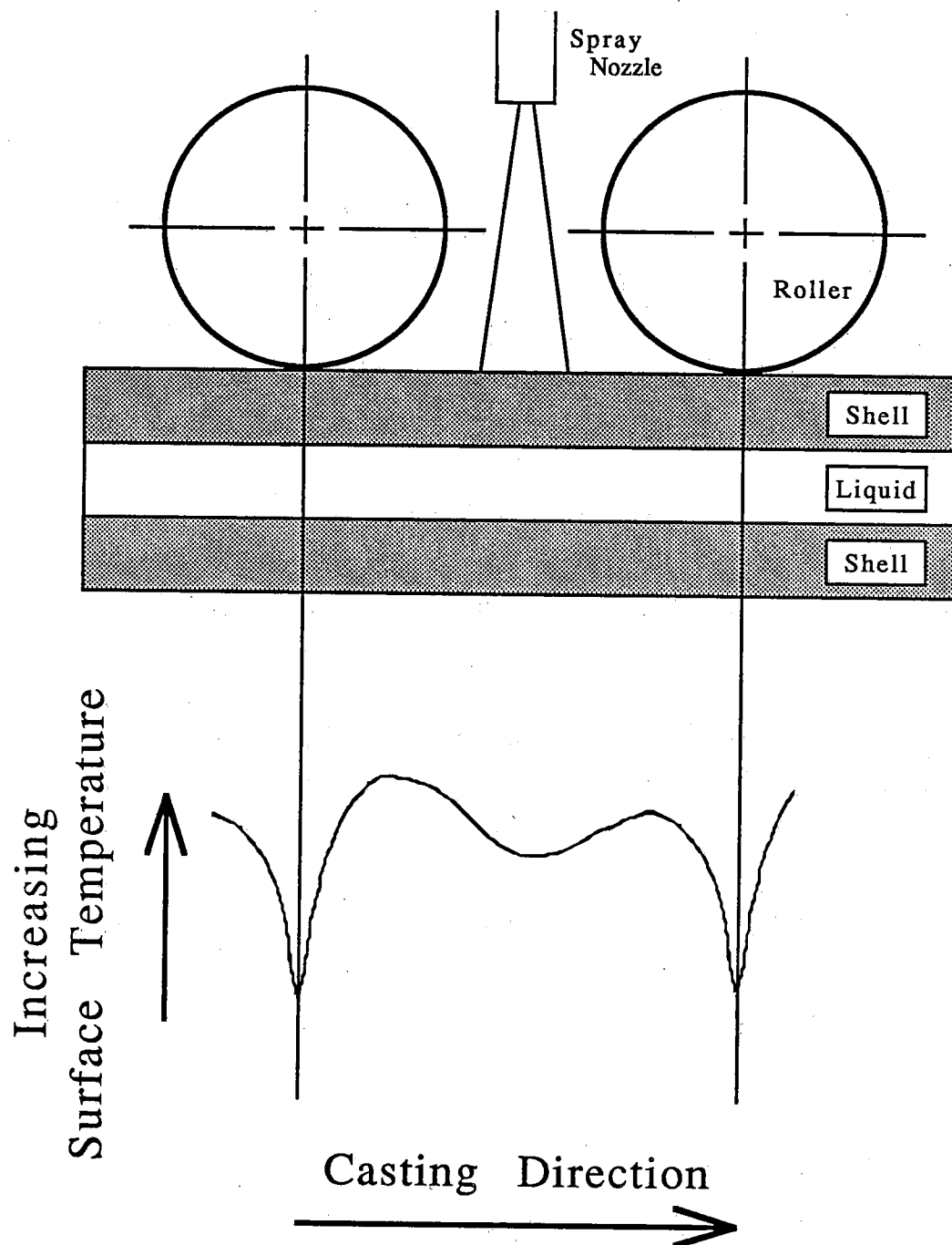


Figure 3. Illustration of typical surface temperature as strand passes under the rollers and cooling sprays.

dimensional, explicit finite difference model to obtain the heat flux out of the surface. The strand was coldest under the water sprays, with the roll contact region composed of three zones: residual water, roll contact, and leaking water.

Hibbins et al [20] examined the heat transfer in the spray zones. A one-dimensional mathematical model analyzed actual surface temperatures to get average heat transfer coefficients. These were then correlated to an average spray water flux for each of the five zones of the caster examined. The percentages of heat extracted by each of the heat transfer mechanisms (roll contact, direct spray, radiation, convection) were also calculated. As expected, direct spraying accounted for virtually all of the heat removal high in the caster, but contributes moderately in the later zones. Radiation and roll contact increase their heat removal as the strand progresses through the caster. These trends match those reported by Wiesinger above, but differ in magnitude, exemplifying the uniqueness of the heat transfer in the secondary cooling zone between continuous casting machines.

A solidification model was developed by Davies et al [21] which analyzes the mold and spray zones of the caster and their roles in shell growth. The one-dimensional heat transfer model included the latent heat due to solidification, temperature-dependent material properties, convection heat transfer in the liquid, and solute redistribution. The mold region used a mold heat flux equation based on a finite element analysis of thermocouple measurements from an operating mold. The spray zone heat transfer was based on an average heat transfer coefficient. Actual surface temperatures were inputted to an iterative-type program to find a heat transfer coefficient which produced matching temperatures. It was emphasized that this coefficient is very caster-dependent.

Finally, a mold and caster thermal simulation was performed by Upton et al [22]. This model used a mold heat flux equation very similar to the classic Savage and Pritchard relationship [23]. A correlation for the water spray heat transfer coefficient was used, similar to those discussed previously. The coefficients for the roll contact region were calculated separately from Etienne above. These were used in a one-dimensional, finite difference model which evaluated the surface temperature and shell growth of a strand. The model included the liquid pool convection, as well as the roll/spray interaction. The model accurately predicted the large temperature swings that occur on the strand surface. Narrow face effects on the temperature distribution and the metallurgical length were not available due to the one-dimensional assumption.

1.2 CONTINUOUS CASTING STRESS MODELS

All of the previous research has been concerned with the heat flow during the casting process. However, demand for higher productivity and higher casting speeds have made it necessary to bend the strand before it is completely solidified. Recent research into the strain distribution and deformation of the cast shell during unbending has shown how important this area is to the development of internal cracks. These cracks are caused by straining the steel liquid/solid interface while it has reduced ductility, commonly referred to as "hot tearing". The crack opens up and is penetrated by solute-rich liquid steel, thus causing an internal defect described as "radial streaks".

Uehara et al [24] modeled a two-dimensional slice through the center of the wide face with an elasto-plastic finite element model to predict the strain distribution during both bending and bulging of the strand. Results from the slice model were compared to an elastic three-dimensional simulation to verify its

validity. The residual stresses in the strand prior to straightening were considered negligible. The analysis showed that the bulging strain and bending strain during straightening can combine to produce tensile stresses that cause cracking, particularly in the weak newly-solidified steel at the inside of the shell. To avoid this problem, some Japanese steel plants have adopted "compression casting", whereby the drive rolls purposely attempt to produce compressive stresses at the crack-sensitive solidifying interior. [2] Several researchers have used the finite element method to model the cast strand, focussing on bulging between two sets of rollers. For example, Barber et al [25] developed a three-dimensional model and found that the bulge was non-symmetric, with the maximum bulge arising closer to the trailing (lower) roller. Both analyses showed that predicting the strain distribution during straightening is quite complicated due to the three-dimensional nature of this problem.

1.3 METALLURGICAL DEFECTS

Before examining the various defect problems found in continuously cast steel slabs, it is helpful to summarize the different ductility problems in steels at high temperature. This loss of ductility combined with tensile stress can lead to crack formation. The temperature zones of reduced ductility and the associated embrittling mechanisms are illustrated schematically in Figure 4, and will be briefly discussed. [4]

At high temperatures, (Zone A) just below the solidus, a severe loss in ductility arises, resulting in "hot tearing" if only a few percent tensile strain is imposed. This embrittlement zone is due to segregation of phosphorus and sulfur to the inter-dendritic regions during solidification and results in

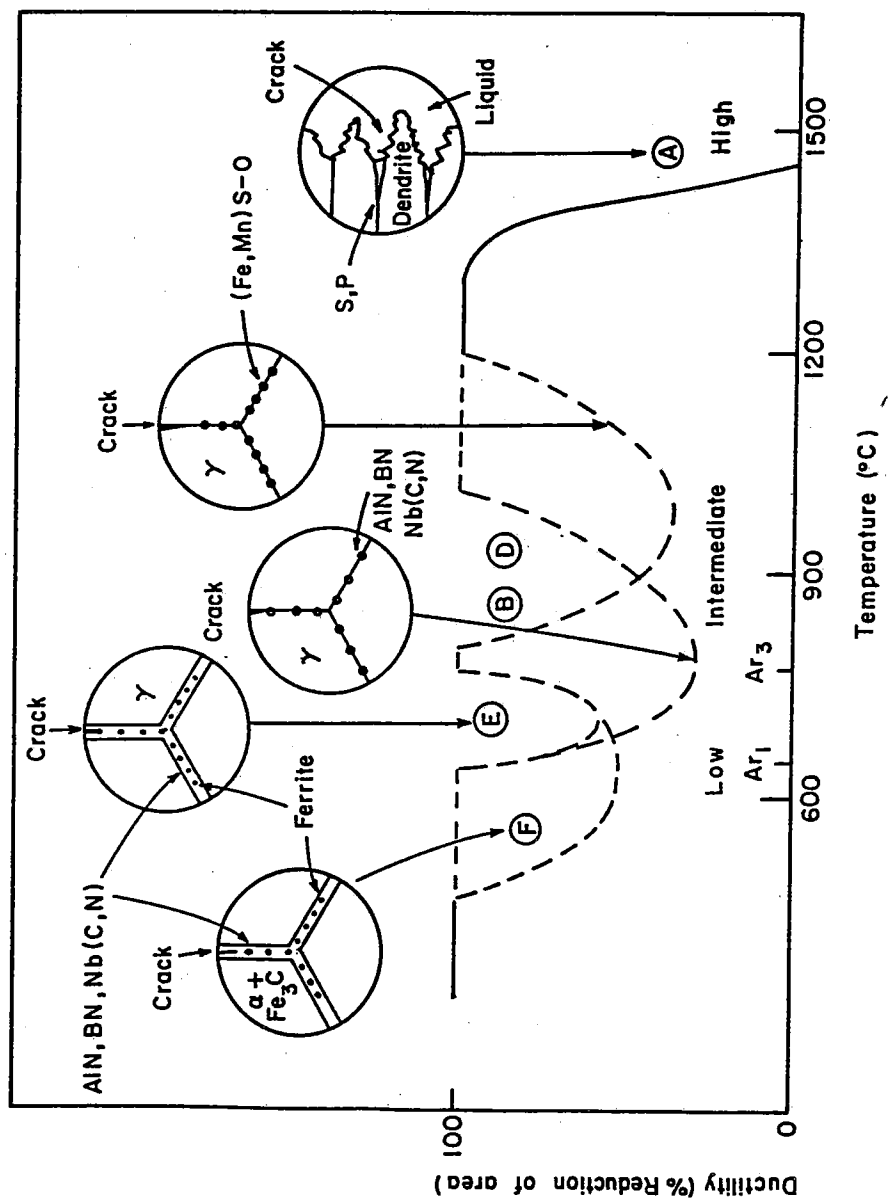


Figure 4. Schematic representation of temperature zones of reduced hot ductility of steel related to embrittling mechanisms.

severely weakened grain boundaries. Cracks at the solidification front can occur, particularly high in the caster where the newly formed shell is weak and easily bent, or lower in the caster as the strand passes through the unbending rollers.

At temperatures between roughly 900 and 1200 °C, (Zone B) sulfur segregates to the austenite grain boundaries, where it combines with iron and manganese to form sulfide and oxide precipitates. These precipitates, particularly FeS, weaken the grain boundaries and can lead to intergranular cracks. Embrittlement is most severe when large numbers of very fine precipitates pin the grain boundaries and enhance strain concentration there. Thus, the phenomenon is most severe at higher sulfur contents and higher strain rates (above 10^{-3} /sec). At lower strain rates, the precipitates coarsen and are less able to pin the grain boundaries. Both of these first two embrittlement zones can be reduced by reducing the sulfur content or increasing the manganese content, since the latter forms less harmful MnS precipitates. Decreasing the sulfur content is the best solution, and this is being achieved as more mills become cleaner. It is obviously not possible for resulfurized, free-machining steels, where the control of stress and strain becomes crucial.

At lower temperatures, a large ductility trough exists in the 700-900°C range, (Zone D). The embrittling mechanism is similar to that in Zone B, but nitride precipitates (particularly AlN) are formed at the austenite boundaries in place of sulfides. Since the AlN precipitates take longer to nucleate and grow, embrittlement is worst at lower strain rates, and is most severe in microalloyed steels containing other nitride formers: niobium, vanadium, and boron. Removal of aluminum alleviates the problem but AlN precipitates are beneficial, since they refine the austenite grain size, and retard recrystallization, resulting in improved low temperature toughness. Addition of titanium can aid hot ductility by forming

coarse TiN precipitates and preventing AlN formation, but at the expense of reduced low temperature toughness.

The practice of soft "air-mist" cooling attempts to allow time for the AlN precipitates to coarsen, but the kinetics of coarsening are not rapid enough to cause significant improvement in ductility [26].

At still lower temperatures, (Zone E), the presence of ferrite (α) at the grain boundaries adds to the precipitation mechanism. The resulting strain concentration at the prior pro-eutectoid ferrite grain boundaries can lead to crack formation.

Various defects have been found in hot charged steel products. Longitudinal facial cracks are generally triggered by high heat transfer in the mold. This uneven cooling in the mold may be caused by nonuniform mold flux viscosity resulting in uneven powder distribution in the gap between the shell and the mold wall. However, if the mold powder is too viscous, it cannot fill the gap evenly, also resulting in cracking. After formation, these cracks may be enlarged by nonuniform cooling of the surface as it passes through the secondary cooling zone. Careful control of mold powder viscosity and contamination by oxidation products are possible solutions to the longitudinal cracking problem [26].

Star cracks are another problem arising in the mold. They are due to embrittlement caused by copper pick-up by the slab surface in the mold region and are eliminated by chrome plating of the copper mold. Copper has also been found to exacerbate the important defect of transverse cracks [26].

Transverse surface cracks are thought to form while the surface is in the temperature range of the 700-900 °C ductility trough mentioned above. They are usually found at the base of the oscillation marks, which act like a notch, or stress riser, when strained [27]. In addition, lower heat transfer in the mold due to the added gap of the mark results in a coarser austenitic structure, increasing the susceptibility of the slab to surface cracking due to strain concentration at the grain boundaries. Thus, decreasing the depth of the oscillation marks through careful control of the mold oscillator has been shown to decrease the incidence of transverse cracks. For example, a high speed, short stroke oscillation practice reduces the oscillation mark depth and pitch.

The 700-900 °C ductility trough corresponds to the temperature range when the strand is in the lower part of the casting machine. Any tensile strain, such as that from unbending, could combine with the notch effect and the loss of ductility and form a crack. Thus, transverse cracking has also shown a strong correlation to roll gap, roll alignment, and roll surface condition in the straightening section [26]. To avoid cracking problems due straightening strains, it is recommended that the unbending occur with the slab above the ductility trough temperature range [28]. This is also consistent with the goals of hot charging. However, it may leave the strand more susceptible to internal cracking from hot tearing, since the thinner shell has less strength to withstand strains from slight roll misalignment and bulging due to ferrostatic pressure.

This temperature range of 700 - 900 °C also corresponds to the approximate temperature of the slab during the transfer and early reheating stages. It is therefore possible that thermal stresses associated with reversals in temperature gradients and phase transformation volume changes may present additional cracking problems for hot charged slabs. The problem of panel crack

formation in static cast steel ingots has been found to be due to this mechanism and is controlled by the "track" times elapsed prior to rolling. [32] Few problems are experienced in slabs that are cooled to ambient temperature prior to reheating. The worst thermal sequence is to reheat the ingot from an intermediate stage of air cooling when an austenitic interior is surrounded by a surface that is transforming to ferrite and pearlite and expanding. This can give rise to a sub-surface zone of tensile stress during reheating that produces cracks in the nitride-embrittled austenite just beneath the surface. These cracks can then propagate to the surface later during reheating or air cooling prior to hot rolling.

It is suspected that a similar mechanism might produce cracks in continuously-cast slabs that are hot-charged. Indeed, track time, or the transfer time between the caster and the furnace, has been linked to surface defect formation in blooms [29]. As track times increased, the defect incidence decreased. Also noted was the "safe" extension of track times if the blooms were transported under insulated hoods. Clearly, the defect formation was related to the slab temperature, and it should be noted that the reported defects dropped off substantially as the hot charge temperature dropped below the ductility trough temperature range. To combat this, in-line quenching after torch cut-off has been implemented at some plants, but while it has been reported to decrease the defect rates, it also defeats the purpose of hot charging. These experiences prompted the present research.

1.4 HOT CHARGING

Hot charging is being implemented currently at several steel mills. To facilitate hot charging, several prerequisites must be met [3]. First, the continuous caster must produce high temperature slabs, so that the maximum amount of heat may be retained and the slabs do not have to be reheated as much prior to rolling. This involves softer cooling practices in the secondary cooling zones, and higher constant casting speeds utilizing the full caster length. Also, radiation shielding on the narrow face lowers the cooling of this face. After casting, the slabs must be kept insulated during transfer to avoid heat losses due to radiation.

The next prerequisite is the production of defect-free slabs, since the hot charging process does not allow time for conditioning, and inspection is very difficult at the high temperatures involved. One solution to this problem is currently being used at Stelco [26]. A slab quench tank was installed close to the caster run-out table. A representative slab is selected and quenched. The slab is then removed and carefully inspected. Based on the number of defects found, the slabs may be approved or rejected for hot rolling. This process takes approximately one hour to perform, and can also indicate what is causing the defects. If the problem is mechanical in nature, such as incorrect roll gap, then adjustments may be made and the quench tank can rapidly assess their success while the caster is still on-line.

As discussed earlier, mist cooling allows softer, but more uniform cooling which avoids cracking problems due to large temperature changes on the surface. However, higher slab temperatures reduce the rigidity of the solidifying shell, and make it more susceptible to internal cracks due to bulging. More

precise roll alignment and smaller, closer rolls are one solution to this problem. However, roll bending must also be considered with smaller rolls. Compression casting, introduced earlier, has also been suggested as a way to reduce the overall strains in the slab [2]. Compression casting aims to keep the entire strand in slight compression, especially at the unbending points. When the strand is being bent, the tensile strains due to unbending and the compressive strains superimpose on each other, dropping the tensile load below a critical level to prevent cracking. Compression casting should not be confused with the process of "soft reduction" or "squeeze casting" where the strand is actually compressed by the guide rollers near the end point of solidification. Finally, quenching of the strand prior to unbending has been suggested as an alternative way to avoid the internal cracking problems associated with unbending while the strand is in the critical temperature zone of embrittlement. This has not received wide practice, though, since it wastes thermal energy and actually increases thermal stresses.

To the authors' knowledge, no investigation has tried to predict the strain and stress distribution, as well as heat transfer in a continuous casting - hot charging process. Recent work involving static-cast ingots has demonstrated the applicability of mathematical models to the prediction of heat flow and stress generation in a solidifying steel ingot during thermal processing [30,31]. Knowledge of the thermally induced stress and strain aids understanding of defects and their relation to process parameters. It is with this goal that the current research has been conducted.

2. MODEL DEVELOPMENT

The finite element method was used to model the heat flow and stress distribution in the continuously cast strand. An existing program [32] was modified to simulate the different stages of the slab casting process. This code was originally used to model the thermal processing of a static cast ingot [30,31]. The modified program is called CONCAST and has several features which allow it to simulate the continuous casting process. Although the fortran code is still under development, features used in the present work will be discussed in detail below. Details concerning the finite element method and the resulting equations can be found in any finite element text [35-38] and will be discussed only briefly.

2.1 HEAT TRANSFER FORMULATION

A two dimensional, transverse slice through the strand is simulated in the present work, with the third dimension (casting direction) being simulated by moving the slice through time in this dimension. This necessitates the assumption that no heat flows in the third direction which has been shown to be reasonable [33]. The heat transfer model is based on the two-dimensional, transient heat conduction equation:

$$\frac{\partial}{\partial x} \left(k_x \frac{\partial T}{\partial x} \right) + \frac{\partial}{\partial y} \left(k_y \frac{\partial T}{\partial y} \right) = \rho C_p \frac{\partial T}{\partial t} \quad (1)$$

where: k_x, k_y = Thermal conductivity of material in x and y directions

T = Temperature

t = time

ρ = mass density

C_p = specific heat at constant pressure

The finite element method discretizes the domain into small, finite elements. In each element, a function approximates the differential equation. The solution is compatible at the element boundaries. In this model, constant gradient triangles are used and their approximating function is linear in temperature:

$$T = Ax + By + C \quad (2)$$

Although higher order elements allow more flexibility in approximating functions, they are also harder to work with and are more computationally expensive.

Because the approximating function is not exact, an error, or residual will exist at each nodal point in the region. Galerkin's method is a numerical technique which forces these residuals to zero. Applying this method to Eq. (1) yields the following matrix equations:

$$[K]\{T\} + [C]\{\dot{T}\} = \{Q\} \quad (3)$$

where: $[K]$ = conductance matrix

$[C]$ = capacitance matrix

$\{Q\}$ = external heat flux vector

$\{T\}$ = nodal temperatures

$\{\dot{T}\}$ = time derivatives of the temperature field

Because a time derivative appears in Eq. (3), some sort of time-stepping technique must be used to approximate this derivative. For example, $\{\dot{T}\}$ could be approximated by:

$$\{\dot{T}\} = \frac{\partial T}{\partial t} = \frac{\Delta T}{\Delta t} = \frac{T_{\text{new}} - T_{\text{old}}}{\Delta t} \quad (4)$$

This relationship could then be used in Eq. (3). T_{new} could be explicitly solved for and would become T_{old} for the next time step. This method is common and rather effective, but three level time-stepping techniques provide better accuracy and stability. Two such methods are implemented in CONCAST: Lees and DuPonts.

In the Lees formulation, the time derivative of the temperature vector are:

$$\{\dot{T}\} = \left\{ \frac{T_3 - T_1}{2\Delta t} \right\} \quad (5)$$

$$\{T\} = \frac{1}{3} \{T_1 + T_2 + T_3\} \quad (6)$$

where T_3 is the temperature for which the current equations are being solved, T_2 is the temperature at the last time step, and T_1 is the temperature at the time step before T_2 .

In the DuPont formulation, the corresponding equations to Eqs. (5) and (6) above are:

$$\{\dot{T}\} = \left\{ \frac{T_3 - T_1}{2\Delta t} \right\} \quad (7)$$

$$\{T\} = \frac{1}{4} \{3T_3 + T_1\} \quad (8)$$

with T_1 , T_2 , T_3 as defined above. Both of these techniques are discussed in more detail elsewhere [34]. A complete flowchart of the heat flow model is shown in Figure 5.

CONCAST allows three formulations of the capacitance matrix $[C]$ in Eq. (3). The consistent capacitance formulation, lumped formulation, and "Ohnaka lumped" formulation may be requested. "Ohnaka" differs from the normal lumping in that the lumping is based on the amount of area that is closest to each node. Thus, an equilateral triangle would have the same "Ohnaka" and standard lumped capacitance matrix.

In this model, the latent heat of solidification is handled by calculating an effective specific heat through the use of the enthalpy function, H . The two methods available for calculating C_p are the Lemmon method and Del-Giudice method. Both methods involve differentiation of the enthalpy function and temperature field across the element, and are described in detail elsewhere [34].

Substituting the capacitance matrix $[C]$ and the Lees time derivative vector $\{\dot{T}\}$ into Eq. 3 and reducing yields:

$$[K] \left\{ \frac{T_1 + T_2 + T_3}{3} \right\} + [C] \left\{ \frac{T_3 - T_1}{2\Delta t} \right\} = \{Q\} \quad (9)$$

The corresponding equation using the DuPont formulation is:

$$[K] \left\{ \frac{3T_3 + T_1}{4} \right\} + [C] \left\{ \frac{T_3 - T_1}{2\Delta t} \right\} = \{Q\} \quad (10)$$

The Choleski method is used in CONCAST to solve this system of simultaneous equations.

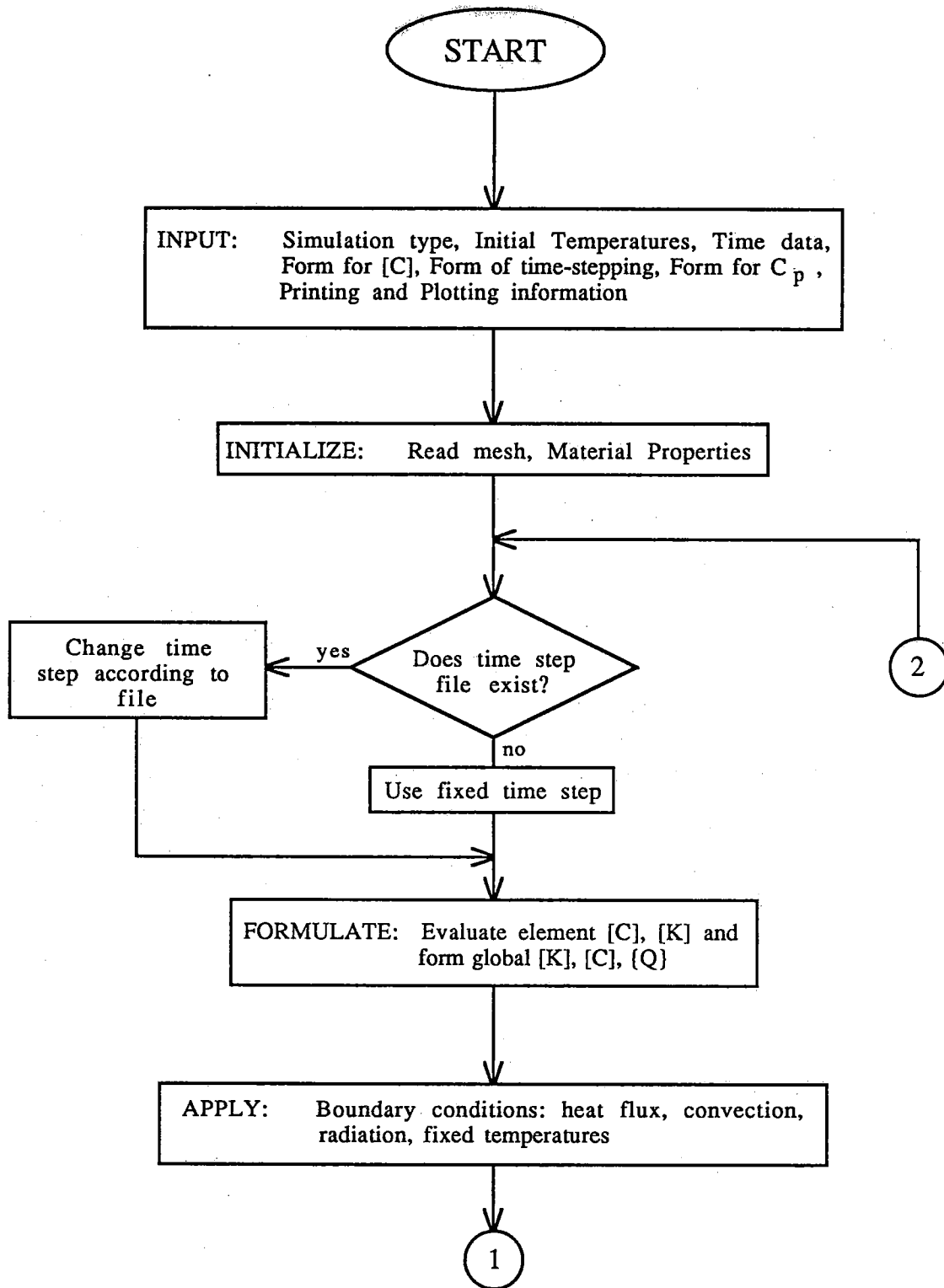


Figure 5. Flowchart of the heat flow model.

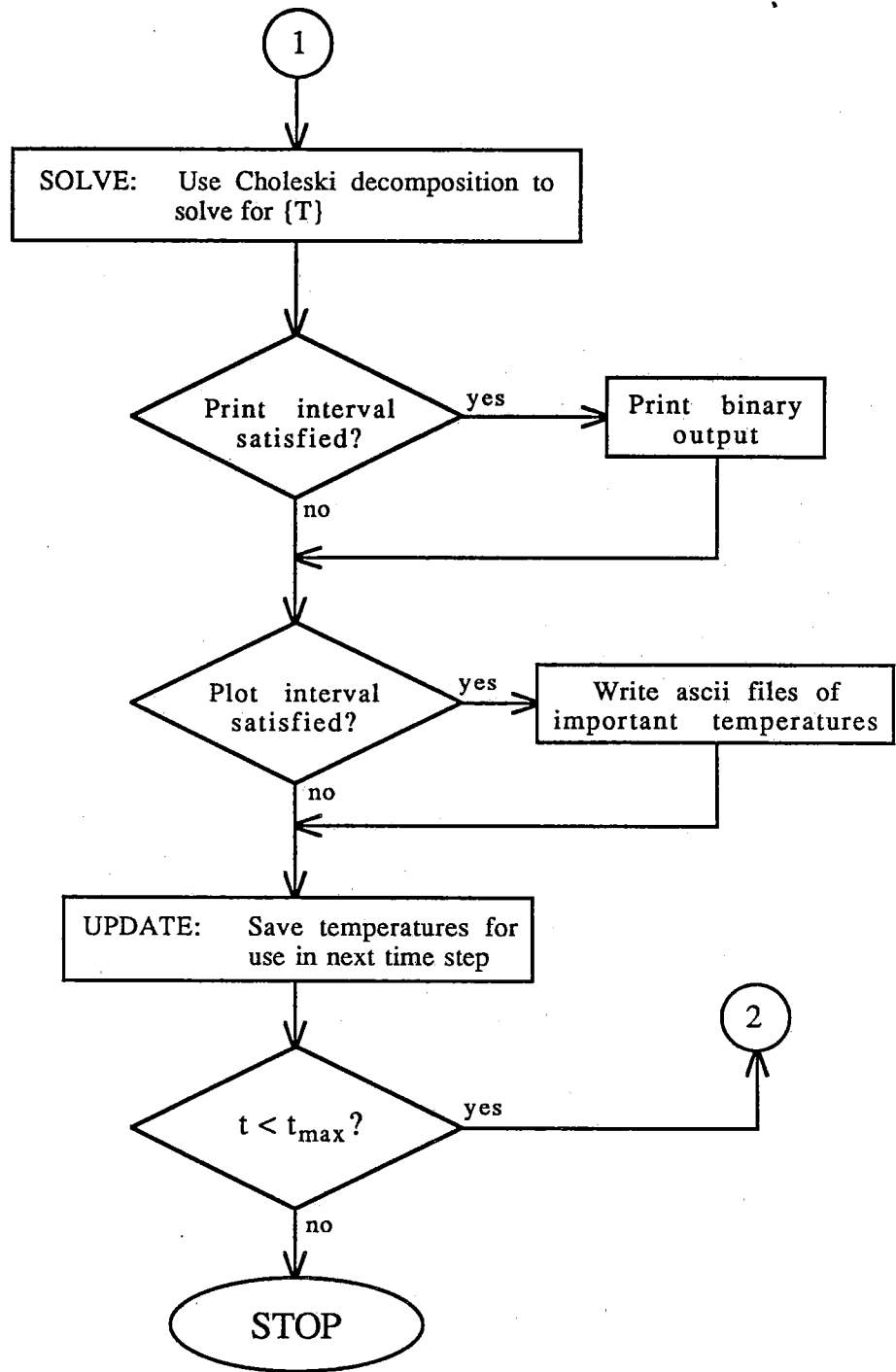


Figure 5. Flowchart for the heat flow model (continued).

This model has many features which allow flexibility in modeling thermal problems. For material properties, such as enthalpy, density, and conductivity, any user-defined equation or value may be used. Several types of boundary conditions may be applied. Along an element face, heat transfer by convection, by a heat flux, or by radiation may be simulated. Also, heat generation within an element and specified nodal temperatures may be imposed. Lastly, a gap boundary condition may be simulated, as might occur in the mold region. Combinations of these six boundary conditions are usually sufficient to model all thermal situations.

Finally, the model allows the user to control the time step size at any time in the simulation. Based on a coded number read from a time step size file, the model may cut the step size in half, double the size, halt execution, or continue at the previous step size. In this way, the step size may be tailored to each particular run, saving unnecessary calculations.

2.2 STRESS FORMULATION

The stress distribution within the two-dimensional region is governed by the differential equation of equilibrium for plane elasticity:

$$\frac{\partial \sigma_x}{\partial x} + \frac{\partial \tau_{xy}}{\partial y} = -F_x \quad (11)$$

$$\frac{\partial \tau_{xy}}{\partial x} + \frac{\partial \sigma_y}{\partial y} = -F_y \quad (12)$$

The strain-displacement relations can be stated in matrix form [36]:

$$\begin{Bmatrix} \epsilon_x \\ \epsilon_y \\ \epsilon_z \\ \gamma_{xy} \\ \gamma_{yz} \\ \gamma_{zx} \end{Bmatrix} = \begin{bmatrix} \frac{\partial}{\partial x} & 0 & 0 \\ 0 & \frac{\partial}{\partial y} & 0 \\ 0 & 0 & \frac{\partial}{\partial z} \\ \frac{\partial}{\partial y} & \frac{\partial}{\partial x} & 0 \\ 0 & \frac{\partial}{\partial z} & \frac{\partial}{\partial y} \\ \frac{\partial}{\partial z} & 0 & \frac{\partial}{\partial x} \end{bmatrix} \begin{Bmatrix} u \\ v \\ w \end{Bmatrix} \quad (13)$$

The incremental, elastic form of Hooke's law is

$$\{\Delta\sigma\} = [E]\{\Delta\epsilon_e\} \quad (14)$$

where $[E]$ is a matrix of the material stiffnesses, $\{\Delta\sigma\}$ is the stress vector, and $\{\Delta\epsilon_e\}$ is the elastic strain vector.

To reduce Eqs. (13) and (14) to a two-dimensional case, the third dimension, z , must be related to the other two coordinate directions. The four ways of handling this are plane stress, plane strain, generalized plane strain, and axisymmetric conditions. Plane stress assumes that the stress in the z -direction is zero, whereas plane strain assumes the strain is zero in the z -direction. Generalized plane strain is similar to plane stress, however the strain in the z -direction is a constant value determined by averaging the z -strains over the region. Thus, neither the stress nor the strain is zero in the z -direction. The last condition, axisymmetric, is used for cylindrical-type regions where a condition of axial symmetry exists. All derivatives in the

angular direction (around the axis of symmetry) are assumed zero. All four cases are implemented in CONCAST, however axisymmetric has not been fully verified. Also, generalized plane strain has been found too computationally intensive to be used in large simulations, since iteration presently must be performed to determine the z-strain value. Full derivations of these strain states and the resulting equations for $[E]$, $\{\Delta \sigma\}$, and $\{\Delta \epsilon\}$ can be found elsewhere [39].

The total incremental strain vector in Eq. 14 was divided into three parts:

$$\{\Delta \epsilon\} = \{\Delta \epsilon_e\} + \{\Delta \epsilon_T\} + \{\Delta \epsilon_p\} \quad (15)$$

where $\{\Delta \epsilon_e\}$ is the elastic strain increment, $\{\Delta \epsilon_T\}$ is the thermal strain increment, and $\{\Delta \epsilon_p\}$ is the plastic creep strain increment.

The incremental thermal strain $\Delta \epsilon_T$ is formulated as:

$$\Delta \epsilon_T = TLE(T_{t+\Delta t}) - TLE(T_t) \quad (16)$$

where thermal linear expansion (TLE) is described by the state function:

$$TLE(T) = \int_{T_0}^T \alpha_T(T) dT \quad (17)$$

where α_T is the thermal linear expansion coefficient, and T is an arbitrary base temperature, assumed to be 0°C . In this way the temperature dependence of α_T may be modeled. Also, the model takes into account the volume change due to the phase transformation of steel. This is accomplished by taking a

weighted average of TLE based on the fraction of ferrite (α) and austenite (γ) present:

$$TLE = (\% \alpha) TLE_{\alpha} + (\% \gamma) TLE_{\gamma} \quad (18)$$

In this model, the incremental plastic strain is characterized by:

$$\Delta \epsilon_p = \Delta t \dot{\epsilon}_p(\sigma_{eff}, T, \epsilon_p) \quad (19)$$

where $\dot{\epsilon}_p$ is a scalar function dependent on the current effective stress, σ_{eff} , the current temperature, T , and the accumulated plastic strain, ϵ_p . This unified constitutive equation takes into account the various strain rate and temperature effects, and the combination of elastic-plastic strain and creep strain. A complete flowchart is shown in Figure 6.

The thermal and plastic creep strain vectors described above introduce nonlinearities into the problem. If these nonlinearities become too large, the explicit time-integration procedure is prone to instability. Thus, this model has several convergence schemes with parameters which enable the user to control these stability problems that are occasionally encountered.

Two routines in CONCAST can cause the model to reduce the time step and sub-iterate. The first checks the entire domain for the smallest ratio of incremental plastic strain to total effective elastic strain. If this ratio exceeds a user-defined value, the model cut the time step in half and solves this new time step. The second routine checks if the percent difference between the current plastic strain rate and the previous plastic strain rate is too large, and if so, cuts the time step in half and continues.

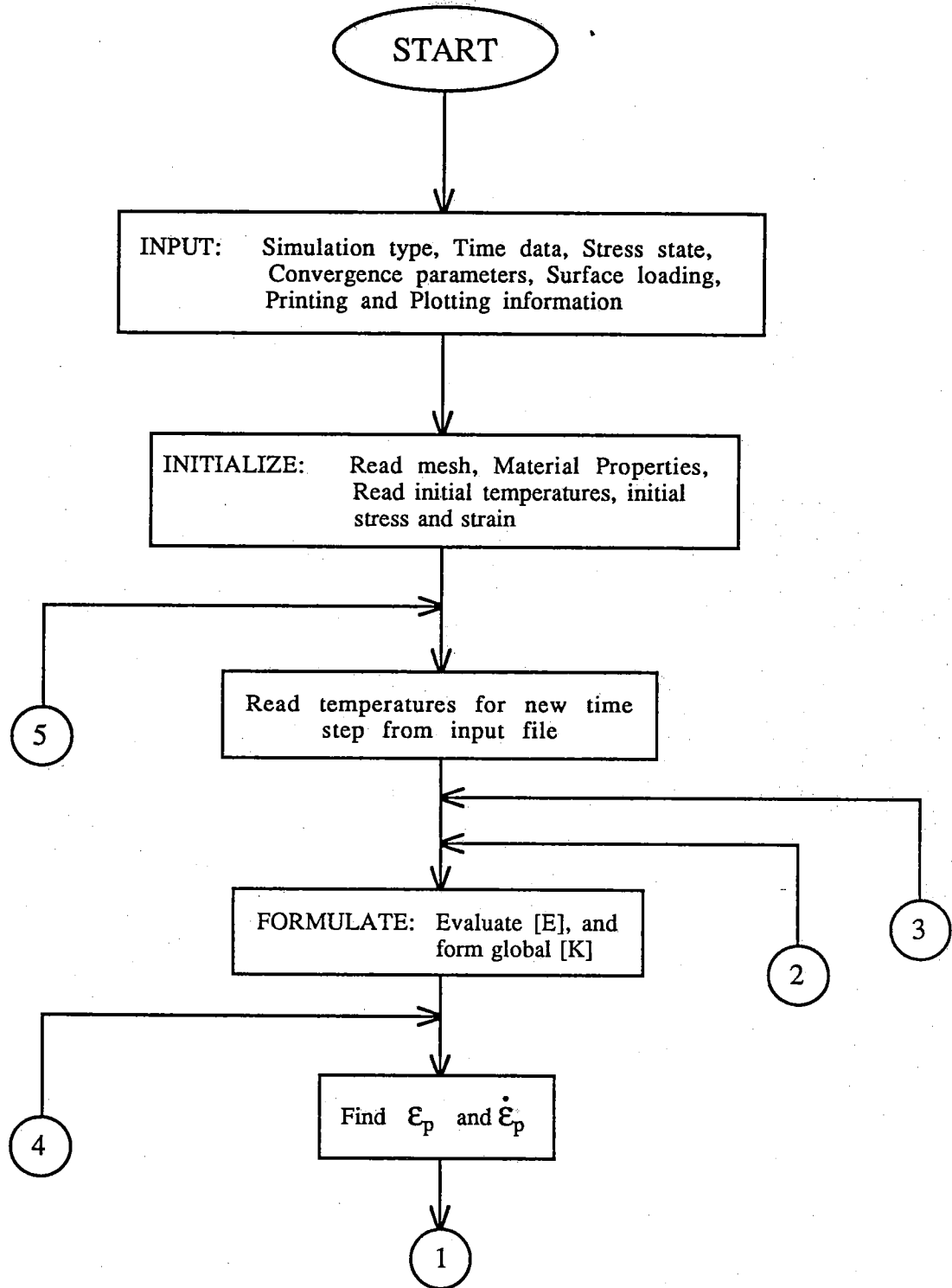


Figure 6. Flowchart of the stress model.

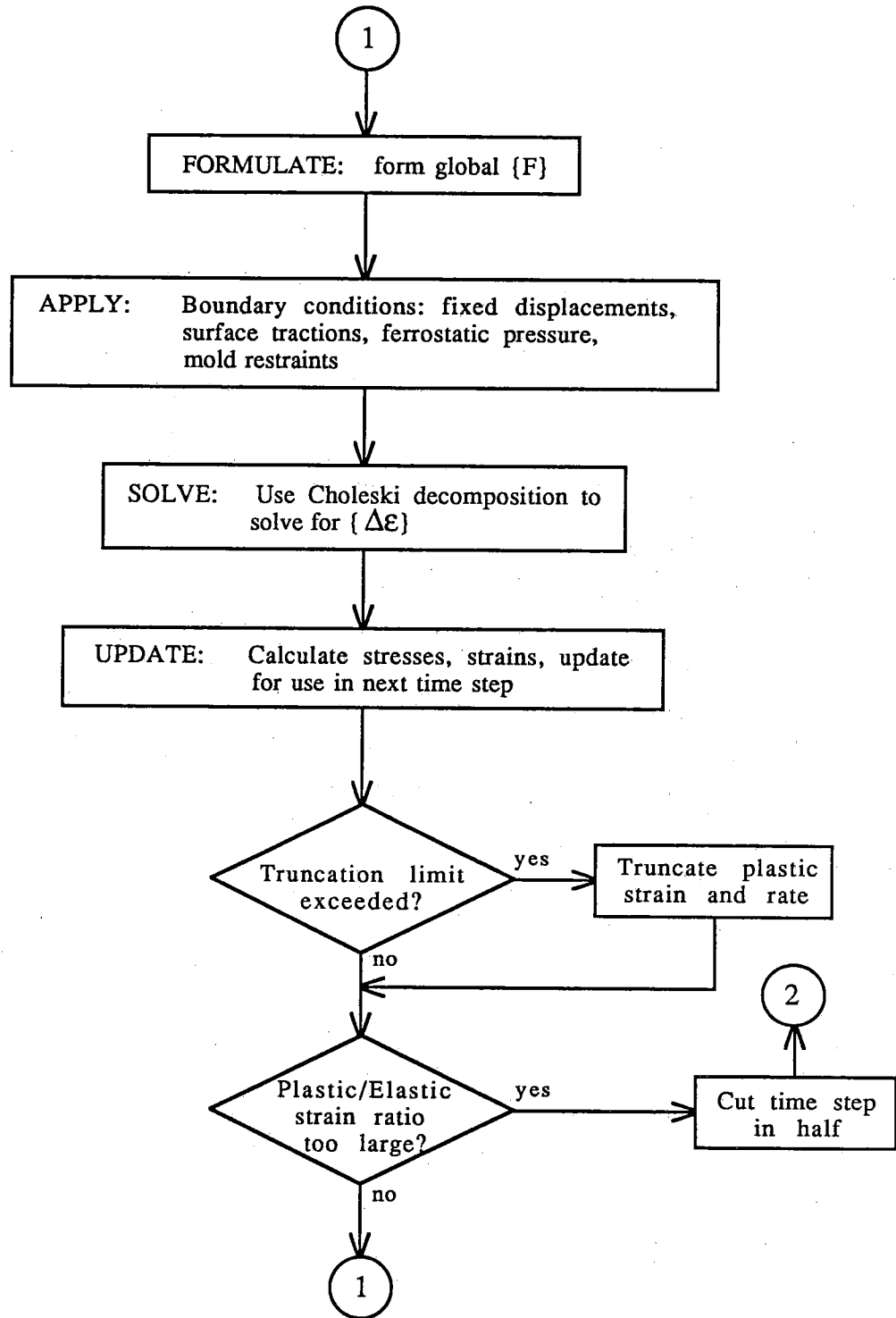


Figure 6. Flowchart for the stress model (continued).

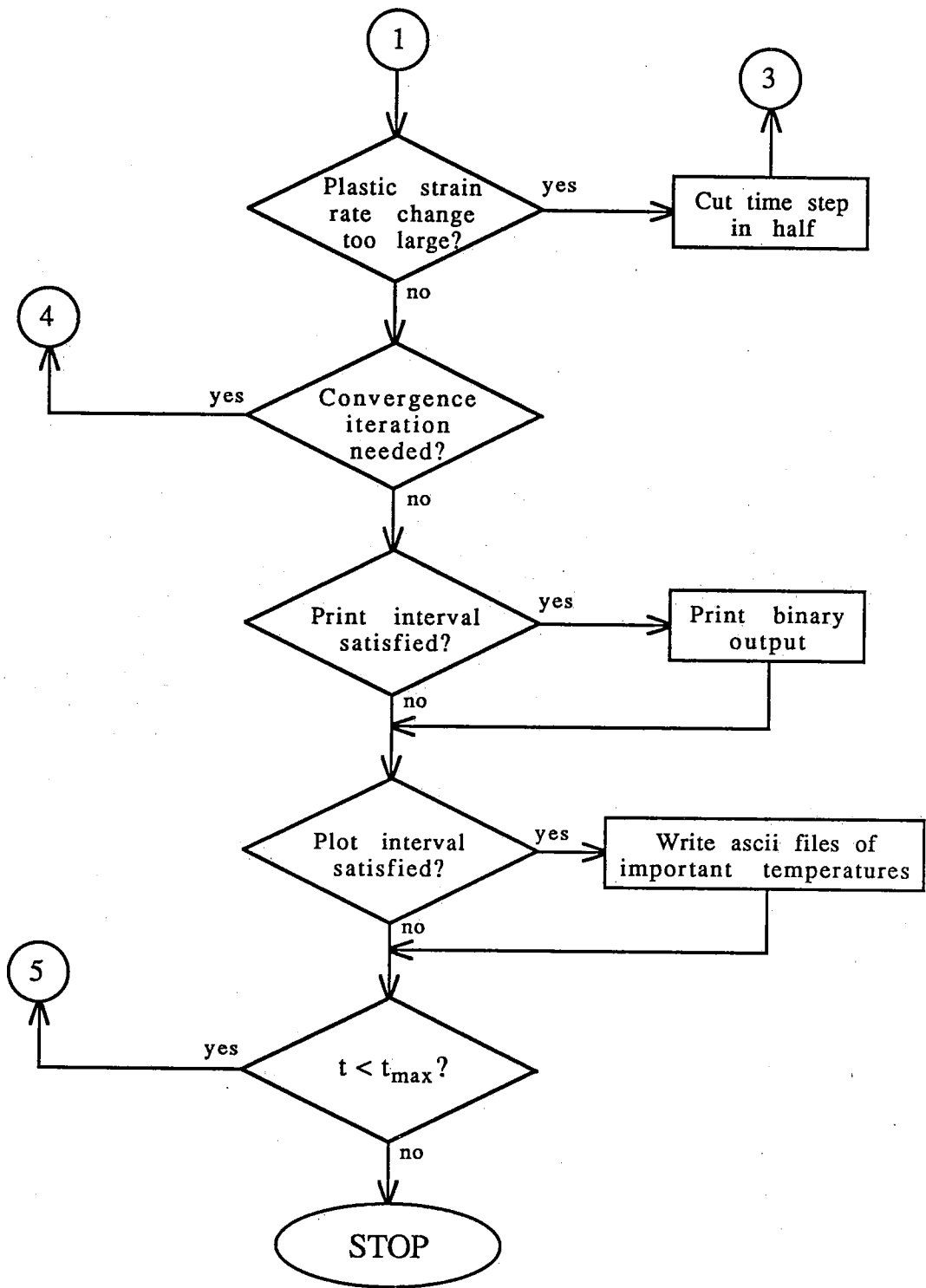


Figure 6. Flowchart for the stress model (continued).

The program also will resolve a time step to allow for convergence. This is based on the same percent difference as the last check described above. If the percent difference in plastic strain rate is greater than a user-defined value, but is not large enough to cause a sub-iteration, then a convergence iteration is performed. The time step is resolved using properties evaluated at the new stress/strain state.

Finally, a truncation routine in the program limits the maximum size of the plastic creep strain increment to a user-defined value. If the actual plastic strain rate is greater than the prescribed value, the plastic strain rate and incremental plastic creep strain is truncated to the limit values, and the simulation continues. If many truncations occur, accuracy of the solution may be questionable. Obviously, this method is highly dependent on time step size, and the output must be checked for extensive truncation, which indicates that the model has underpredicted strain and overpredicted stress. However, this method has the distinct advantage of being able to easily handle a situation where only a few nodes in the domain are highly strained. Without truncation, the model would sub-iterate extensively, trying to relieve the excess strain. The truncation routine limits strain at these nodes extensively, but would allow the simulation to continue on to the next time step. This eliminates problems caused by coarse meshes, for example, or when a region of little interest to the stress solution, perhaps the liquid steel, is trying to strain, thereby holding up the simulation needlessly.

2.3 OVERALL SIMULATION PROCEDURE

The heat transfer and stress models may be executed separately, or a coupled heat flow/stress run is possible. In the mold region, coupling allows

the heat flow model to determine the heat flux across the mold/shell interface based on the air gap thickness calculated by the stress model. Coupling also allows recalculation of the temperature distribution if the stress model sub-iterates, as described before. Usually, a thermal run is executed first, and after having verified that the resulting temperatures are reasonable, a stress run could be performed. In practice, however, a coupled heat flow/stress run is usually executed after the initial heat transfer run. The thermal calculations were found to be only a small part of the computing time with a coupled run, and in some cases, the coupled run was quicker than a stress run alone. For example, a simulation of the mold run involving plasticity used 7.7 CPU seconds for the thermal portion and 6814 CPU seconds for the corresponding stress part. However, the coupled heat/stress run using the same parameters took only 4378 CPU seconds. The time-savings resulted from fewer convergence iterations being performed since the thermal solution was recalculated for the stress model when it sub-iterated.

CONCAST is completely interactive and user-friendly. In addition, it provides the option of using an input file to eliminate repetitive typing of answers to the questions. An echo file is created each time the code is run, so this file may be edited and resubmitted. The program is divided into four simulation regions of the caster: mold, spray chamber, transfer, and reheat furnace. By selecting a certain simulation type, the user is branched to that section and answers questions pertaining to that particular part of the casting process.

The mold region has many options, due in part to the complex nature of the heat transfer in the mold. Ferrostatic pressure may be applied to the solidifying shell due to the head of steel inside. A corresponding mold

stiffness must then be supplied to simulate the mold pushing back the shell. The mold taper may also be included so that the appropriate gaps or interferences may be determined. This allows realistic modeling of the sharp heat transfer drop as the gap between the shell and mold appears, and the strain caused by the mold pushing back on the shell when they meet. Also included are the important effects of the mold powder.

The spray region is divided into five zones. Several parameters must be provided to describe each zone. The distance to the start of each zone and the number of rolls in each zone are used to calculate the roll centerlines. The model assumes that the rolls are evenly spaced in each zone. The roller diameters, the spray water temperature, and the spray water flux are used to calculate the appropriate boundary conditions for the strand as it passes through the rollers. Determination of these boundary conditions will be discussed later.

The transfer and reheat regions are quite similar. Both require the user to supply a radiation emissivity for the strand and a temperature of the surface with which the strand radiates. The length of transfer and of reheat are also needed.

2.4 POSTPROCESSING

CONCAST output is in binary form to save computing time and lower file size. To manipulate this output, a postprocessor was developed. This program is also interactive, and has the echo file feature described previously. A complete copy of the postprocessing program is included in Appendix B.

The postprocessor has three main types of output. First, the postprocessor can take a binary output file and create a startup file for a new run. Using this feature, CONCAST can be easily restarted at any point in a previous run. This is very advantageous if a run was somehow accidentally stopped during execution. Instead of having to start the run over from the beginning, the postprocessor can create a startup file using the latest data written to the binary output file, and restart the run.

The second type of output is contour plots of any variable, at any iteration, time, or position along the caster. These plots include contour labelling, and maximum and minimum markings. Contour values may be automatically defined, or may be specified by the user. Meshes may also be plotted to check their integrity before they are used in CONCAST. Some variables that may be plotted are temperature, displacement, elastic stresses and strains, plastic stresses and strains, principal stresses and strains, effective stress, and strain rates. In all, 37 different variables are available for plotting.

Finally, the postprocessor can create printouts of the variables described above. The data can be printed out at various time steps or can be printed in a time dependent form. In the latter case, the file can be transferred to other plotting packages and x-y type plots may be made. Shell thickness may also be tracked over time, and plotted in this manner. The postprocessor is a very versatile package which allows the user great flexibility in what can be analyzed, and how it can be presented.

Because this code was eventually run on various types of computers, the binary output files from the various machines were not compatible. To

overcome this problem, a binary-to-ascii file translator was developed, as was a corresponding ascii-to-binary translator. The binary file is translated to an ascii file on the first computer, and is transferred to the second machine. The file is then converted back into a binary file on the second machine for use with the postprocessor. A complete listing of these translators is included in Appendix C.

Finally a mesh generator was developed to facilitate creating meshes in the format which can be read by the CONCAST program. This will not be discussed in any detail here, but is included in Appendix D for completeness.

3. MODEL VERIFICATION

To verify the computer program, a problem involving both thermal strain and plastic creep was obtained for which the analytical solution is known. The solution was derived from Boley and Weiner [40], and a complete derivation of the governing equations appears in Appendix E.

A long, thin beam, 20mm x 0.8mm, was subjected to an instantaneous cubic temperature distribution:

$$T = 100 + 3000 y + (-0.3 \text{ e}7) y^2 + (-0.5 \text{ e}8) y^3 \quad (20)$$

with the $y=0$ at the midpoint of the beam. The initial temperature of the beam was 0°C . The beam was unconstrained in the y -direction, except for one node in the center of the left side to prevent rigid body motion. The beam is totally constrained in the x -direction. The applied constraints and the thermal load are shown in Figure 7. The material used had an elastic modulus of 200 GPa, a thermal linear expansion coefficient of $12\text{e-}6 \text{ }^\circ\text{C}^{-1}$, and a Poisson's ratio of 0.25, and the coefficient A was $1\text{e-}13 \text{ Pa}^{-1}\text{s}^{-1}$.

The solution for this problem is as follows: (see details in Appendix E)

$$\sigma_y = \sigma_z = \tau_{xy} = 0 \quad (21)$$

$$\sigma_x = \sigma_{x0} \exp[-EA(t - t_0)] \quad (22)$$

$$\epsilon_x^p = \frac{\sigma_{x0}}{E} (1 - \exp[-EA(t - t_0)]) \quad (23)$$

$$\epsilon_y^p = -\frac{1}{2} \epsilon_x^p = \frac{\sigma_{x0}}{2E} (\exp[-EA(t - t_0)] - 1) \quad (24)$$

Note that plastic strain is directly proportional to stress, which decreases asymptotically to zero.

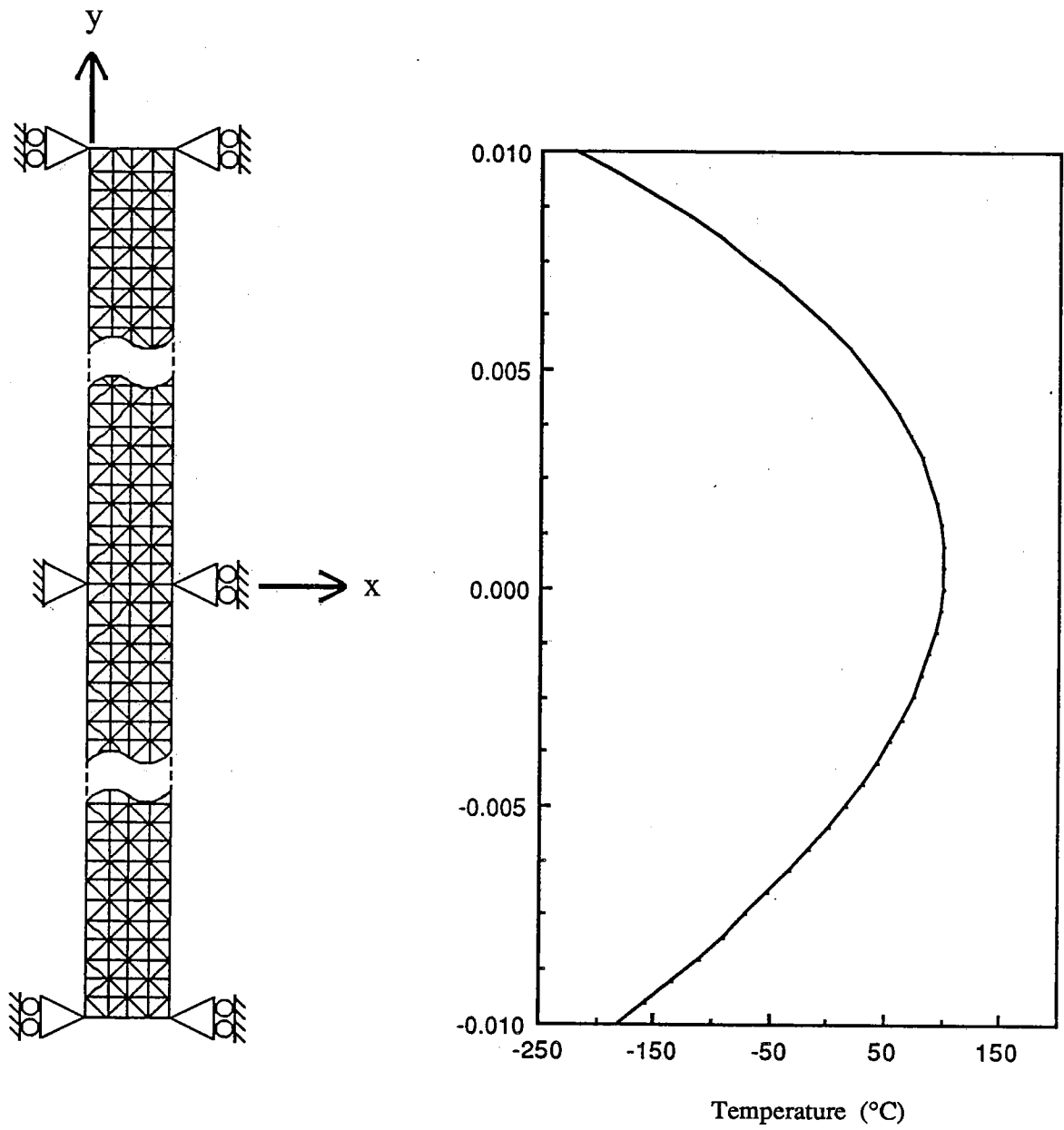


Figure 7. Displacement boundary conditions and thermal loads used in the verification problem.

The stress model was programmed to solve this transient, plastic creep problem. A 505 node by 800 mesh of triangular elements was created using a "British jack" arrangement similar to that used in the simulations. A constant time step of 1 second was used, with a maximum time of 20 seconds. The model predictions of both stress and plastic strain were compared at the bottom ($y = -0.01$), center ($y = 0.0$), and top ($y = 0.01$) of the long beam. The calculated and predicted x-stress is plotted in Figure 8. Excellent agreement was found between the analytical and model solutions, with a maximum difference in x-stress of just over 12% in the center of the beam. X-plastic strain is compared in Figure 9, and y-plastic strain is compared in Figure 10. Maximum difference between the model predictions and the analytical solution was just under 2% at the top node for the x-plastic strain. The maximum difference for the y-plastic strain was also just under 2% at the top node. Tabulated values for Figures 8, 9, and 10 are included in Appendix E.

Clearly, the model accurately predicts displacements, strains and stresses including plastic creep. Further verification of the program was not pursued since the original code had been adequately verified. This problem verifies the integrity of the code after modifications to allow modeling the continuous casting process.

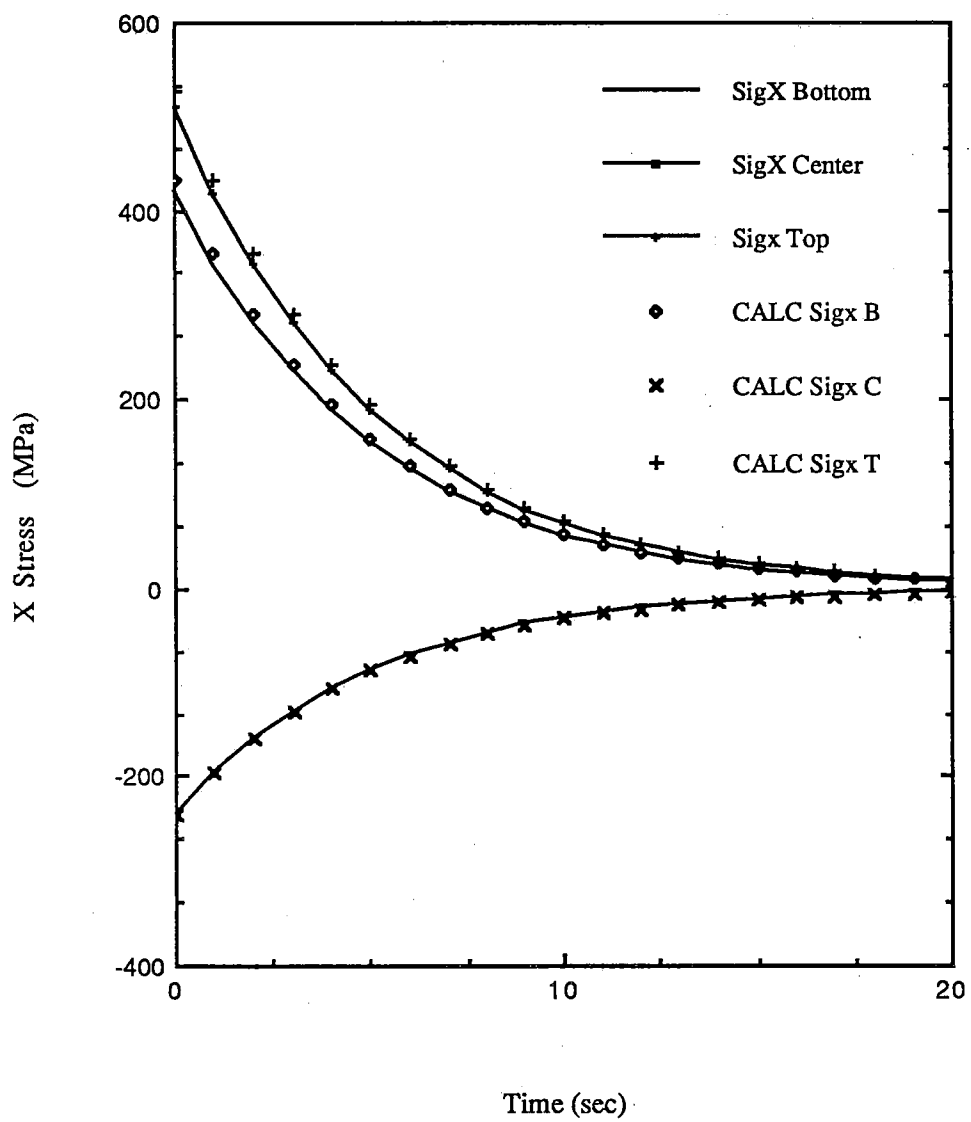


Figure 8. Comparison of x-stress from analytical solution and finite element model.

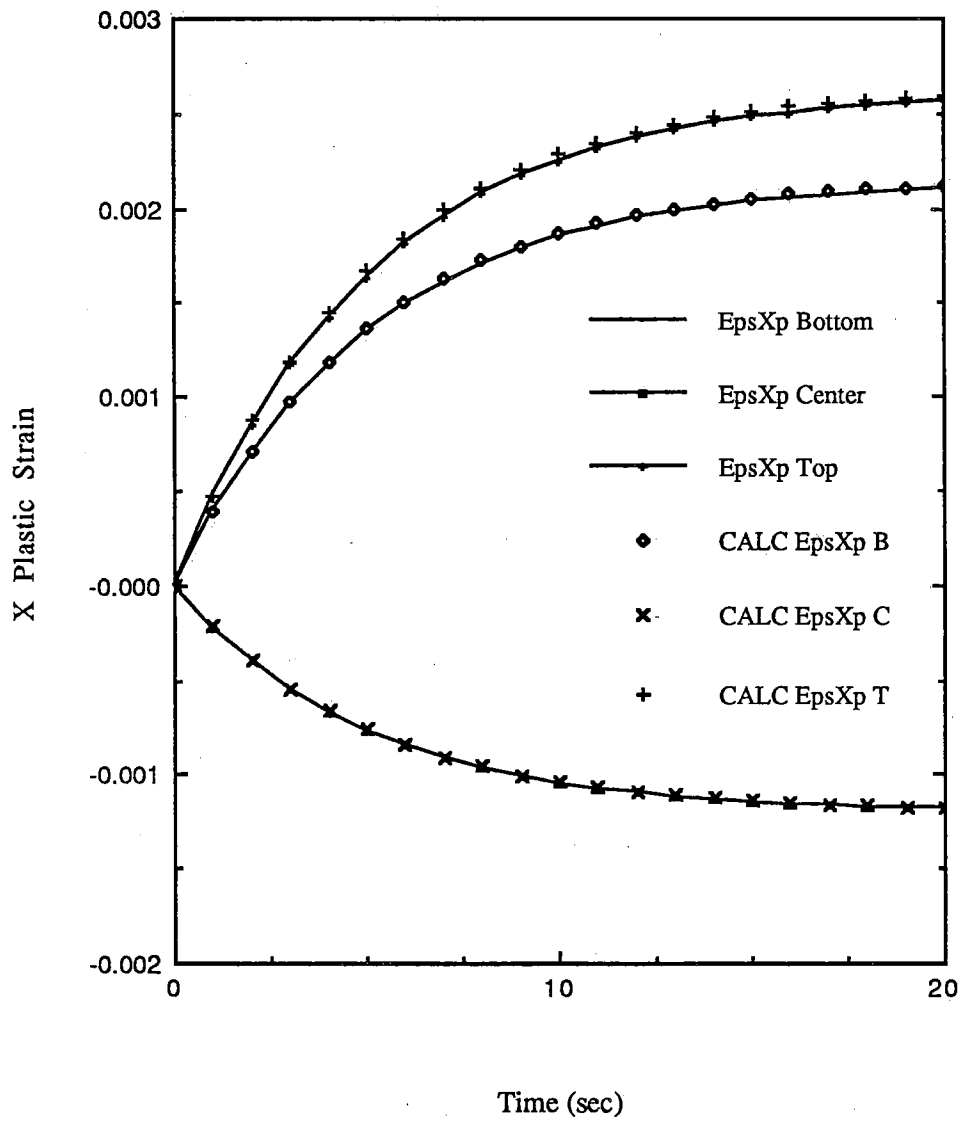


Figure 9. Comparison of x-plastic strain from analytical solution and finite element model.

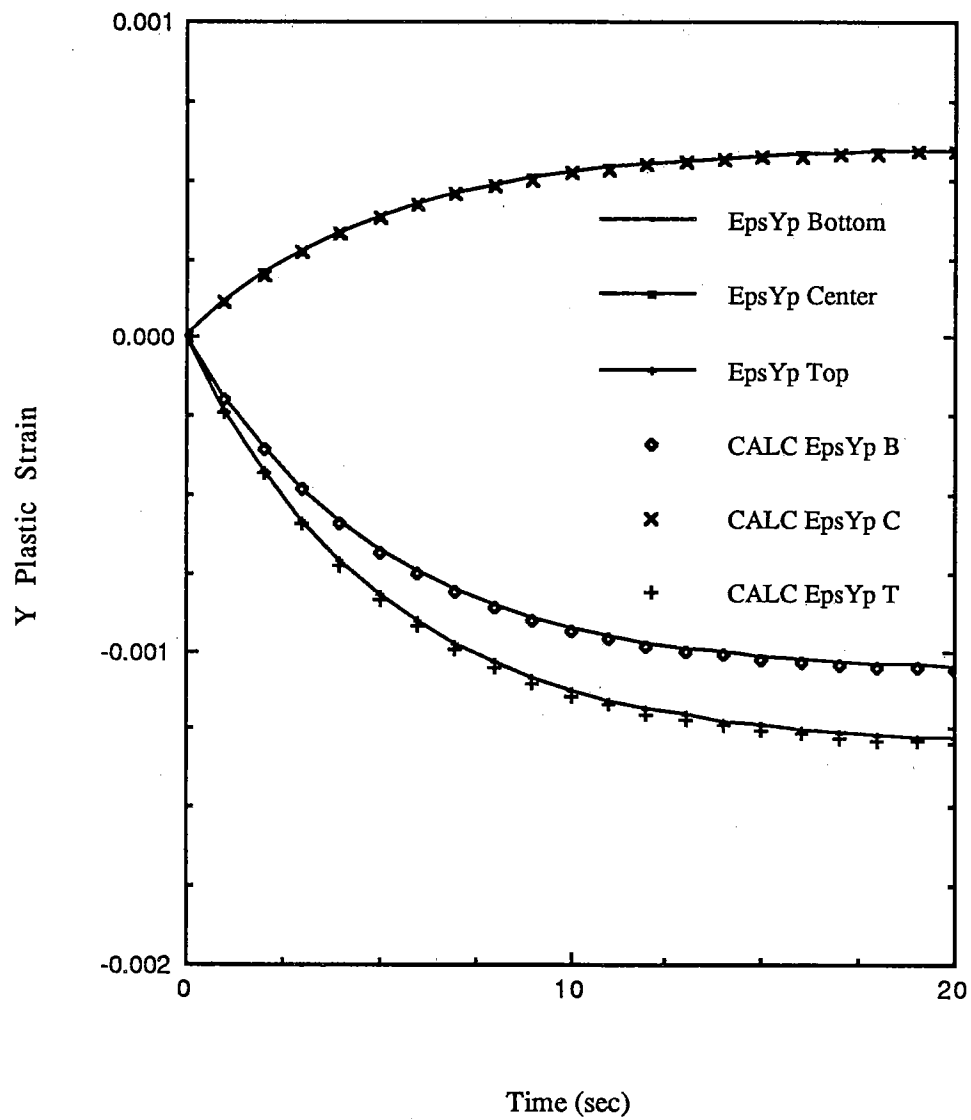


Figure 10. Comparison of y-plastic strain from analytical solution and finite element model.

4. APPLICATION TO HOT CHARGING

The No. 1 slab caster of Inland Steel Indiana Harbor Works was modeled to provide realistic physical dimensions. The caster is a two-strand, curved mold machine of DEMAG design, and has a radius of curvature of 12.2 meters. A schematic diagram of the secondary cooling system is shown in Figure 11. It has five main water spray zones, and has a single unbending point. Information concerning these zones and the dimensions of the rollers in each zone were taken from blueprints of the caster [41], and are listed in Table 1. Location of the individual rollers are included in Appendix F. Some rollers in each zone are larger than the rest of the rollers in that zone. This was ignored to simplify the modeling of the secondary cooling region. The machine casts slabs that are 9 1/4" thick and vary from 30" to 72" wide.

Utilizing two-fold symmetry, a mesh was generated for one quarter of a 9 1/4" thick by 36" wide slab, and is shown in Figure 12. The mesh uses a "British jack" arrangement of triangular elements, and is comprised of 392 nodes and 702 elements. The semi-bandwidth of this mesh is 16.

A thin mesh was also generated to examine a one-dimensional slice at the centerline of the wide face of the slab, and is shown in Figure 13. The mesh is the same thickness as the large mesh, but is only 5/8" wide. The elements are similar in arrangement to the previous mesh, but the thin mesh has only 45 nodes and 56 elements, with a semi-bandwidth of 5. Due to the reduced size, this mesh allowed quick simulations to be run to check out the various simulation parameters prior to using the large mesh. For example, a mold run involving plasticity using the large mesh took 10396 CPU seconds,

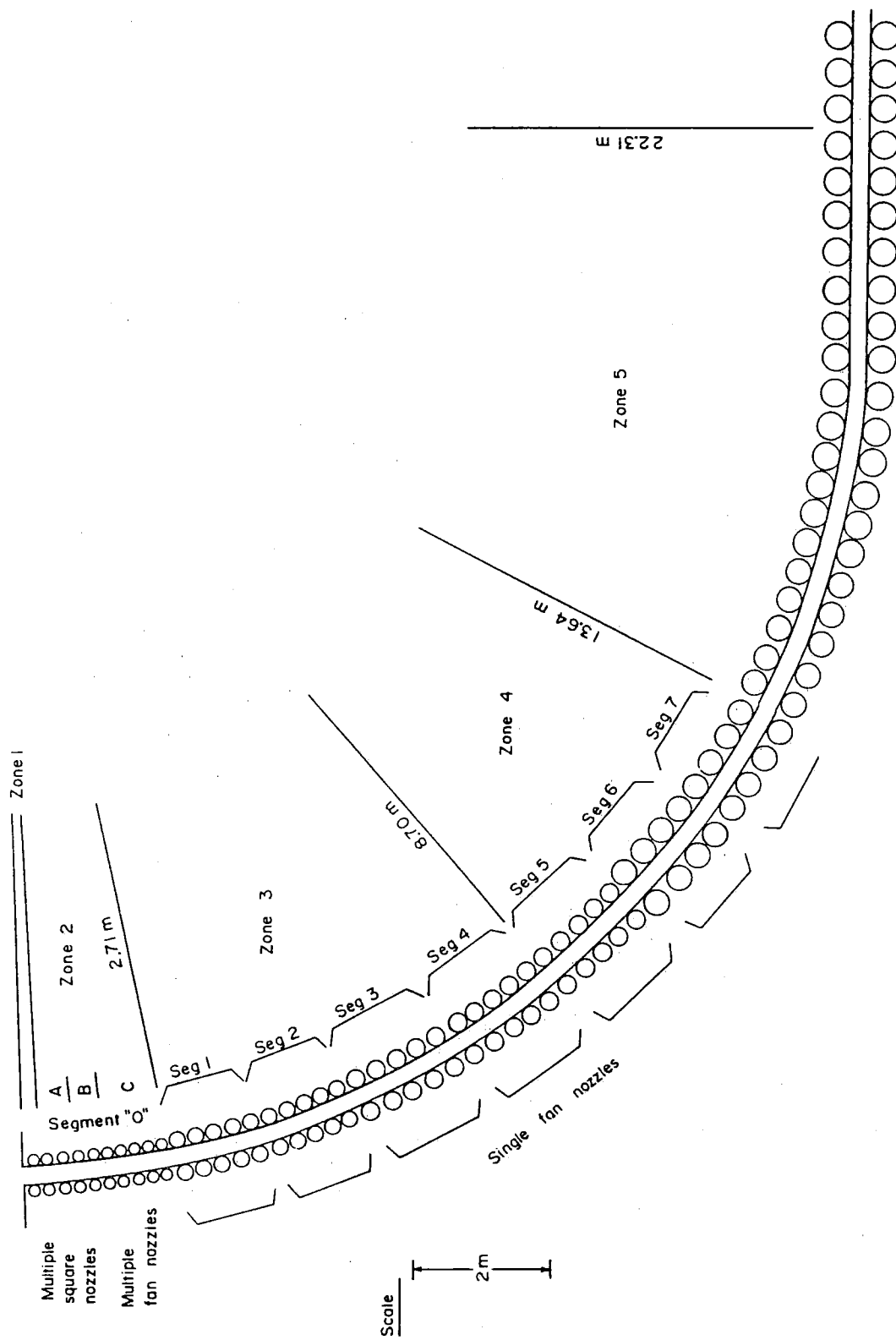


Figure 11. Schematic diagram of secondary cooling system of the Inland Steel No. 1 Slab Caster [19].

Table 1. Specifications of secondary cooling system
of the Inland Steel No. 1 Slab Caster.

Zone #	Distance to start of zone (m)	# of rollers	Roller radius (m)
1	0.60	1	0.064
2	0.94	9	0.086
3	2.71	20	0.127
4	8.70	13	0.162
5	13.64	30	0.222

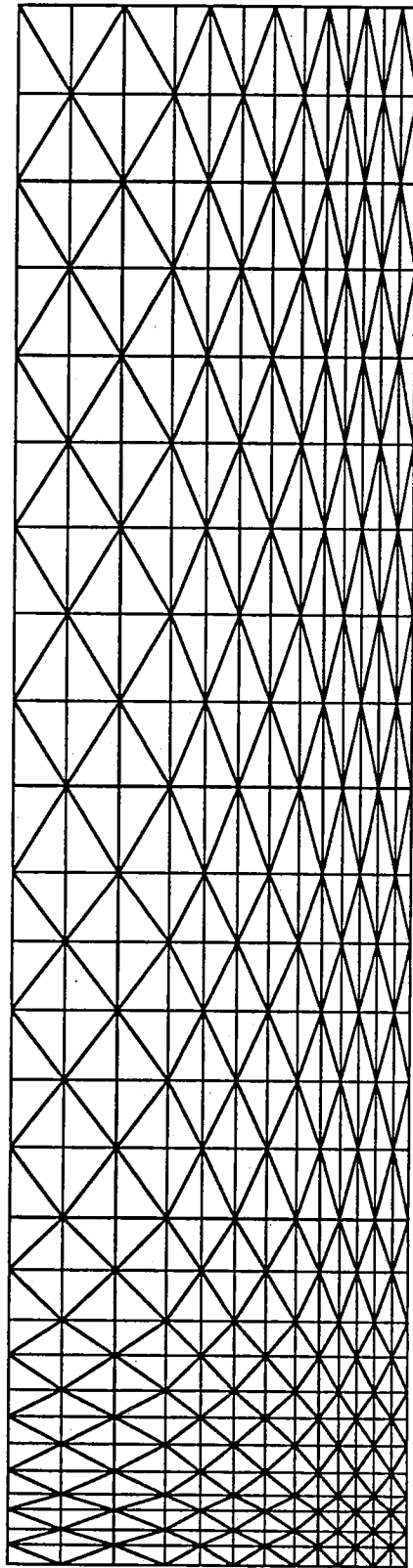


Figure 12. Finite Element mesh for a 9 1/4" by 36" slab of the Inland Steel No. 1 Slab Caster.

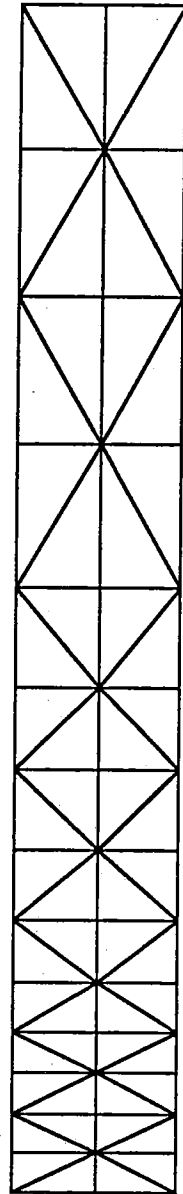


Figure 13. Finite Element mesh for a thin slice at the center of the slab for use in one-dimensional simulations.

while the same run using the thin mesh took 3051 CPU seconds, or just under 3.5 times as fast.

4.1 MATERIAL PROPERTIES

The enthalpy function used in the simulations was taken from previous work with static cast ingots [32]. The function is shown in Figure 14. The latent heat of solidification was assumed to vary linearly across the liquidus, T_{liq} , and solidus, T_{sol} , temperature range. The curve is composed of eight separate functions:

$$T \leq 500 \quad H_I = -23.3 + 0.456 T + 1.88e-4 T^2 \quad (25)$$

$$500 < T \leq 800 \quad H_I = 13.4 + 0.268 T + 4.18e-4 T^2 \quad (26)$$

$$700 < T \leq 750 \quad H_I = -595.0 + 1.431 T \quad (27)$$

$$750 < T \leq 850 \quad H_I = -1348.9 + 3.849 T - 1.883e-3 T^2 \quad (28)$$

$$850 < T \leq 1150 \quad H_I = 11.7 + 0.648 T \quad (29)$$

$$1150 < T \leq T_{sol} \quad H_I = 228.3 + 0.268 T + 1.67e-4 T^2 \quad (30)$$

$$T_{sol} < T \leq T_{liq} \quad H_I = H_I + 272.0(T - T_{sol})/(T_{liq} - T_{sol}) \quad (31)$$

$$T_{liq} \leq T \quad H_I = 97.5 + 0.787 T \quad (32)$$

where H is in kJ/kg, and T is the temperature ($^{\circ}\text{C}$).

The steel modeled had a 0.15% carbon content. Density was assumed to be a constant value, 8000 kg/m³. The liquidus and solidus temperatures were 1513 $^{\circ}\text{C}$ and 1487 $^{\circ}\text{C}$, respectively. Poisson's ratio, ν , was 0.30.

Figure 15 shows the thermal conductivity used in the simulations. The convection in the liquid pool was modeled by artificially raising the thermal conductivity of the liquid steel by a factor of 1.5. The equations used to form this function are as follows:

$$T \leq 800 \quad k = 59.4 - 0.0418 T \quad (33)$$

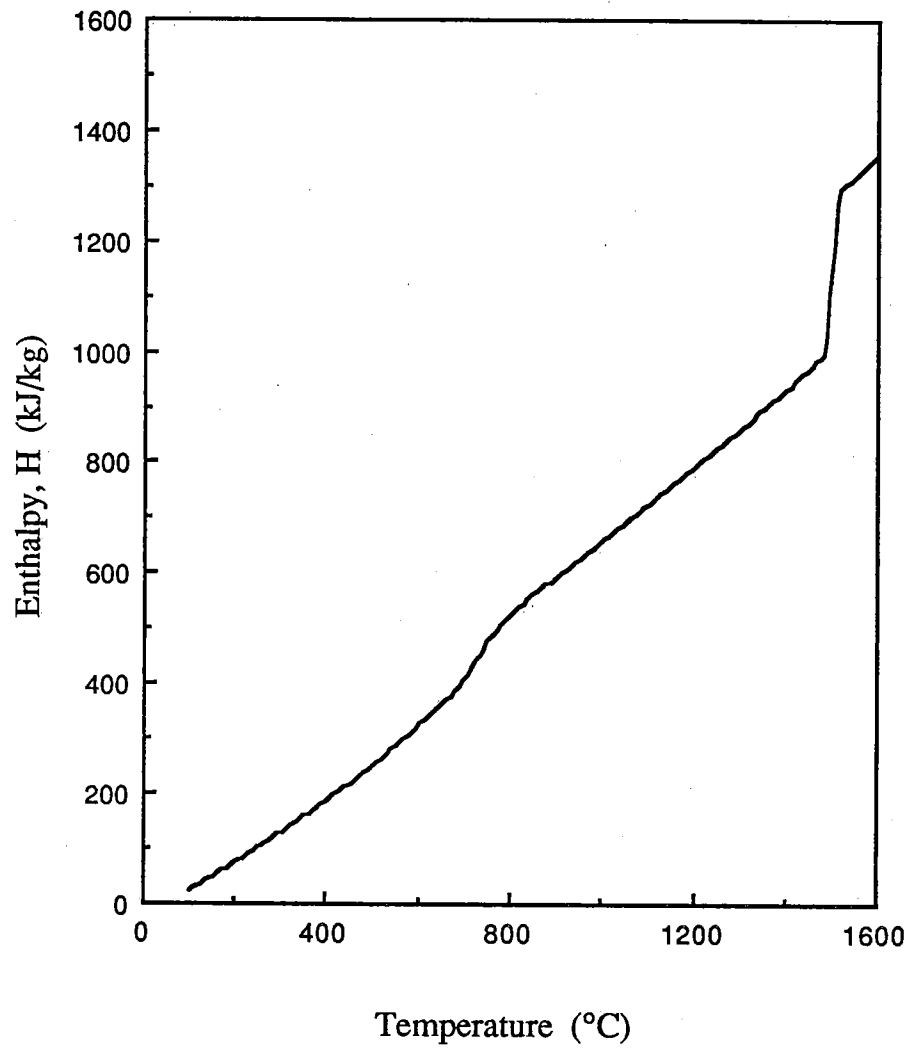


Figure 14. Enthalpy function for steel used in the heat transfer model.

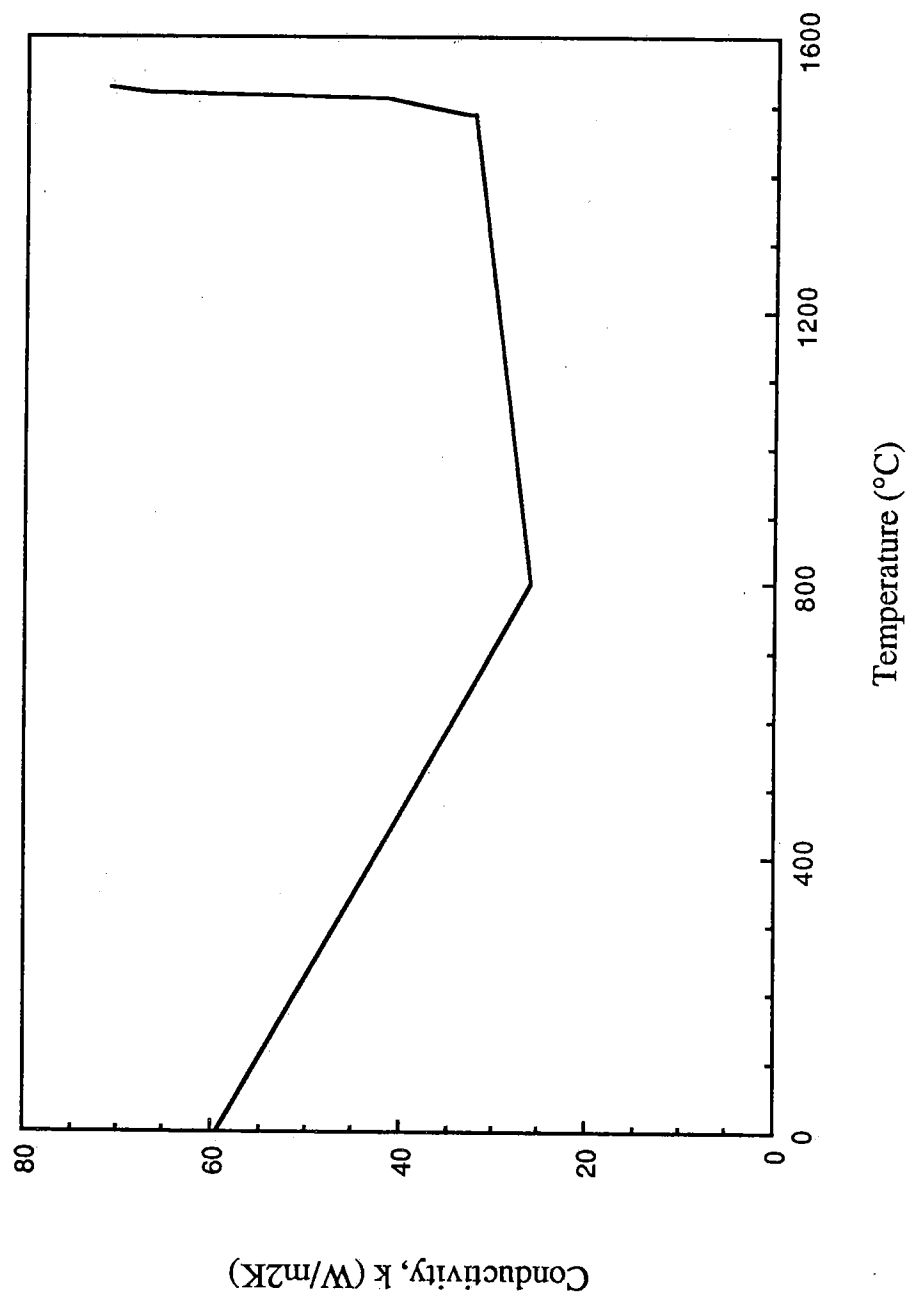


Figure 15. Thermal conductivity function for steel used in heat transfer model.

$$800 < T \leq T_{sol} \quad k = 18.4 + 0.0094 T \quad (34)$$

$$T_{sol} < T \leq T_{liq} \quad k = 32.5 + 10.0(T - T_{sol})/(T_{liq} - T_{sol}) \quad (35)$$

$$T_{liq} \leq T \quad k = 32.5 + 10.0(T - T_{sol})/(T_{liq} - T_{sol})^{1.5} \quad (36)$$

where k is in W/mK, and T is the temperature ($^{\circ}\text{C}$).

As discussed earlier, the thermal linear expansion (TLE) is formulated to allow the temperature dependence of α_T as well as the volume change of the steel due to the $\alpha \leftrightarrow \gamma$ transformation. The phase transformation kinetics, or time-dependency of the transformation, is included in the model through the following equations:

$Ar_1 < T < Ar_3$, cooling

$$\% \gamma = 50 \cos \left[\pi \frac{(Ar_3 - T)}{(Ar_3 - Ar_1)} \right] + 50 \quad (37)$$

$Ac_1 < T < Ac_3$, heating

$$\% \gamma = 50 \cos \left[\pi \frac{(Ac_3 - T)}{(Ac_3 - Ac_1)} \right] + 50 \quad (38)$$

where (Ar_1, Ar_3) are the transformation finish and start temperatures for cooling, and (Ac_1, Ac_3) are the corresponding transformation temperatures for heating. This simple approach is effective in calculating TLE in the phase change region. Figure 16 shows the resulting TLE curves for the low carbon steel used in this model. Also included on the graph are the four transformation temperatures for cooling and reheating.

The incremental plastic strain rate function used in this model was taken from concurrent research [42]. The general form of the equation is:

$$\dot{\epsilon}_p = A \exp(-Q/RT) |\sigma - m\epsilon_p^c|^{n-1} (\sigma - m\epsilon_p^c) \quad (39)$$

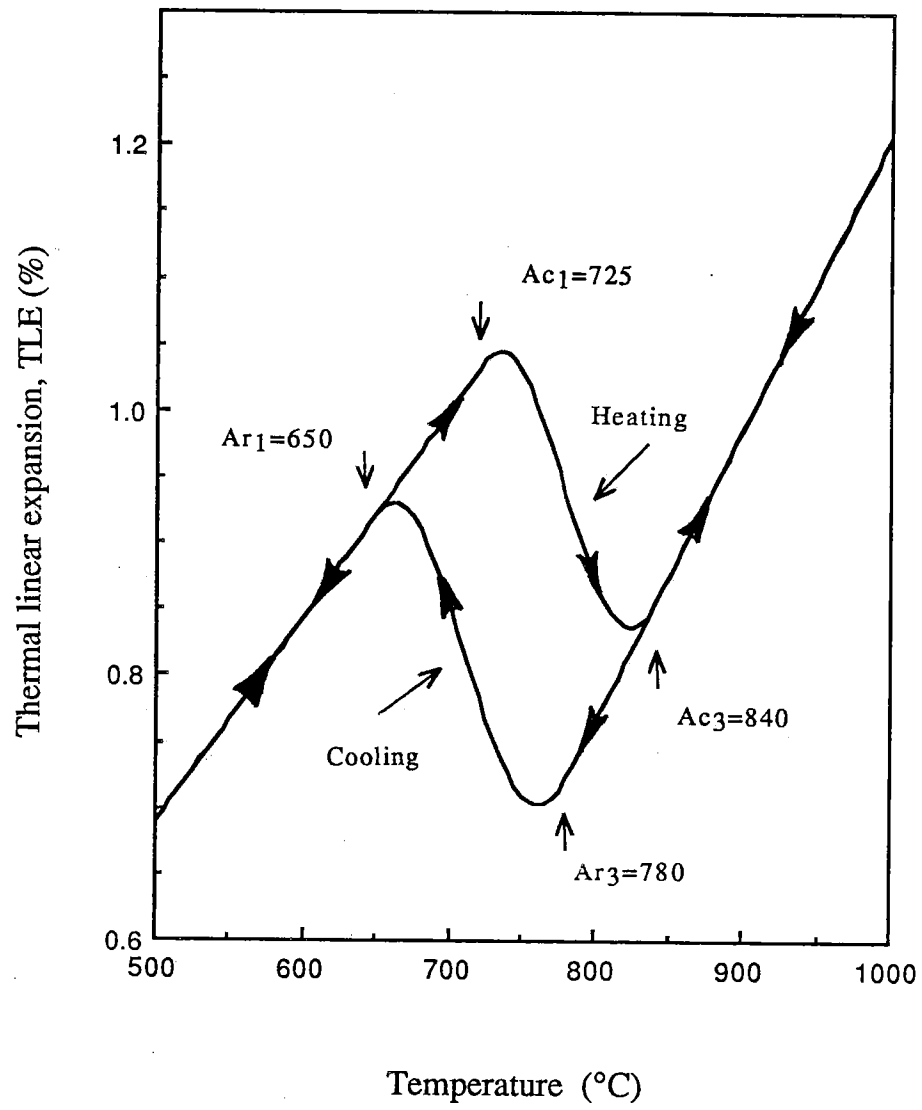


Figure 16. Thermal linear expansion function for steel used in the stress model.

where A, Q, R, m, c, and n are specified in Table 2, σ is the effective stress in MPa, ϵ_p is the accumulated plastic strain, and T is the temperature in degrees Celsius.

The function used for Young's Modulus, E, is shown in Figure 17. The equations used to form the curve are as follows:

$$T \leq 800 \quad E = 211.0e3 - 112.5 T \quad (40)$$

$$800 < T \leq T_{less} \quad E = 172.696e3 - 64.62 T \quad (41)$$

$$T_{less} < T \leq T_{sol} \quad E = 2.6297e6 - 1762.65 T \quad (42)$$

$$T_{sol} < T \leq T_{fsol} \quad E = 1.5409e6 - 1030.436 T \quad (43)$$

$$T_{fsol} < T \leq T_{liq} \quad E = 53.9247e3 - 35.64 T \quad (44)$$

$$T_{liq} \leq T \quad E = 1.0 \quad (45)$$

where E is in MPa, T is the temperature (°C), $T_{less} = T_{sol} - 40.0$ °C, and $T_{fsol} = T_{sol} + 0.3*(T_{liq} - T_{sol})$. Above the solidus temperature, the elastic modulus quickly drops off to only 1.0 MPa. This virtually eliminates any formation of stress in the liquid.

4.2 BOUNDARY CONDITIONS

As discussed earlier, the simulation is divided into four regions: mold, sprays, transfer, and reheat. Each zone has unique heat flow and stress boundary conditions and will be discussed separately.

In the mold, a heat flux was applied to the narrow and wide face using the classic equation of Savage and Pritchard [23]:

$$q_s = 2680.0 - 335.0 \sqrt{\frac{z}{u}} \quad (\text{kW/m}^2) \quad (46)$$

Table 2. Parameters used for the plastic strain rate [42].

A	8.0e+5
Q/R	40.0e+3
m	340.0 - 0.146 T (K)
c	0.675
n	4.54

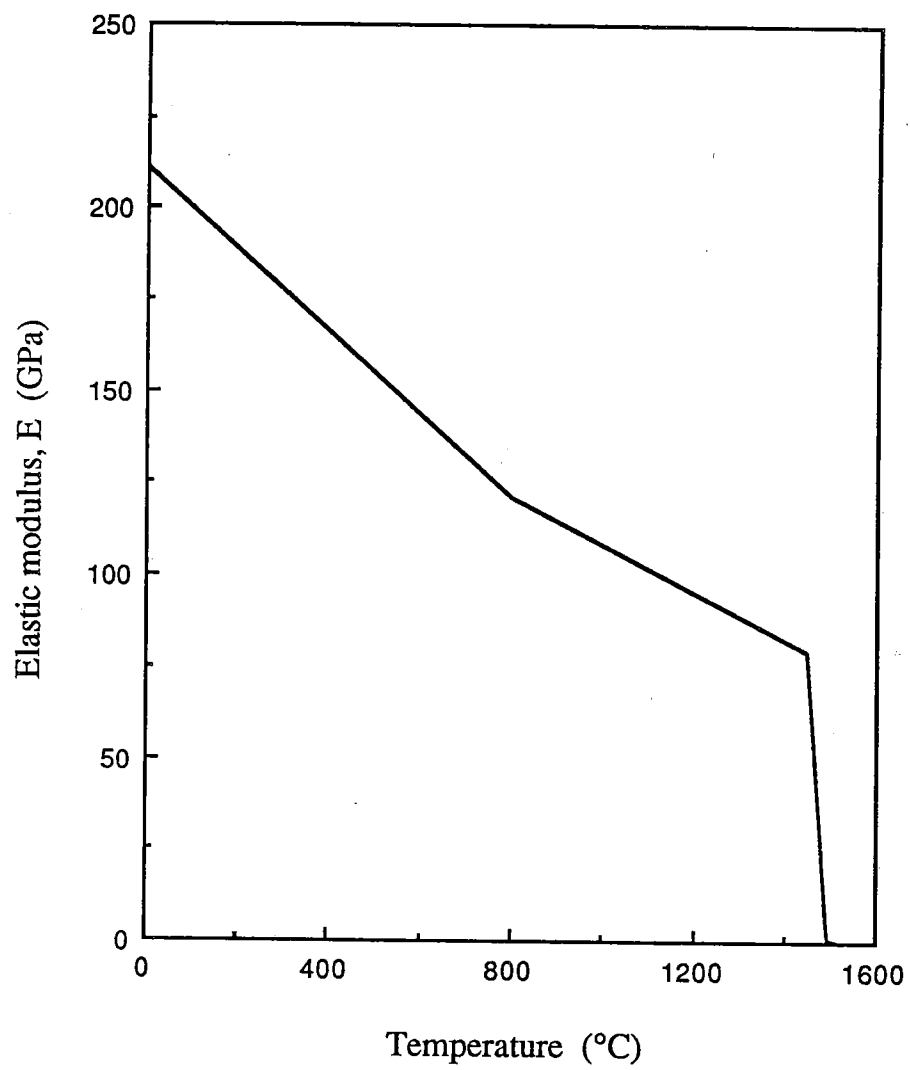


Figure 17. Elastic modulus function used in the stress model.

where z is the distance down the caster (cm), and u is the casting speed (cm/s). This curve was developed for billet molds. A detailed mold analysis including the heat transfer changes due to gap formation and the presence of mold powder in the gap was performed using a finer finite element mesh, and smaller time steps [4]. Figure 18 compares the heat flux out of the mold for this simulation with that of Eq. (46) above and with industrial data based on mold water heat balances [6]. Because of the close agreement between the curves, and due to the intricacies of translating the output from the detailed mold run into a form usable by the coarser mesh, it was decided to use Eq. (46) for the heat flux boundary condition in the mold. The difference in the resulting thermal and stress state in the locations of interest lower in the caster is negligible. To simulate the reduced heat transfer along the narrow face and the corner due to gap formation, the heat flux calculated using Eq. (46) was multiplied by $5/6$ for the narrow face. The first five nodes from the corner along the narrow face, and the first six nodes from the corner along the wide face were also reduced, with the heat flux in Eq. (46) multiplied by $1/3$.

Because the emphasis of the research was not the mold/shell interaction, ferrostatic pressure was not included in the analyses. Thus, the stress boundary conditions were that the left (narrow face) and lower (wide face) sides of the mesh in Figure 12 were left free. The right symmetry plane was constrained in the x -direction, and was unconstrained in the y -direction. The top face (symmetry plane) was constrained in the y -direction and was unconstrained in the x -direction. Thus, the upper right-hand node was fixed in both directions. A state of plane stress was assumed for the z -direction throughout the simulation.

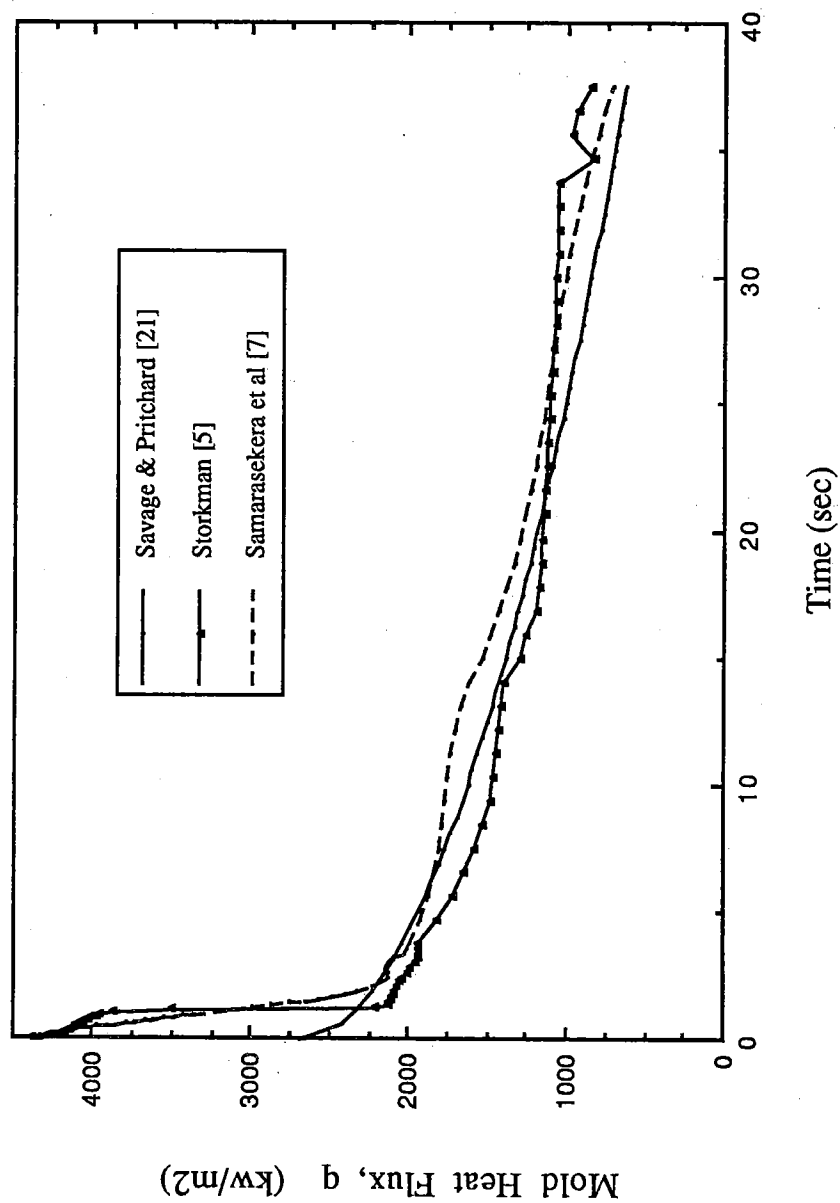


Figure 18. Comparison of mold heat fluxes from three analyses.

Boundary conditions for the thin, one-dimensional mesh in Figure 13 were chosen to simulate plane strain in the y-direction. This assumes that the roll friction along the wide face prevents transverse movement. The thin mesh was unconstrained in the x-direction on the left and right faces, and unconstrained in the y-direction on those faces. The top symmetry plane was constrained in the y-direction and free in the x-direction. The bottom face was unconstrained in both directions. Plane stress was assumed for the z-direction. The two meshes and their constraints are shown in Figure 19.

The spray zone has the most complex heat transfer mechanisms. The strand is alternately exposed to direct water spray, indirect water spray, radiation, and roll contact. This cyclic exposure causes large temperature swings in the surface and thus should be modeled properly to get an accurate picture of the stress and strain on the surface. To accomplish this, the heat transfer boundary condition was divided into two regions: spray impingement and roll contact.

The spray impingement portion was modeled using a thermal convection coefficient, h . Figure 20 shows the wide variability of correlations for h [14]. The correlation of Nozaki et al was chosen for this simulation:

$$h = \frac{1.57W^{0.55}(1-0.0075T_w)}{\alpha} \quad (\text{kW/m}^2) \quad \alpha = 4 \quad (47)$$

where W is the water flux ($\text{l/m}^2\text{s}$), T_w is the temperature of the water, 35°C , and α is an empirical adjustment based on temperature measurements at the straightener. As described earlier, "wetting" of the strand surface causes high localized heat transfer. Below a critical Leidenfrost temperature, in this case

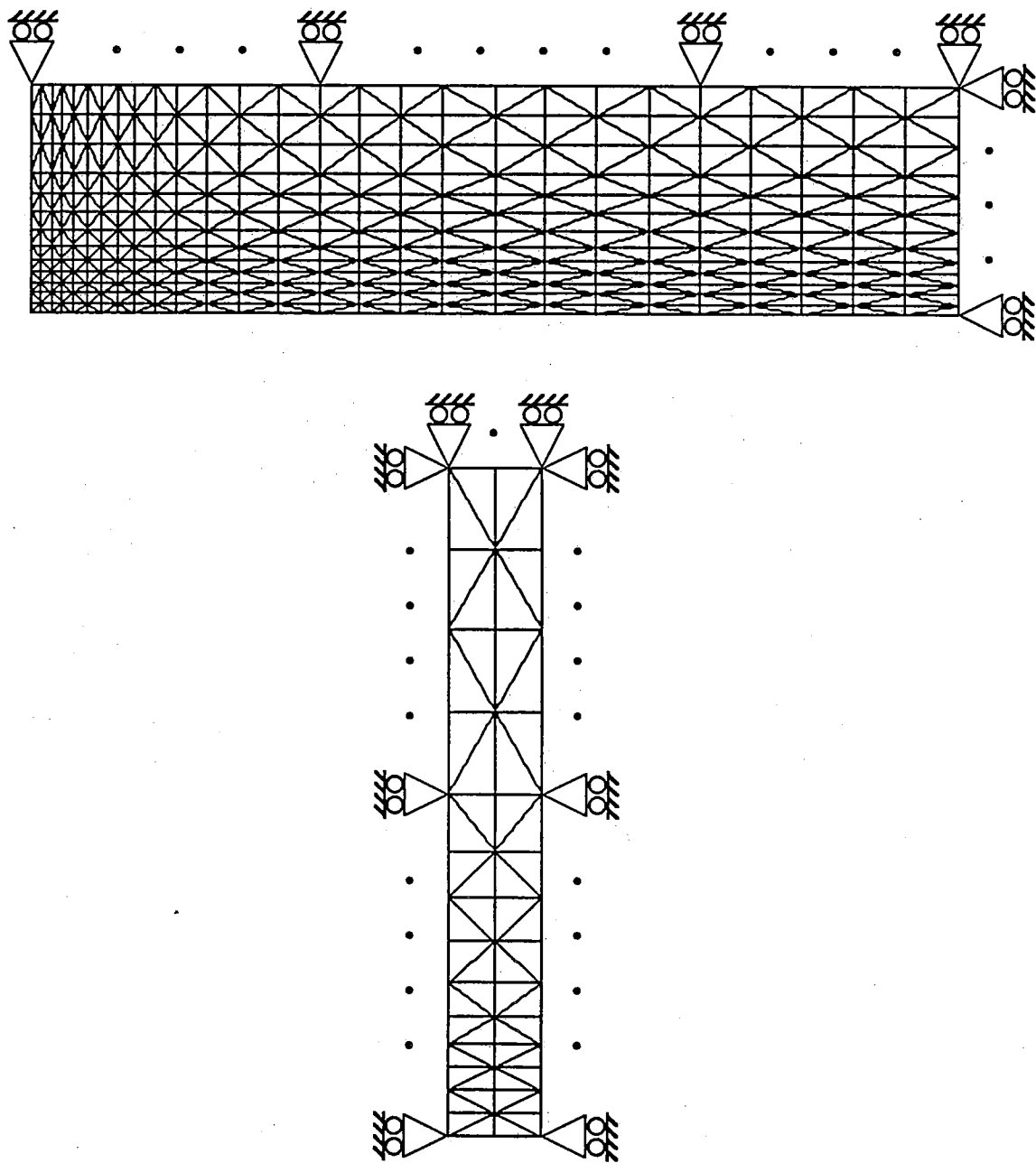


Figure 19. Displacement boundary conditions for the two meshes used in the simulations.

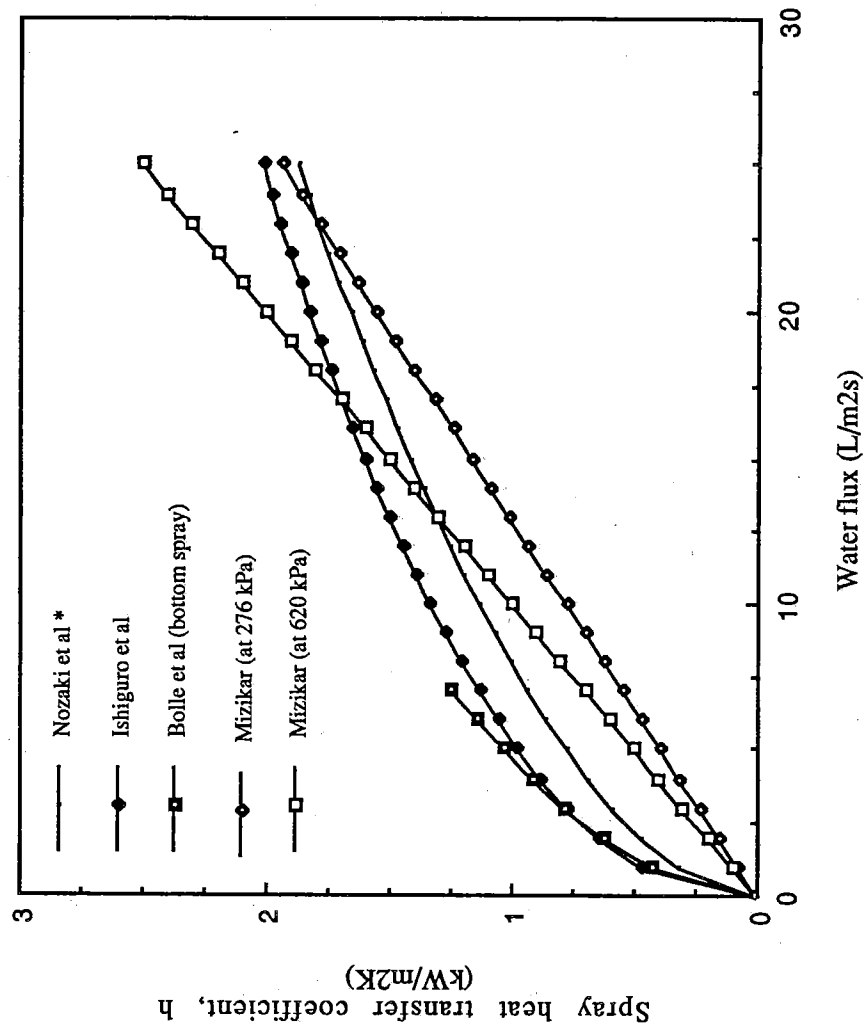


Figure 20. Graph showing wide variability of spray water heat transfer coefficients reported by various researchers. (* used in present research)

550°C, the heat transfer coefficient was rapidly increased in a linear fashion.

This is shown in Figure 21. The linear equation used below 550°C is:

$$h = h_w + 0.04815 h_w (550 - T) \quad \text{if } T < 550$$

$$h = h_w - 0.04815 h_w (T - 550^\circ\text{C}) \quad (\text{kW/m}^2\text{K}) \quad (48)$$

where h_w is the heat transfer coefficient calculated by Eq. (47) above, and T is the surface temperature ($^\circ\text{C}$). This corresponds closely to results reported by Mizikar [12].

The heat transfer due to roll contact was treated as a heat transfer coefficient as well, with its value being determined by the percentage of heat that the rolls are known to extract. The percentages used were taken from Hibbins et al [20], and are presented in Table 3. These data were back-calculated from temperature measurements taken from the No. 1 Inland Steel Slab Caster, Indiana Harbor Works. By knowing the percentage that was removed by the rolls, the heat transfer coefficient for the roll contact region was scaled from the spray impingement heat transfer coefficient. This is explained in more detail in Appendix G. Radiation was also scaled along with the roll/spray water coefficients. Radiation was calculated using:

$$h_{\text{rad}} = \epsilon \sigma (T + T_\infty)(T^2 + T_\infty^2) \quad (\text{kW/m}^2\text{K}) \quad (49)$$

where ϵ is the radiative emissivity, σ is the Stefan-Boltzmann constant, ($5.67\text{e-}11 \text{ kW/m}^2\text{K}^4$), and T_∞ is the temperature with which the strand radiates, 35°C . The emissivity used was .80, which is typical of those found in experimental spray cooling tests [11]. Calculation of the heat transfer due to the roll and sprays in this manner allows the simulation to reproduce the large surface temperature swings without affecting the total amount of heat extracted. Thus, the metallurgical lengths of the simulations remain the same,

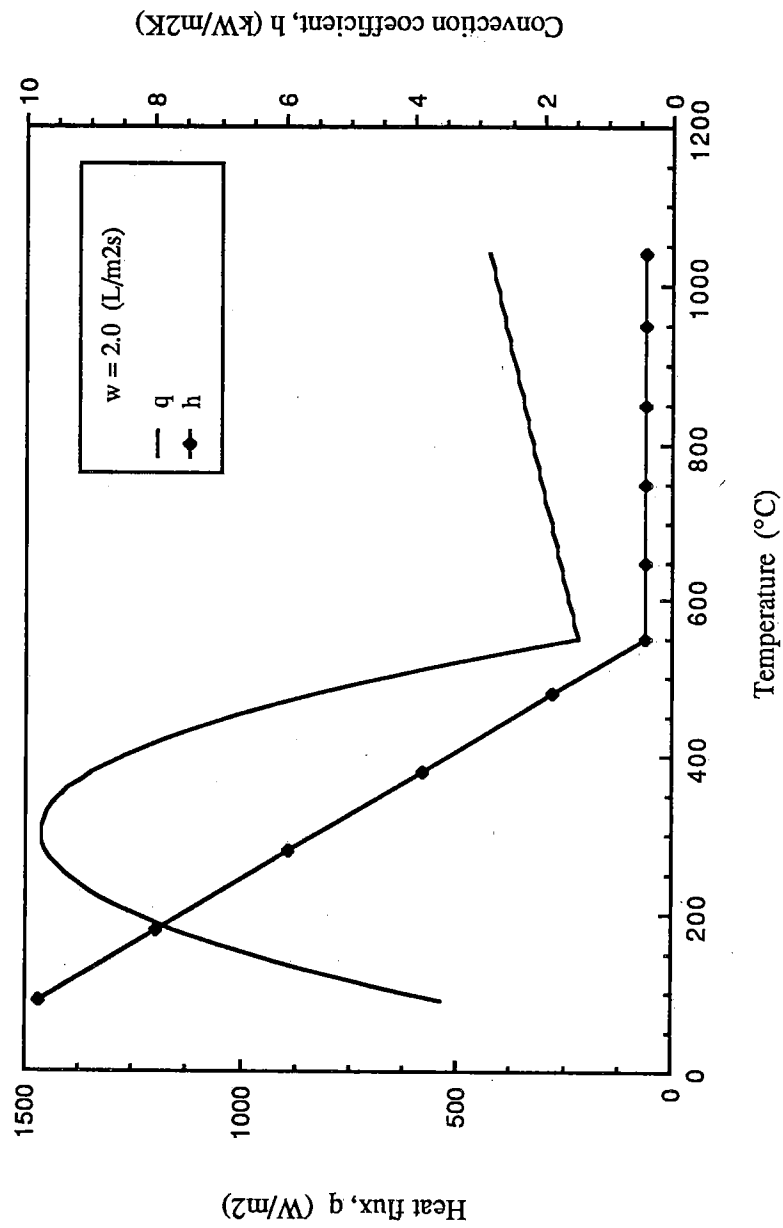


Figure 21. Graph showing relationship of heat flux and heat transfer coefficient assumed by the heat transfer model near the critical Leidenfrost temperature, 550°C .

Table 3. Percentages of heat removed by rollers
in each spray zone.

Zone #	% Contribution to heat extracted by rollers
1	1
2	8
3	22
4	20
5	36

and are not affected by changing the percent of heat extracted by each mechanisms. The main parameter affecting the temperature swings on the strand surface is the length of contact with the roll. This is easily modified in the program, but is highly dependent on the amount of bulging between rollers. Higher in the casting machine, the shell will bulge more because the shell is less rigid, however the rollers are closer together. Lower in the machine, the shell is more rigid and bulges less, however the rolls are larger and are spaced farther apart. Because of the lack of information on how long the strand is in contact with the roll, it was assumed that the roll contact length was 10° of the roll. In this way, the contact length varied with roller diameter. The model calculates all of the roller centerlines and their contact lengths. Then, when the model finds that the strand is within the roll contact zone, the heat transfer coefficient is scaled appropriately.

Cooling water on the narrow face is removed after the second spray zone. At that time, only radiation is applied, using Eq. (49) above.

The stress boundary conditions are the same as for the mold regions. Ferrostatic pressure and the resulting bulging of the strand were not analyzed due to the complexities of implementing this condition with the transverse slice. Unbending was also ignored.

In the transfer stage of the process, natural convection and radiation are applied to both faces of the strand. This simulates the most rapid slab cooling process possible, such as might be encountered in a direct rolling line with no insulation of the slab during transfer. The stress boundary constraints are the same as described above for the mold region. Radiation was

calculated using Eq. (49). Radiative emissivity remained at .80, while T_{∞} was 25°C.

Natural convection was calculated separately for the vertical narrow face and the horizontal wide face. This correlation by Churchill and Chu [43] was used for the vertical face:

$$Nu_L = \frac{\bar{h}L}{K} = \left\{ 0.825 + \frac{.387Ra_L^{1/6}}{[1 + (0.492/Pr)^{9/16}]^{8/27}} \right\}^2 \quad (50)$$

On the horizontal face, a correlation by Incropera and DeWitt [43] was used:

$$Nu_L = \frac{\bar{h}L}{K} = 0.15 Ra_L^{1/3} \quad 10^7 \lesssim Ra_L \lesssim 10^{10} \quad (51)$$

Comparisons with radiation calculations in Appendix H verify the need for natural convection in the analysis. Based on these calculations, an average heat transfer coefficient for natural convection from 500°C to 900°C was used:

$$h_{nat} = 8.70 \text{ W/m}^2\text{K} \quad (\text{vertical face}) \quad (52)$$

$$h_{nat} = 9.50 \text{ W/m}^2\text{K} \quad (\text{horizontal face}) \quad (53)$$

The reheat region utilizes only radiation on the wide and narrow faces. A T_{∞} of 1200°C was assumed. The stress boundary constraints were unchanged from the other zones.

5. SIMULATION RESULTS

The results will be presented in separate sections for each region of the simulation: mold, sprays, transfer, and reheat. The casting speed was held constant throughout at 16mm/sec (≈ 1 m/min), with the steel initially at a temperature of 1513°C (10°C superheat). The models were run on three different computers: a Ridge32/130 super-minicomputer, an Alliant mini-supercomputer, and a Cray X-MP/48 supercomputer.

5.1 MOLD

The mold was simulated using both the thin slice mesh (Fig. 12) and the full mesh (Fig. 13). The temperature histories of the corner node {1}, mid-narrow face node {14}, mid-wide face node {379}, and center node {392} is shown in Figure 22. It is interesting to note that both of the mid-face nodes show rapid cooling in the first 10 seconds. However, the two nodes begin to increase in temperature as the interior starts to conduct heat out. Also plotted in Figure 22 is the shell thickness of the wide face centerline as a function of time. The shell thickness at mold exit is 14.2mm. By comparison, the shell thickness using the thin slice mesh with identical boundary conditions is only 13.8mm. Although not extensive, narrow face cooling does effect the shell growth in the mold.

A corresponding stress/strain simulation involving plasticity was also performed. The stress along the centerline of the wide face at mold exit is plotted in Figure 23. As expected, there is little stress in the y-direction, and no stress in the liquid steel. The x-direction stress is tensile, with a maximum at the surface of 9.1 MPa. Comparison to an elastic run with the same

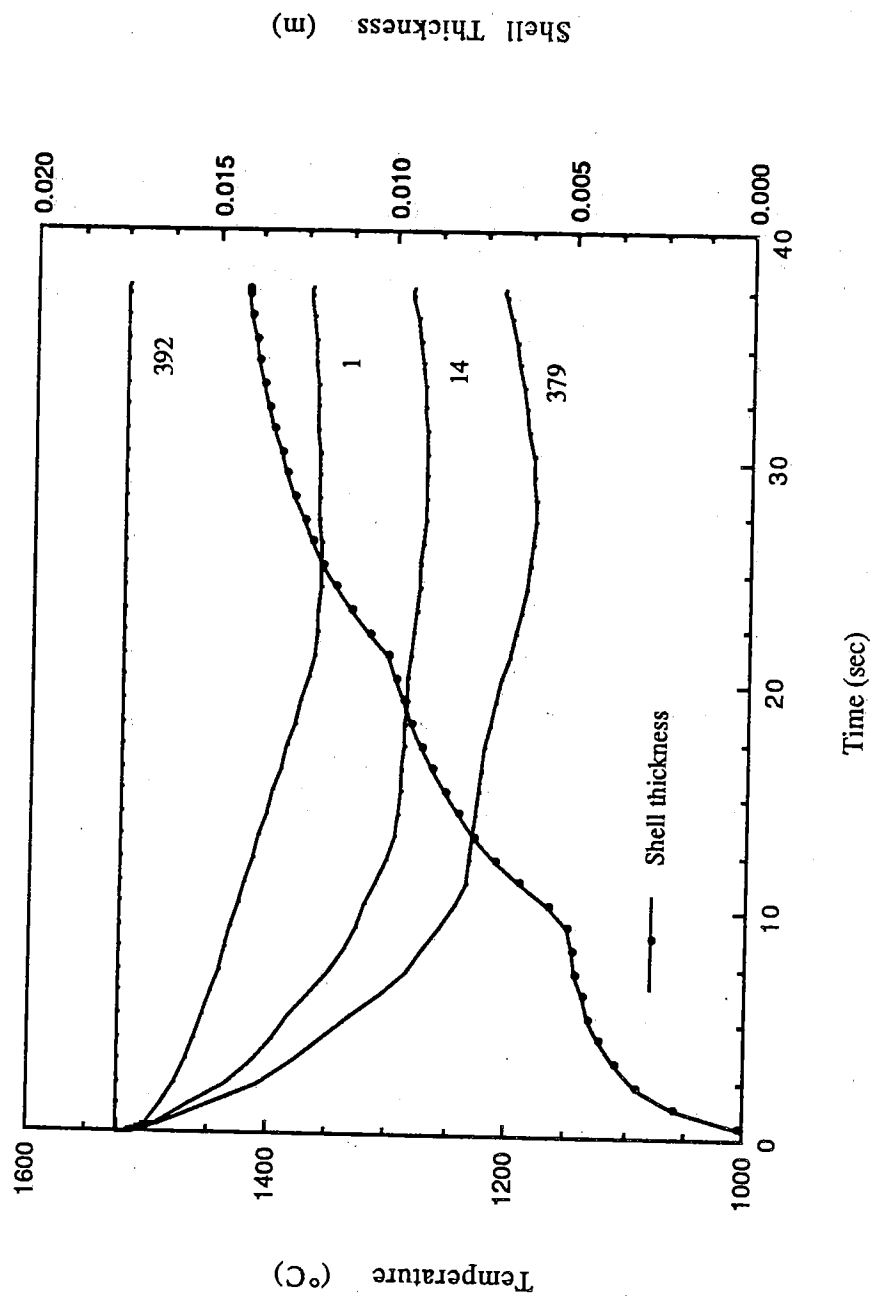


Figure 22. Plot of temperature history for corner node {1}, mid-narrow face node {14}, mid-wide face node {379}, center node {392}, and shell thickness as a function of time.

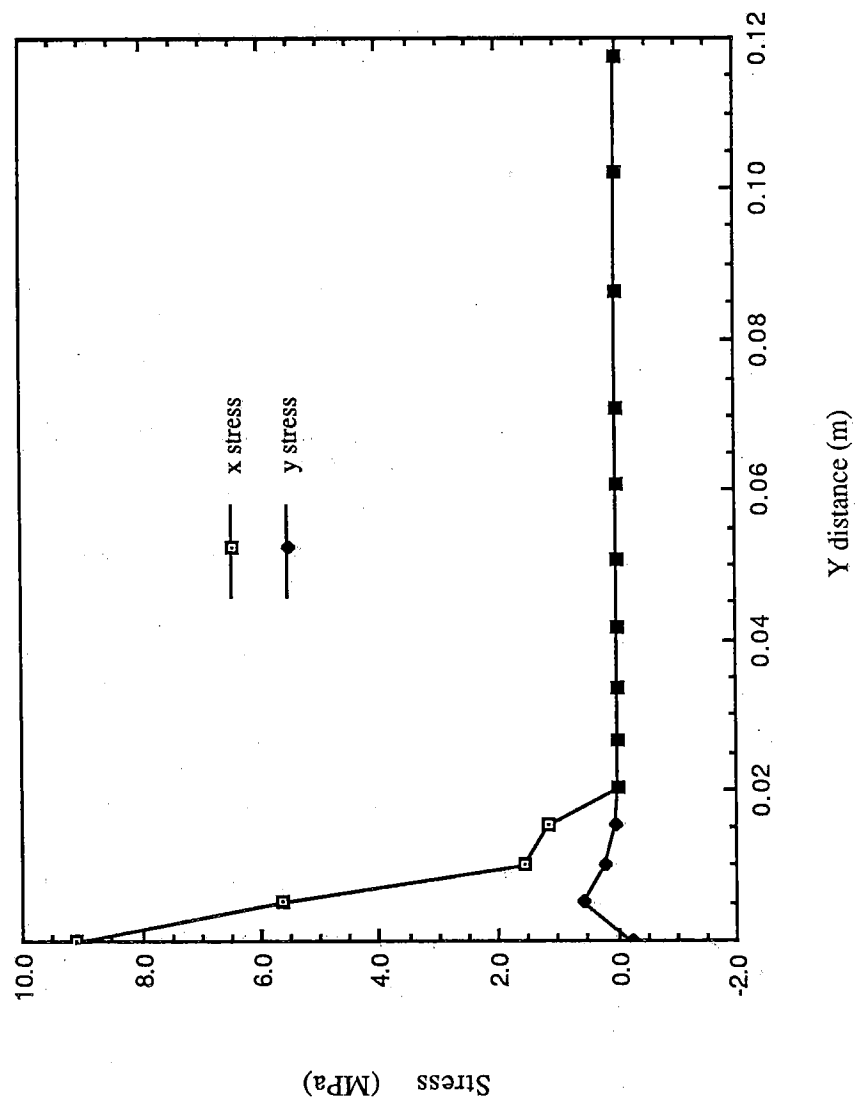


Figure 23. Plot of stress along the centerline of the wide face at mold exit.

boundary conditions is shown in Figure 24. The high surface tension of over 900 MPa clearly shows the need to include plasticity in the mold analysis. The corresponding plastic strain along the wide face centerline at mold exit is plotted in Figure 25. Creep relaxes the high tensile stress in the x-direction by generating plastic strain. To conserve volume, this produces plastic strain in the y-direction as well, resulting in a slight y-direction tensile stress in exchange for vastly reduced x-stresses. As expected, there is no strain in the liquid steel.

5.2 SPRAYS

The spray region of the caster was modeled using both the full mesh and the thin slice mesh, which allowed examination of the two-dimensional heat flow effect on the solidification point. As noted earlier, the narrow face was cooled by water sprays only to the end of the second spray zone, after which only radiation was applied on this face. The temperature history of the sprays is shown in Figure 26. The lack of narrow face cooling is evident as the corner node reheats after exiting the second zone. The surface temperatures oscillate as the slab passes beneath each roll in the caster. This is seen experimentally where the difference in temperature ranges from over 200°C high in the caster to a minimum of 50°C in the lower zones [20]. The corner temperature still oscillates due to the wide face cooling by the sprays. Because of the many time steps involved, not all data points are plotted in Figure 26, giving it a choppy appearance. Figure 27 provides a closer examination of the surface temperature in the first and second zone, and Figure 28 shows the same magnified graph for a portion of the fifth zone. More data points were plotted in each of these graphs to provide a smoother curve. The maximum

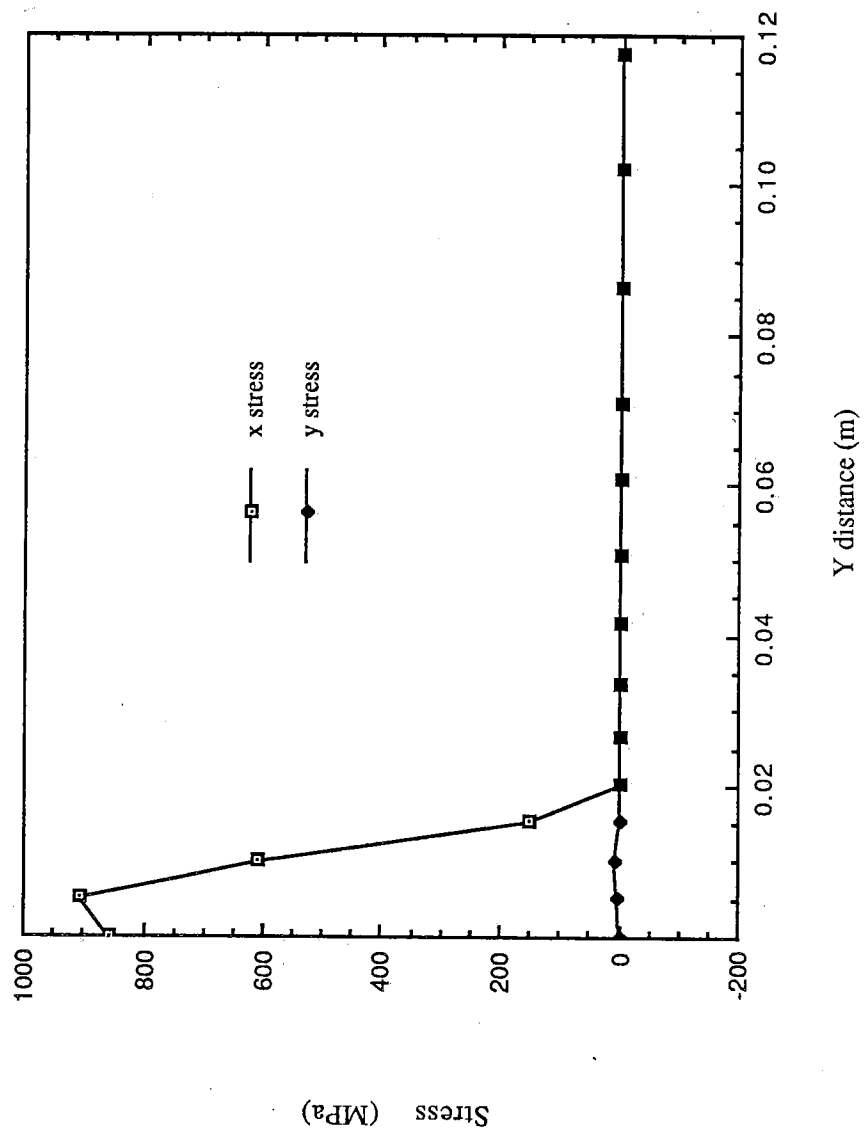


Figure 24. Plot of stress along the centerline of the wide face at mold exit for the elastic mold run.

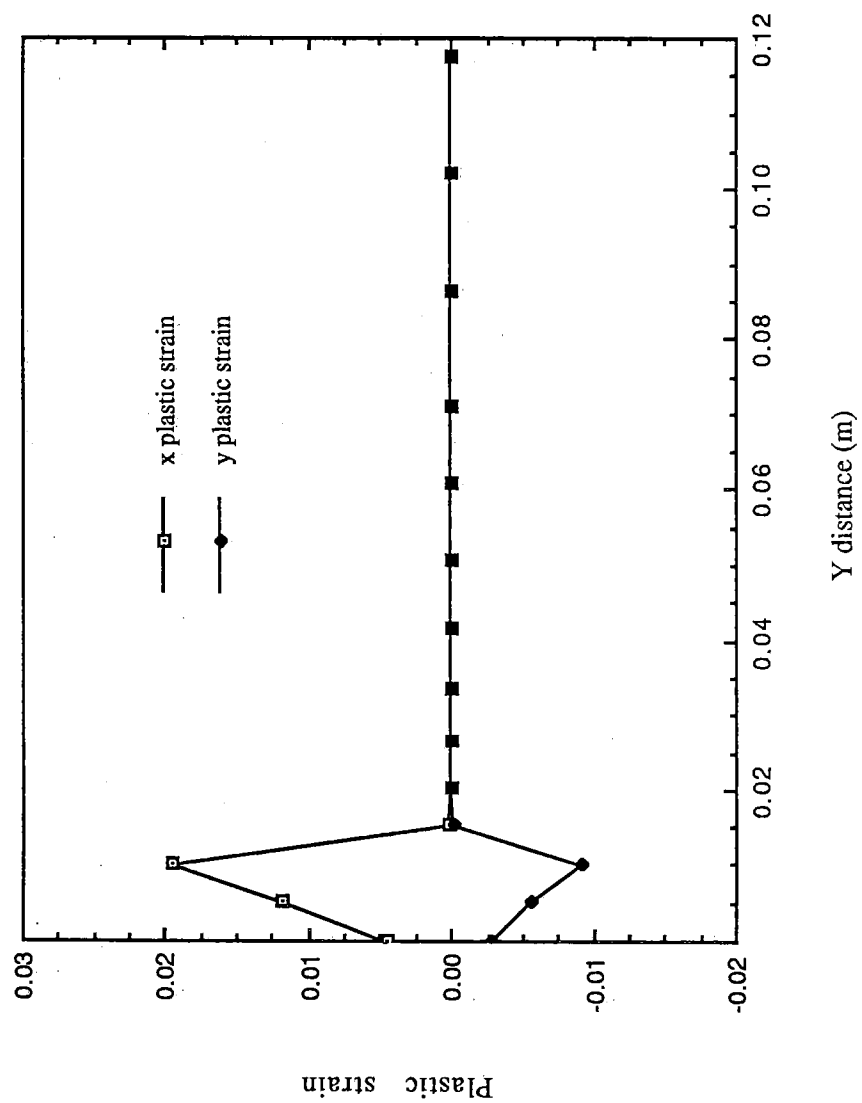


Figure 25. Plot of plastic strain along the centerline of the wide face at mold exit.

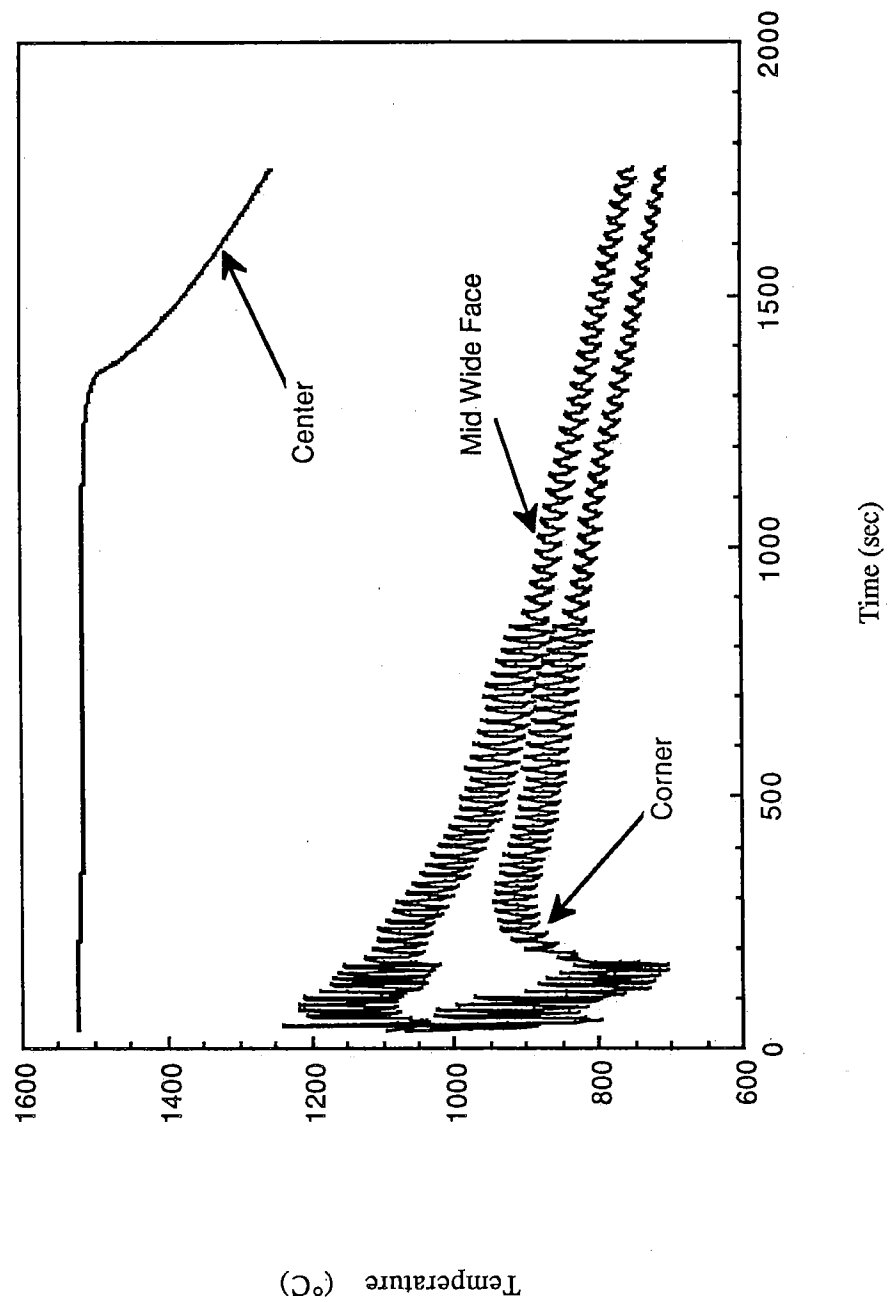


Figure 26. Temperature history of center, mid-wide face, and corner nodes in the entire spray zone.

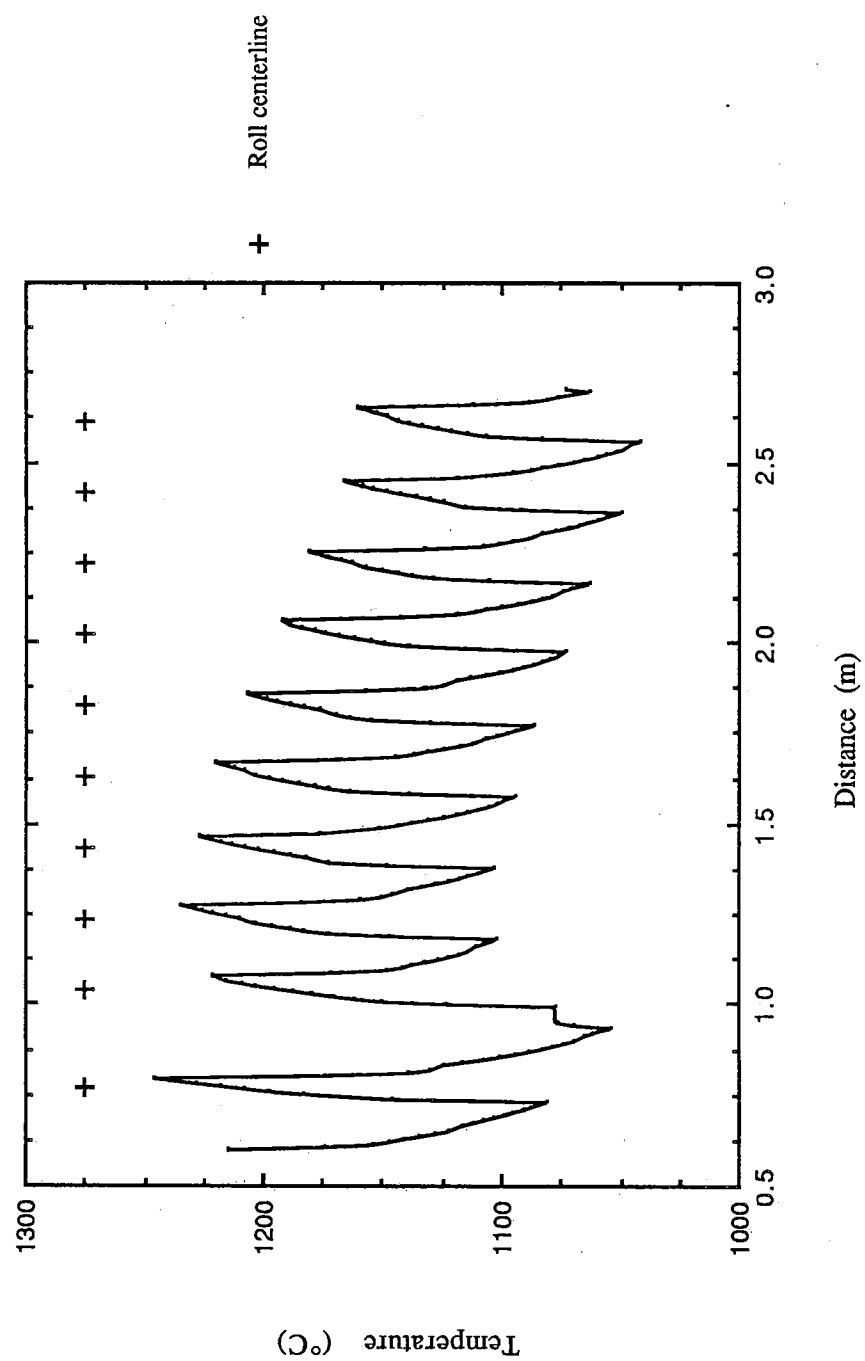


Figure 27. Surface temperature in first and second spray cooling zones.

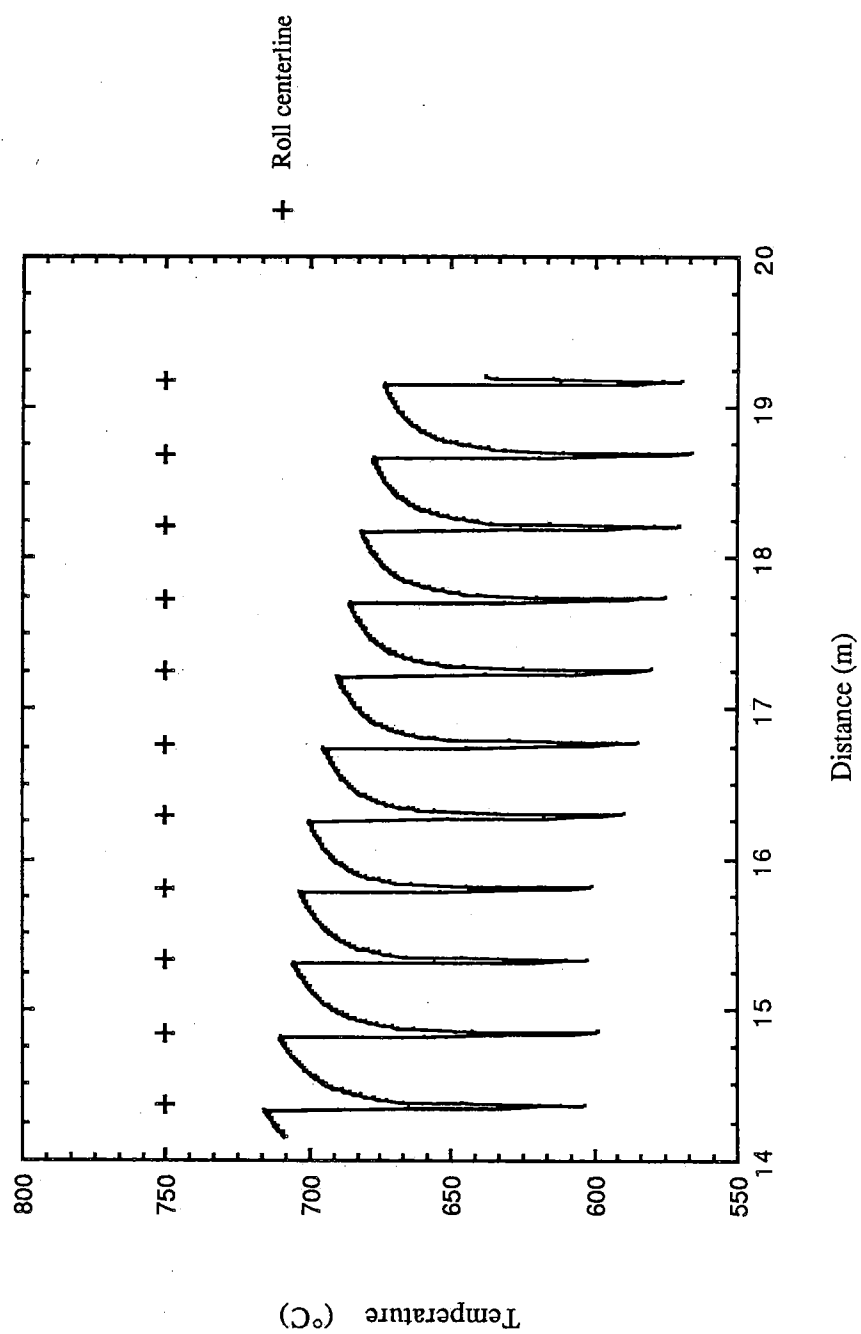


Figure 28. Surface temperature in a portion of the fifth spray cooling zone.

temperature fluctuation is almost 200°C . Also included on the graph are the positions of the roll centerlines. The rollers remove less heat higher in the caster, and extract more heat lower in the caster, which is reflected in Figures 27 and 28. In Figure 27, the regular peaks in temperature correspond to the position of the roll centerline. In Figure 28, this trend is reversed, with the temperature being lower directly under the roller. The magnitude of the change of the surface temperature from roller centerline to the middle of the spray impingement agrees well with the estimates of Hibbins et al [20], as shown in Figure 29. The corresponding plot from the current research is shown in Figure 30. This tends to validate the assumptions made regarding roll heat extraction and on the length of roll contact. Interestingly, the shape of the peaks in the present work is much sharper. Experience showed that varying the roll contact time greatly influenced the surface temperature swings. The estimates of surface temperature in Figure 30 were performed using a casting speed of 26.3mm/s , compared to 16mm/s for the current work. Also, the water flow rate for the current work is $1.75\text{ l/m}^2\text{s}$ in zone 3. Figure 29 shows the resulting surface temperature estimates for two different flow rates. The temperatures predicted by the present model decrease slightly faster than those predicted by Hibbins. This is attributed to the different casting speed and flow rates.

The temperature of the strand at the 10mm depth in the third spray zone is also plotted in Figure 30. As shown, the large temperature swings are restricted to a thin shell near the surface, and interior portions only see small variations in temperature as the kinetics of the heat conduction tends to cushion the temperature peaks. Even nodes as close as 5mm to the surface only see a modest fluctuation of 25°C . This compares with work by Wiesinger

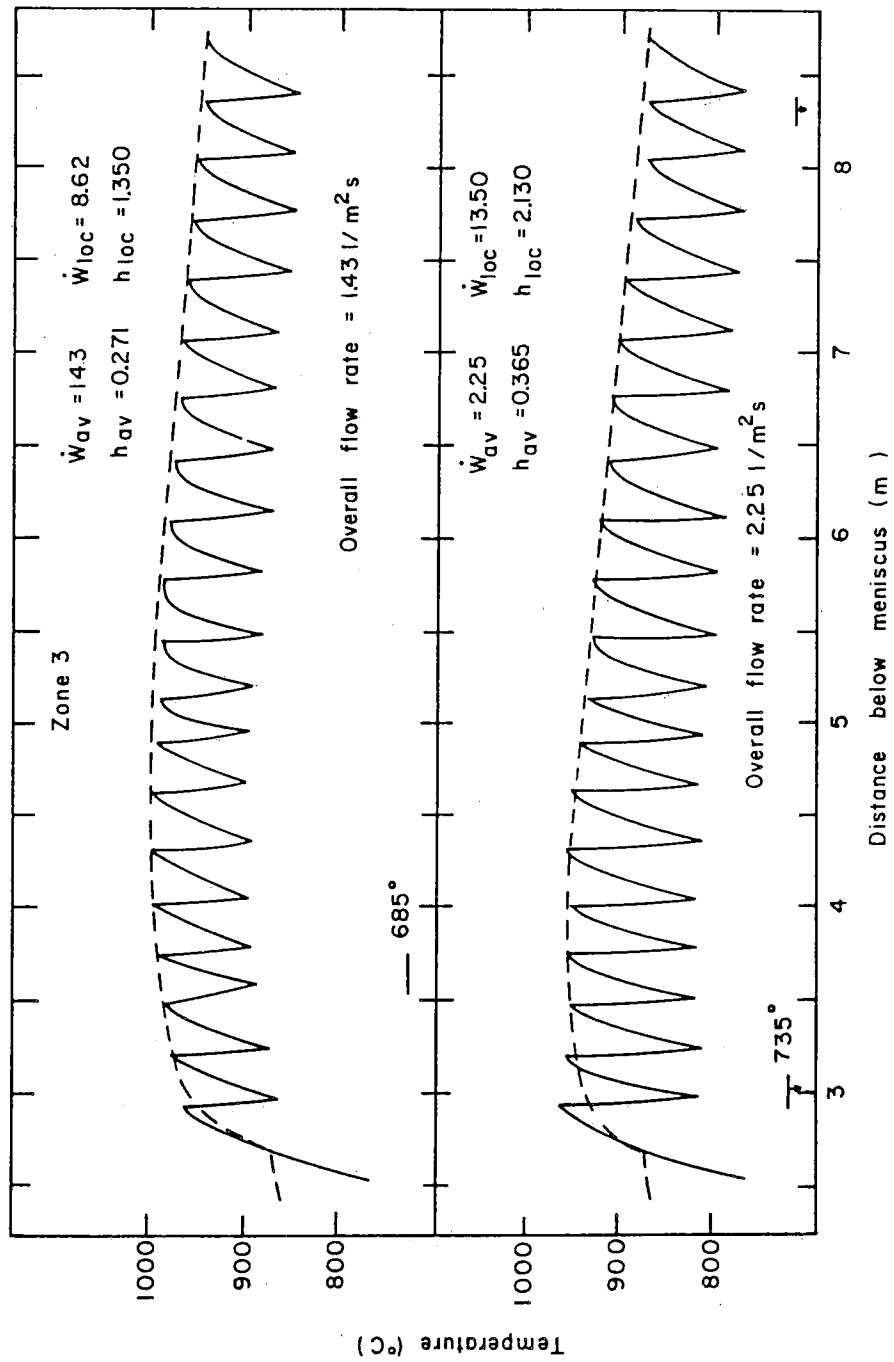


Figure 29. Estimate of actual surface temperature profile for different spray water fluxes in third spray cooling zone [20].

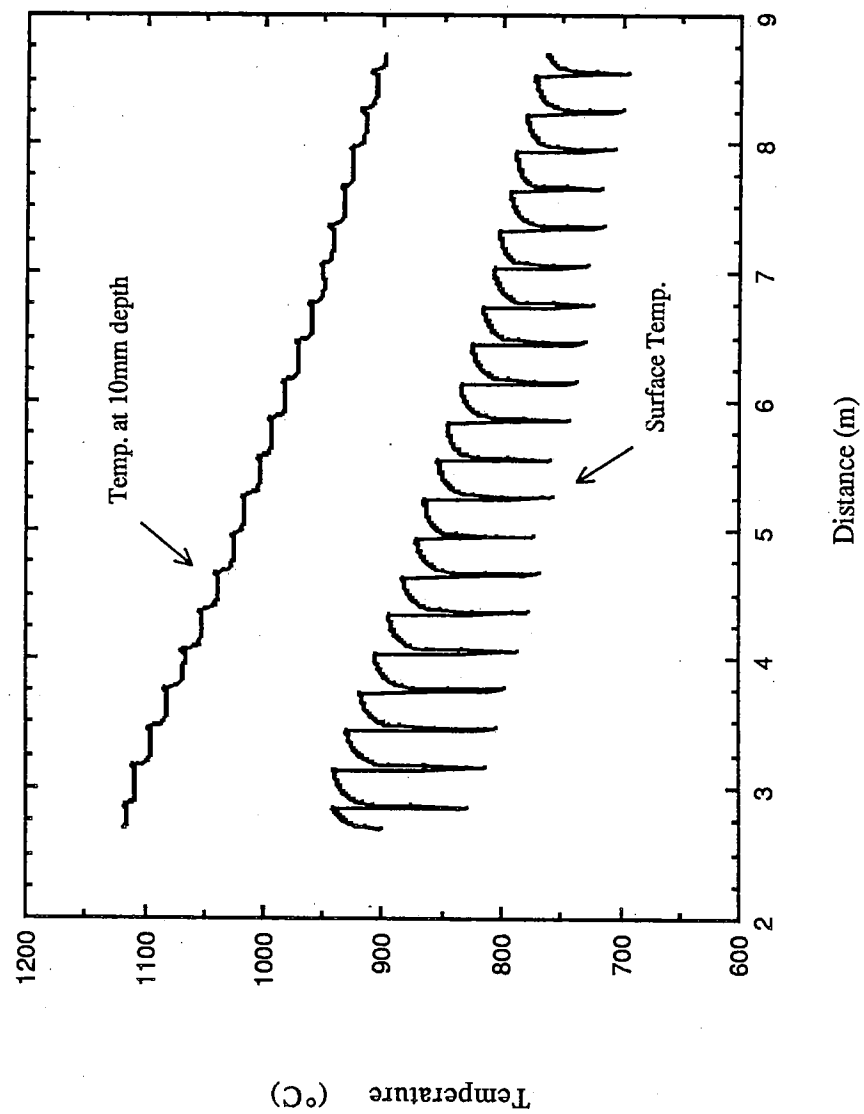


Figure 30. Prediction of temperature profile for surface and 10mm depth in the third spray cooling zone.

et al who found the surface variations to affect only a layer 3mm deep [17]. The discrepancy between the model predictions and Wiesinger's findings cannot be explained since details of the operating conditions were not given.

The calculated metallurgical length for the full mesh was 18.33m and was 18.81m for the thin mesh. Although these two values are very close, as expected, the thin mesh does predict a longer metallurgical length due to the absence of narrow face cooling. This simulation maximized the narrow face temperature, similar to the practice of insulating the narrow face in the caster to retain heat [2]. In normal operation, higher cooling of the narrow face may occur due to water run-off or overspray from the wide face. Figure 31 shows the predicted shell growth. The predicted metallurgical length agrees well with data from actual operation: roughly 19m [41].

The stress runs in the spray zones did not involve plasticity. It was found that the high temperature change required very small time steps to converge, and thus it became infeasible to simulate the region due to the excessive runtimes involved. However, an elastic stress run was performed for the entire spray region. This allows investigation of the resulting trends of stress/strain formation, but is clearly inaccurate quantitatively, as shown by the mold runs.

Figure 32 shows the predicted strand taper or y-displacement at the center of the wide face. The rate of taper is quite steady initially, but begins to increase after solidification. Total shrinkage of the slab at the end of the caster is seen from this figure to be $2 \times 1.2 = 2.4\text{mm}$. This compares with 3.3mm based on calculations using the average temperature in the mold and at the caster exit and their corresponding thermal expansion coefficients.

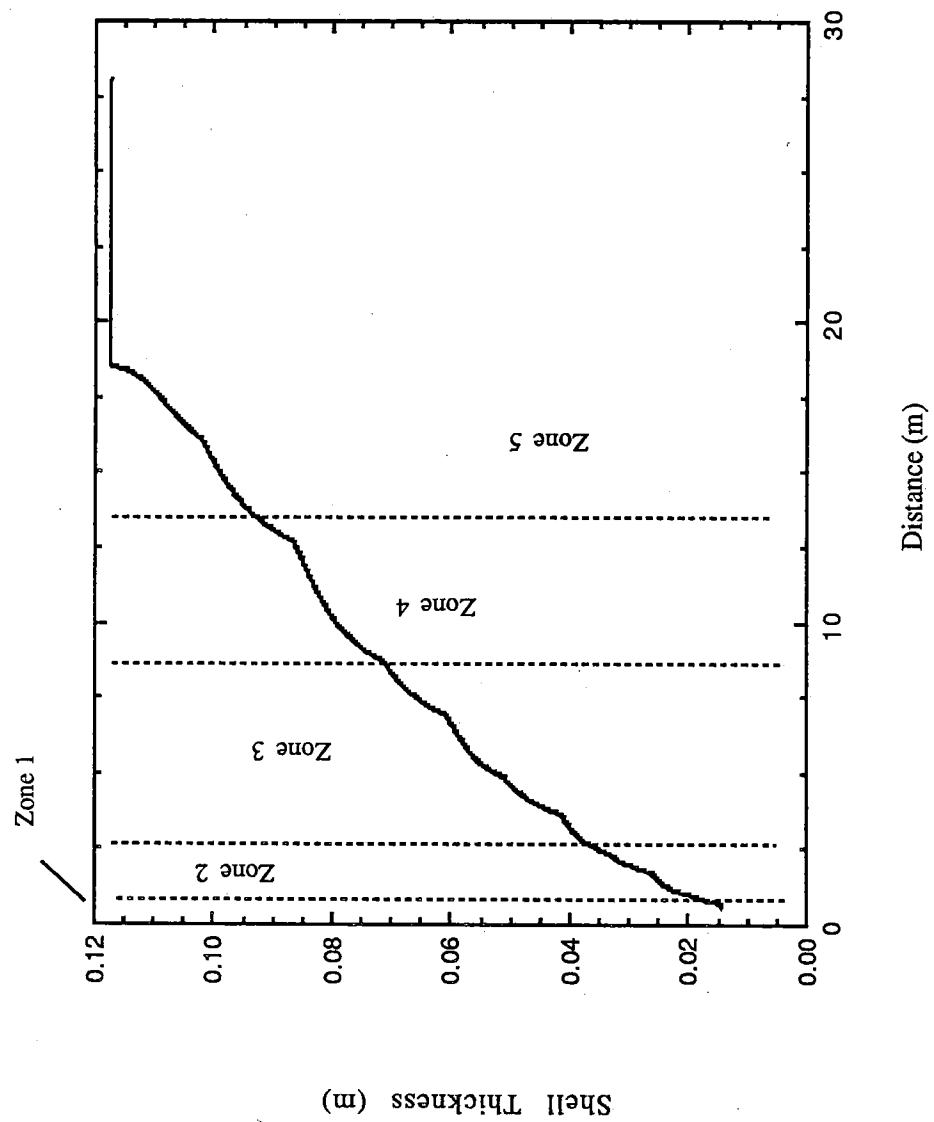


Figure 31. Predicted shell thickness of steel strand in spray cooling zones.

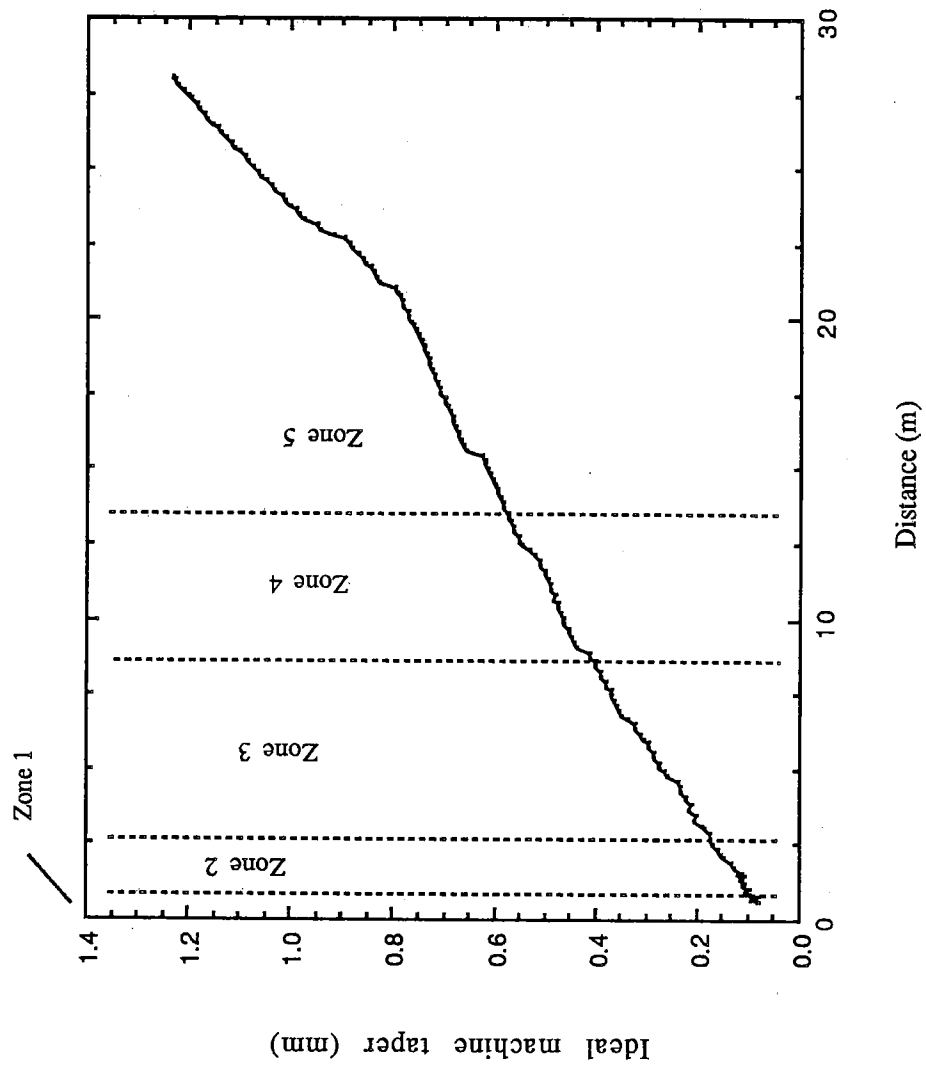


Figure 32. Predicted taper in the spray cooling zones.

Figures 33 and 34 show the stress along the wide face and narrow face centerlines, respectively, at the unbending point, 19.15m. Although the stress magnitudes are well beyond the yield range, this figure does show the majority of the strand exterior to be in tension. The surface stress also oscillates as the slab passes beneath each roll in the caster, with fluctuations between 1150 and 1250 MPa near the unbending point, with the stress less tensile under the roller.

The unreasonable elastic stress and thermal state at the exit of the caster is shown in Figure 35. The temperature contours reflect the removal of cooling on the narrow face. The contours have started to flatten out and the heat flow is approaching a one-dimensional flow case. The slab is almost fully tensile, with only the corner experiencing some slight compression. Finally, just the corner region is starting to transform to α (ferrite and pearlite).

5.3 TRANSFER

The transfer region was simulated until the steel slab was near room temperature which was reached at approximately 13 hours from the time of caster exit. Due to the previously discussed limitations in modeling plasticity in the spray zones, the transfer region was modeled from an initial stress-free state. This assumption ignores the stresses and strains created in the spray zones, but the inability of the transverse slice to model bulging and unbending would limit its usefulness anyway.

Figure 36 shows the temperature histories for the center, mid-wide face, and mid-narrow face during the transfer region. Further cooling to room temperature was not performed since the slab was almost isothermal at 90°C.

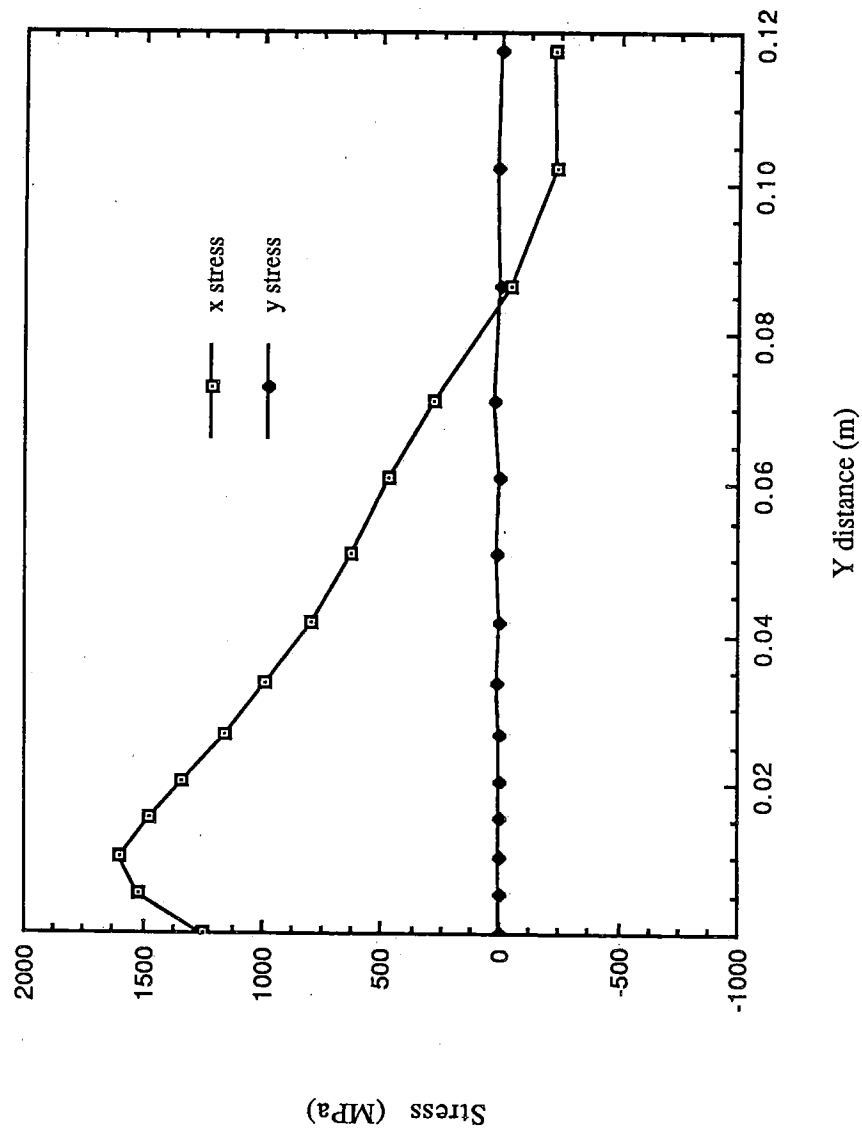


Figure 33. Stress at the unbending point, 19.15m, along the wide face centerline.

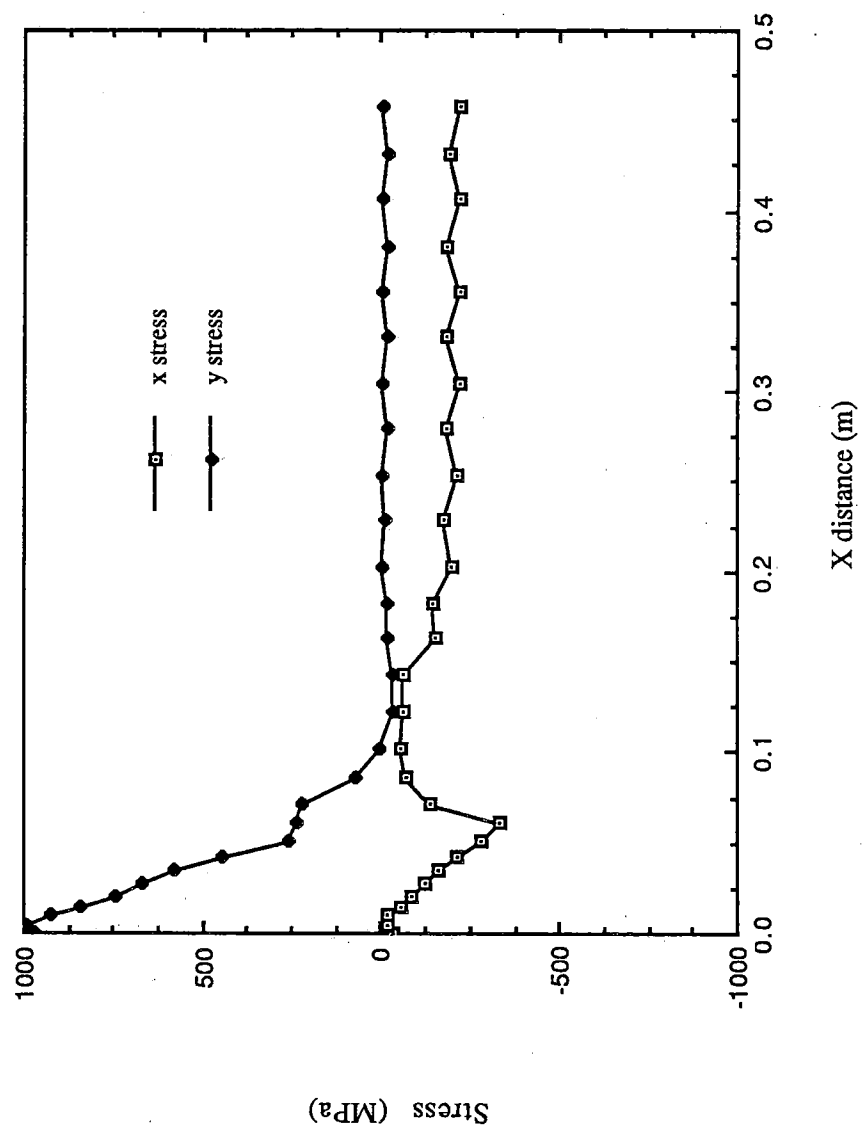


Figure 34. Stress at the unbending point, 19.15m, along the narrow face centerline.

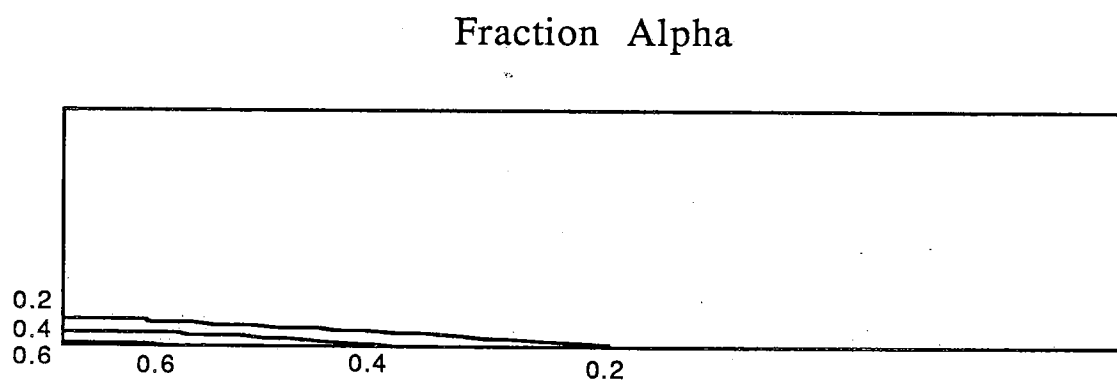
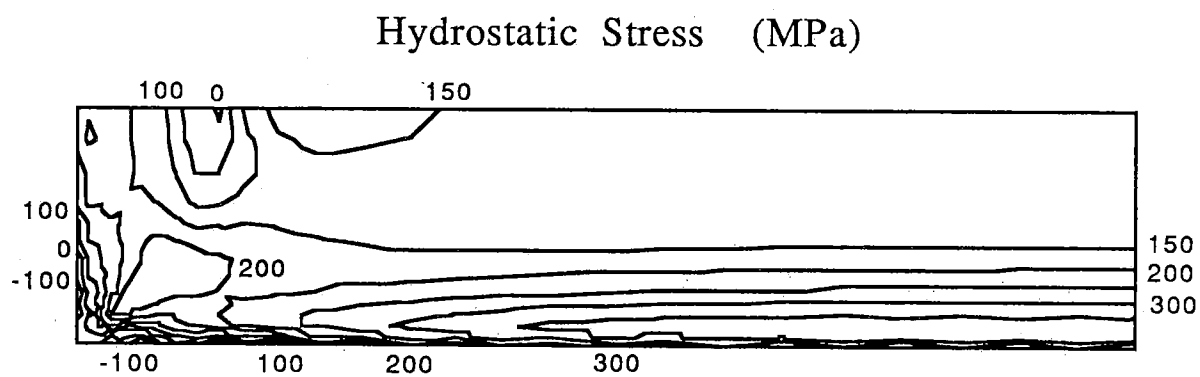
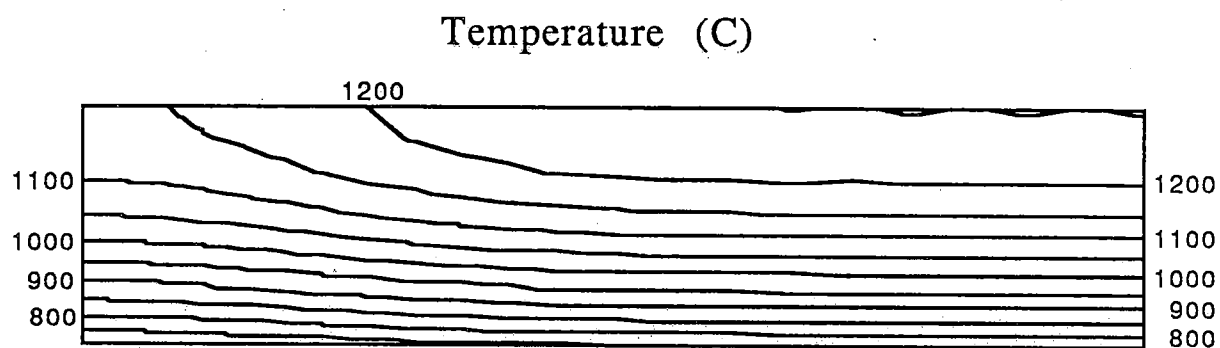


Figure 35. Temperature, hydrostatic stress and fraction alpha contours at caster exit.

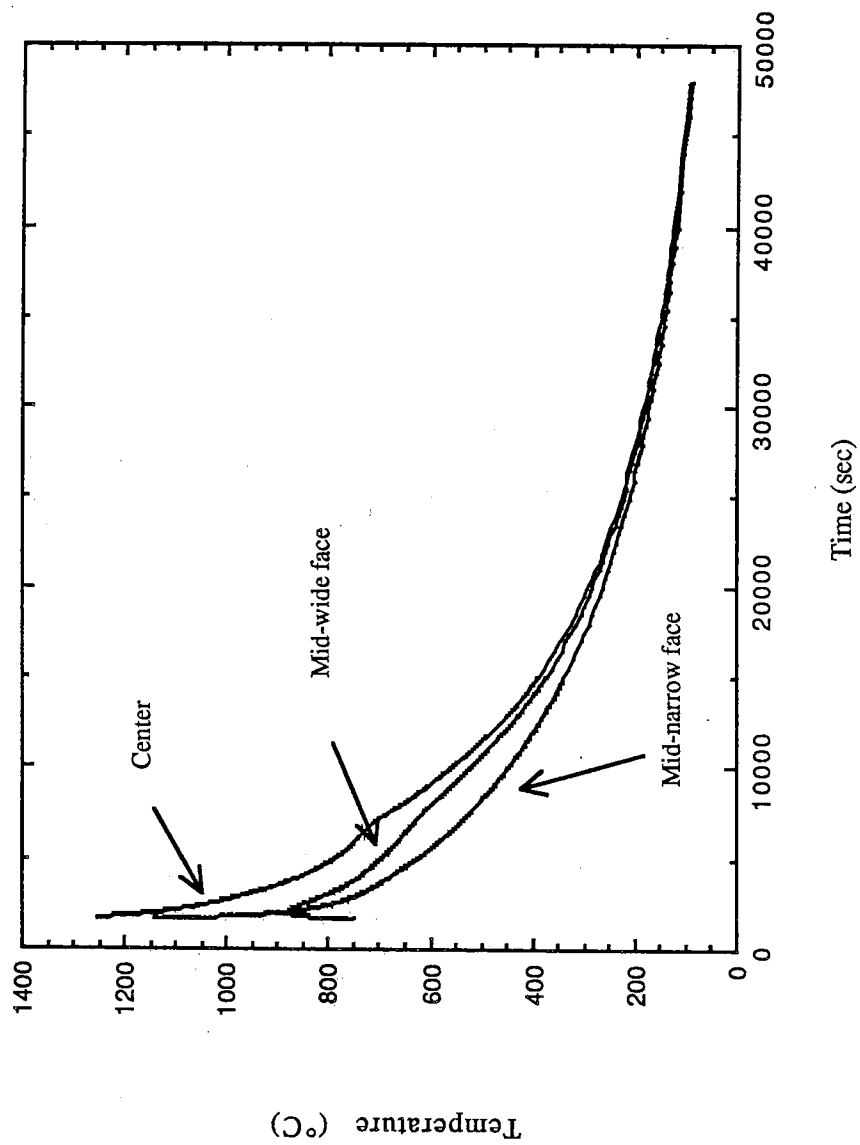


Figure 36. Temperature histories of the center, mid-wide face, and mid-narrow face in the transfer region.

Reheating of the wide face is evident after caster exit, with a temperature recovery of almost 130°C after only 4 minutes. Although the narrow face was too hot at the exit of the caster, the mid-narrow face temperature drops below the mid-wide face temperature after only 6 minutes of transfer. Thus, the artificial insulation of the narrow face should have a minimal effect on the stress state later in the transfer region. This result also demonstrates the need for special narrow face heating, to prevent its natural tendency to cool excessively.

Two times in the transfer region are examined in detail: 54.2 minutes and 13.3 hours after caster exit. The first time (54.2 min.) was selected because reheating is a maximum and the transformation from austenite(γ) to ferrite/pearlite (α) is prevalent. The fraction of α transformed is shown in Figure 37, and the corresponding temperature contours are shown in Figure 38. The contour values correspond to the transformation temperatures of $A_{c3} = 840^{\circ}\text{C}$, $A_{r3} = 780^{\circ}\text{C}$, $A_{c1} = 725^{\circ}\text{C}$, and $A_{r1} = 650^{\circ}\text{C}$. Figure 39 clearly shows the compressive band which coincides with the two-phase region. The model takes into account the sign of the effective stress by making it positive if the largest coordinate stress is tensile and negative for compressive. Tension caused by the volume expansion appears at the narrow face and a portion of the wide face near the corner. The center of the slab is also tensile, though not as high as the center of the narrow face. This pattern is clearly shown in Figures 40 and 41. Figure 40(a) and 40(b) show the stress and plastic strain, respectively, along the centerline of the wide face. The surface is in compression, while the core of the slab is tensile. The corresponding stress and plastic strain plots for the centerline of the narrow face are shown in Figure 41(a) and Figure 41(b), respectively. The compressive band is clearly

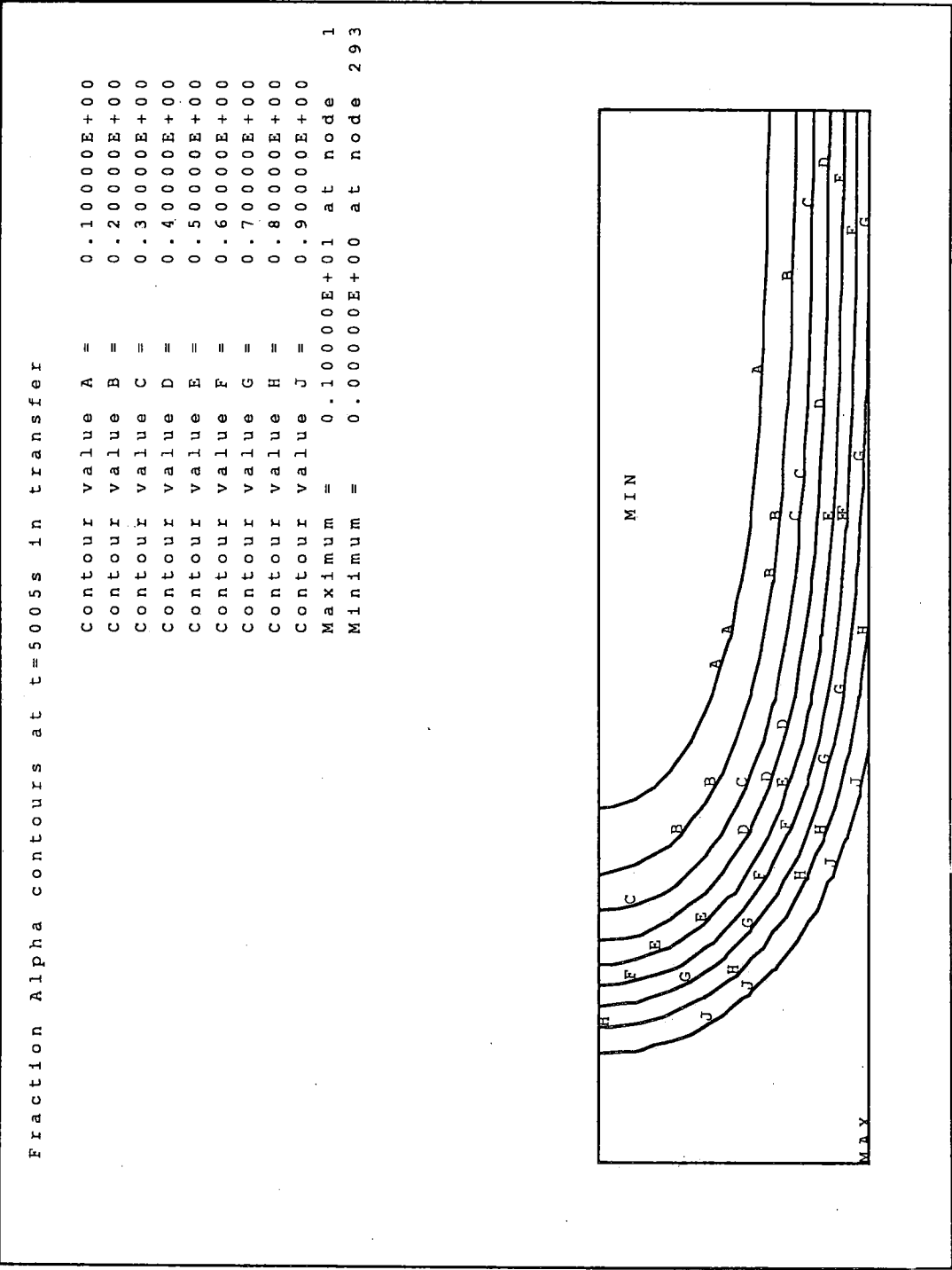


Figure 37. Contours of fraction (α) ferrite/pearlite transformed at 54.2 minutes in transfer.

Temperature contours in transfer at t=5005s

Contour value A = 0.84000E+03
 Contour value B = 0.78000E+03
 Contour value C = 0.72500E+03
 Contour value D = 0.65000E+03
 Maximum = 0.79064E+03 at node 392
 Minimum = 0.57434E+03 at node 1

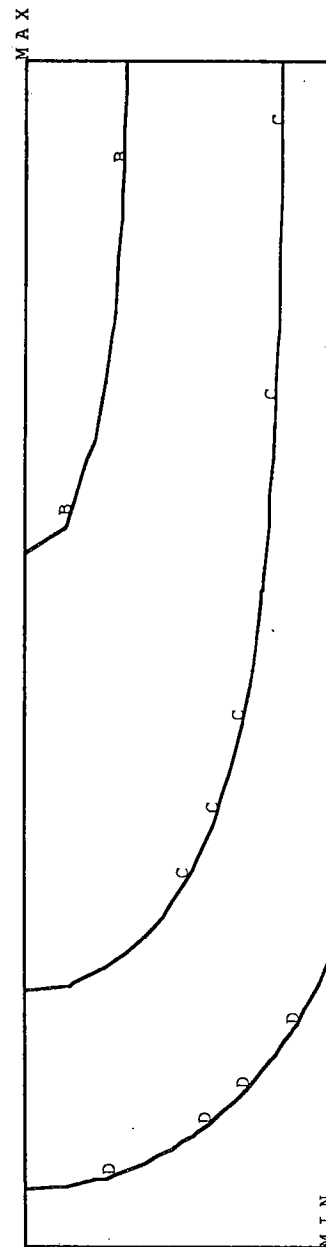


Figure 38. Temperature contours at 54.2 minutes in transfer.

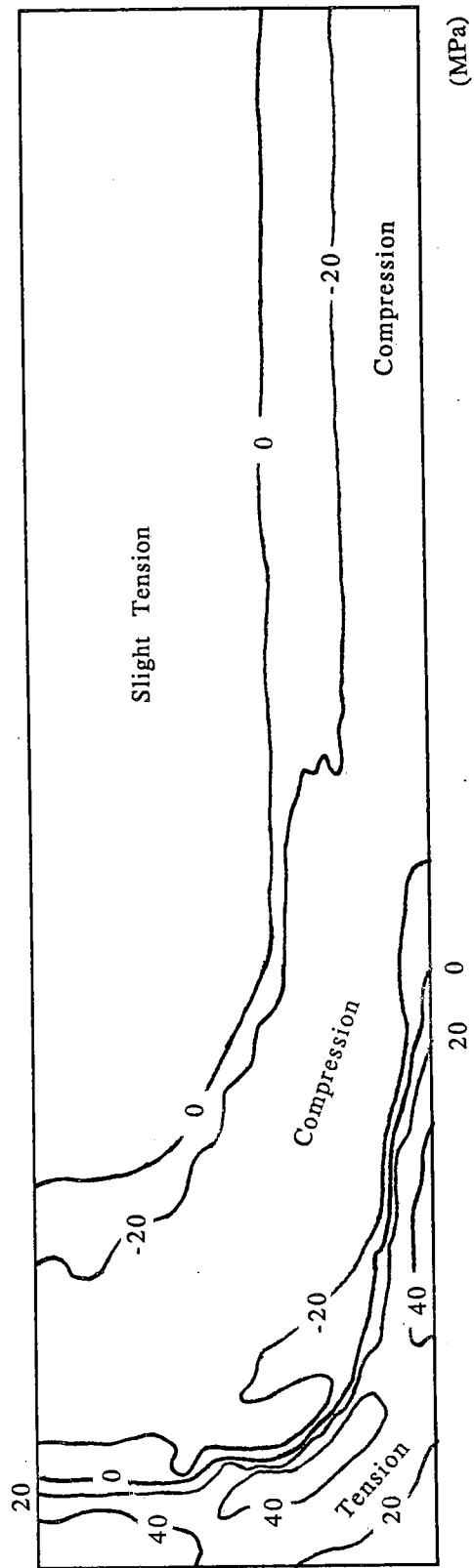
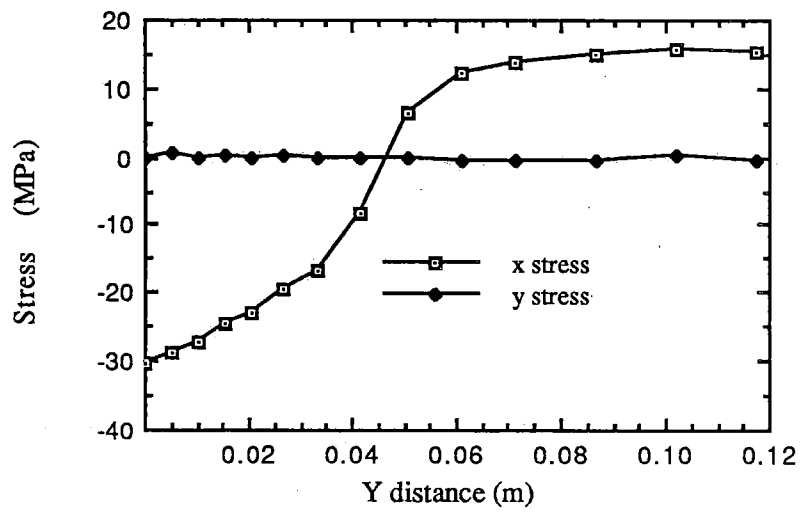
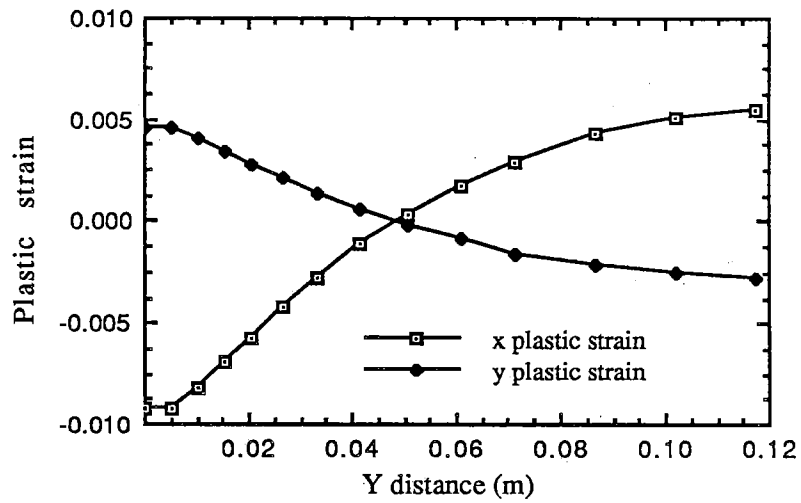


Figure 39. Effective Stress contours at 54.2 minutes in transfer.

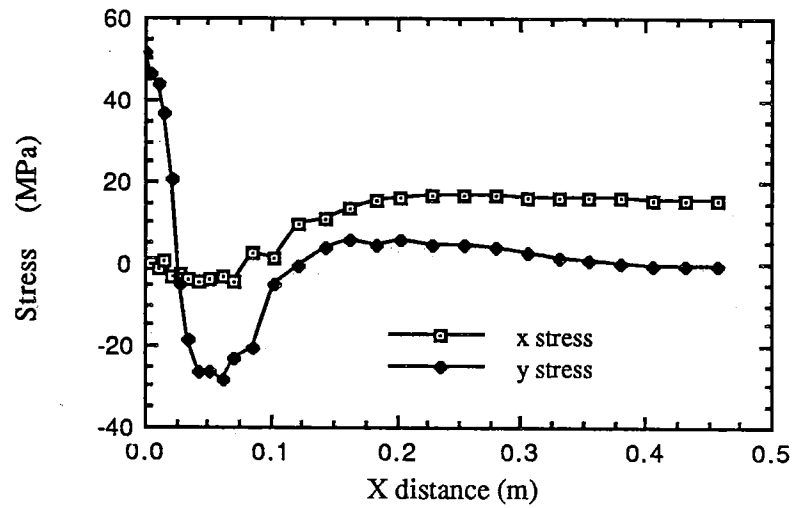


(a)

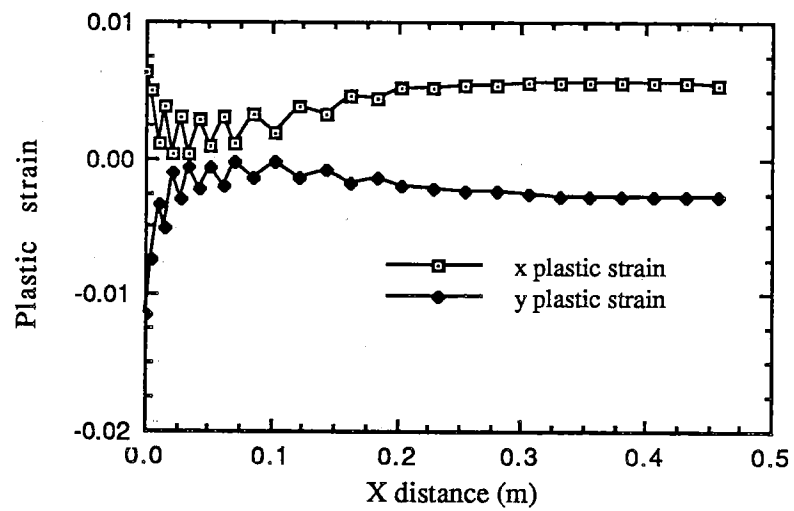


(b)

Figure 40. Stress (a) and plastic strain (b) along the centerline of the wide face at 54.2 minutes after caster exit.



(a)



(b)

Figure 41. Stress (a) and plastic strain (b) along the centerline of the narrow face at 54.2 minutes after caster exit.

shown, while the tension on the surface is quite high. If the steel ductility were poor, this would predict a high susceptibility of the narrow face to longitudinal cracking, a problem not reflected in the literature. The lack of such an occurrence indicates the excellent ductility of steel which has completely transformed to α .

The second time (13.3 hrs.) shows the residual stress state of the steel slab after it has cooled almost to ambient temperature. Figure 42 shows the residual effective stress contours. The surface is completely compressive, with a tensile core. The stress and plastic strain along the centerline of the wide face is shown in Figure 43(a) and 43(b), respectively. The same data for the narrow face centerline is shown in Figure 44(a) and 44(b). These figures indicate that at least a 4cm thick layer of compression protects the surface from cracking. Thus, reheating from a completely cold slab is less likely to form cracks.

The stress pattern along the wide face centerline compares favorably with trends found for stresses generated during a simulation of solidification of a circular cylinder [44]. The interiors of both castings are in tension and the outside is in compression, and the magnitude increases with decreasing temperatures when the calculation is elastic. Both curves have a rounded "s" shape caused by plastic creep which occurred earlier, when the casting was hotter.

Negligible plastic strain is generated at the low temperatures toward the end of reheat and elastic behavior is prominent at the 40-80 MPa stress levels encountered. This is expected since these stresses are far below the yield stress of plain carbon steel of approximately 200 MPa. The effective plastic

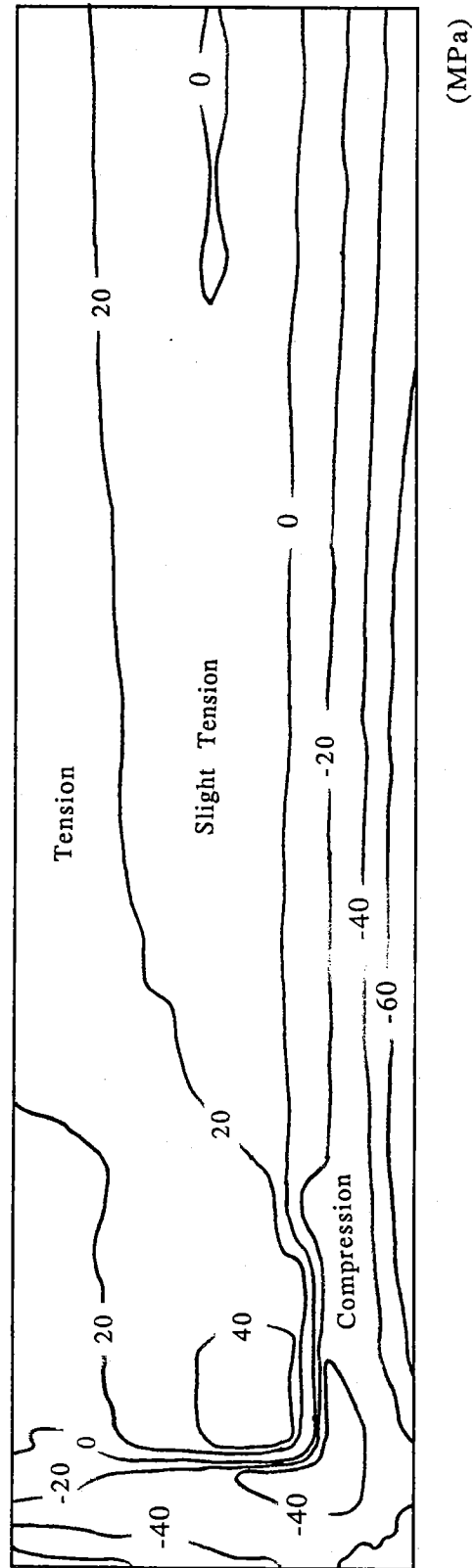
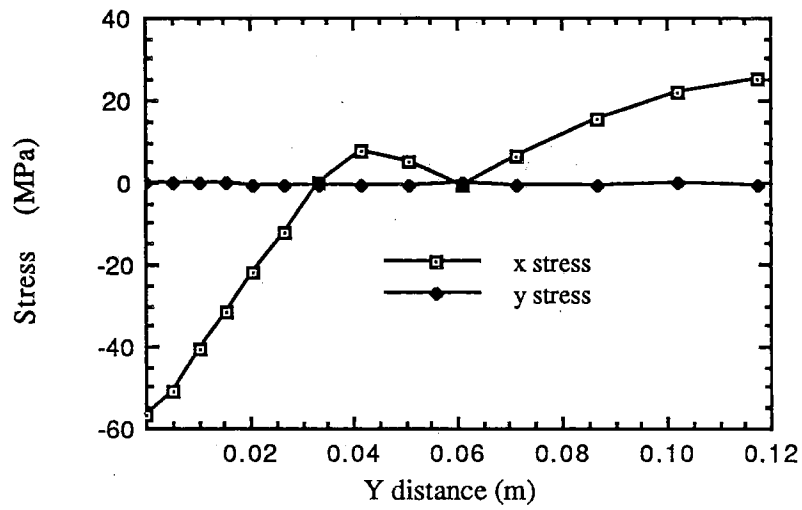
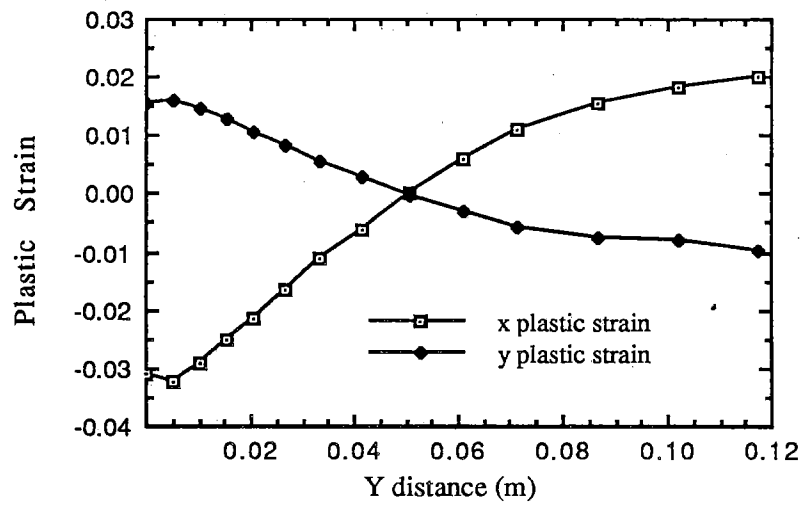


Figure 42. Residual effective Stress contours at 13.3 hours after caster exit.

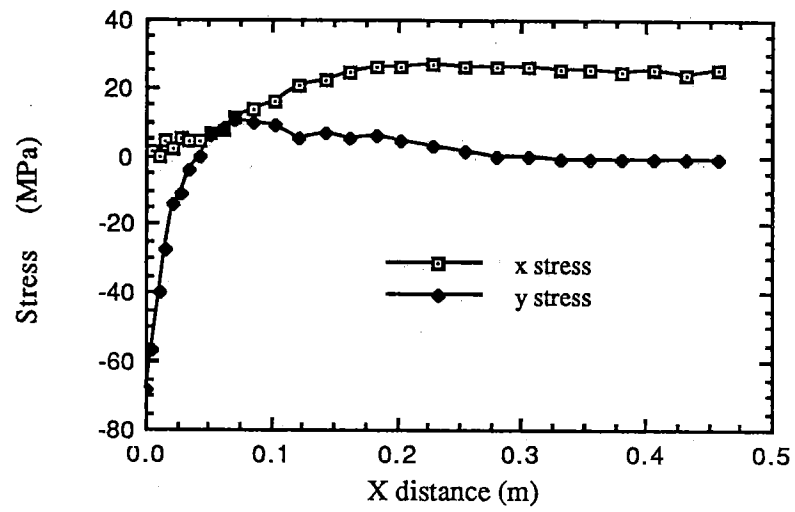


(a)

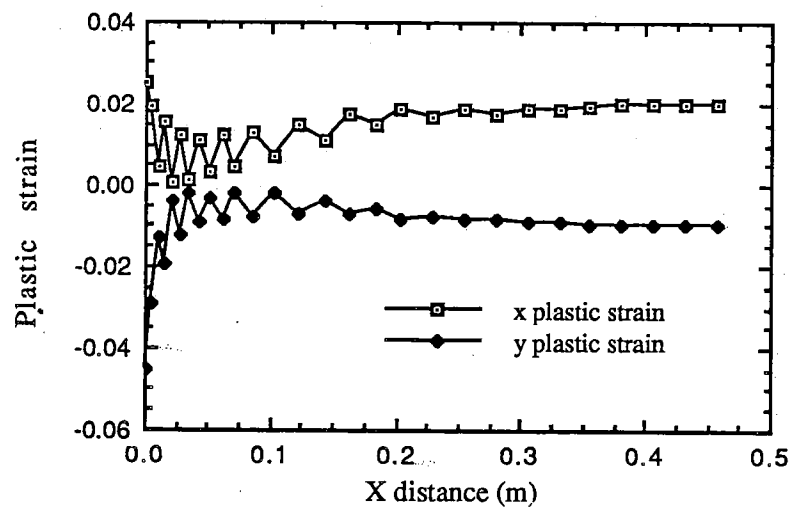


(b)

Figure 43. Stress (a) and plastic strain (b) along the centerline of the wide face at 13.3 hours after caster exit.



(a)



(b)

Figure 44. Stress (a) and plastic strain (b) along the centerline of the narrow face at 13.3 hours after caster exit.

strain remains constant at roughly 2% from two hours after caster exit until the end of transfer.

5.4 REHEAT

A reheat simulation was started at 10 minutes after exit from the caster. This represents a "hot" simulation out of the caster at the minimum transfer logistically feasible. Narrow face heating only is required to extend transfer time since the internal heat in the slab is sufficient to keep the surface above the exit temperature from the caster for at least 35 minutes. With insulated transfer cars and hoods, the track time could be extended even longer while maintaining the same thermal state.

The slab was reheated until the temperature range in the slab was within 20°C of the furnace temperature of 1200°C. The temperature histories for the center, mid-narrow face, and the mid-wide face are shown in Figure 45.

To understand the heat flow into the slab during reheat, temperature contours have been plotted at various times in the reheat process. These appear in Figures 46-52. The heat flow into the slab by radiation and continued cooling of the center causes a small cooler region near the corner to be trapped within hotter, expanding steel. This trapped region grows and gradually reaches the centerline of the narrow face before smoothing out. These results show excellent agreement with similar work involving static-cast ingots [32].

Stress and plastic strain along the centerline of the wide face at the start of reheat are shown in Figure 53(a) and 53(b), respectively. The

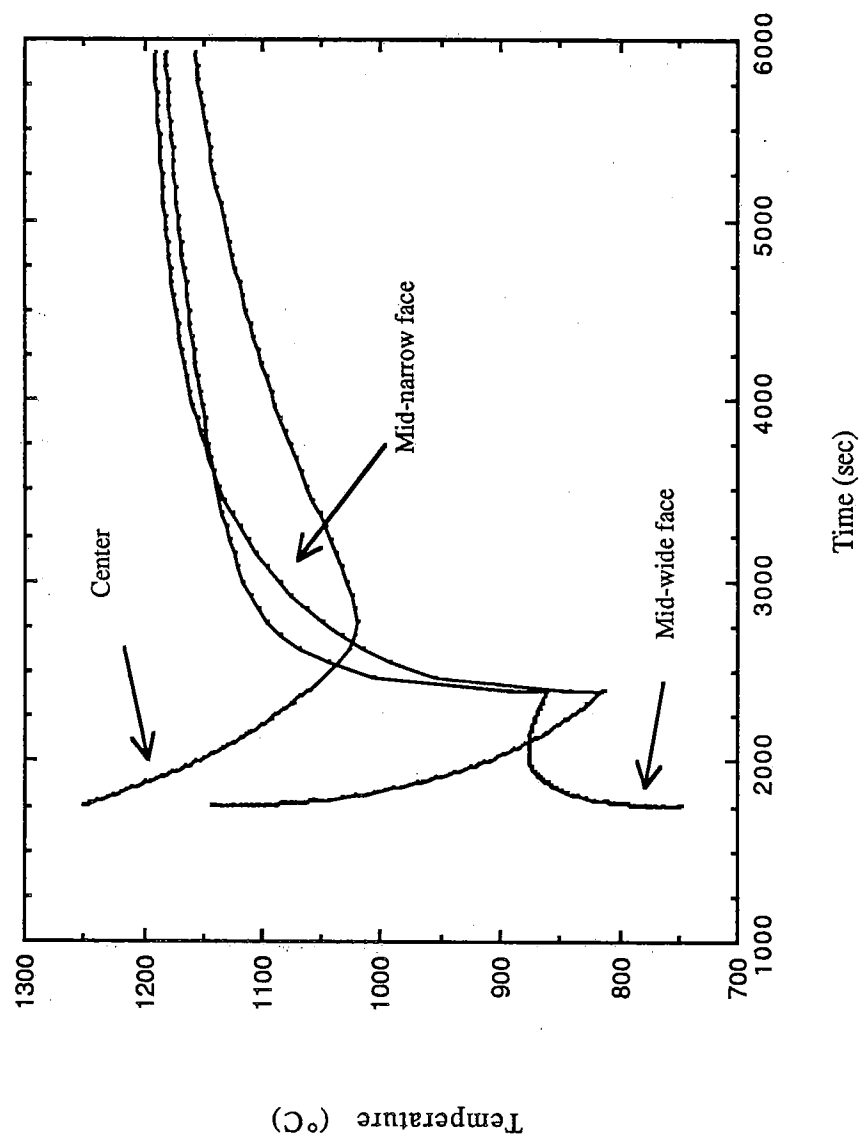
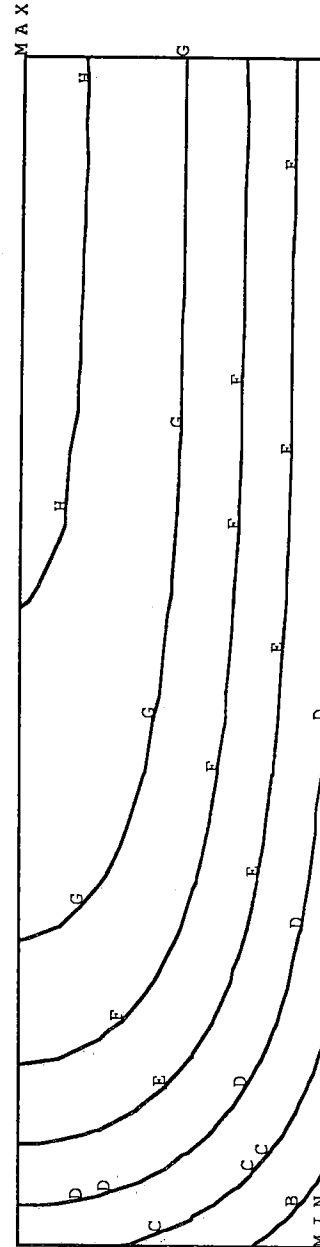


Figure 45. Temperature histories for center, mid-narrow face, and mid-wide face in the transfer/reheat region.

Temperature contours at t=2403s at the beginning of reheat

Contour value A = 0.70000E+03
 Contour value B = 0.75000E+03
 Contour value C = 0.80000E+03
 Contour value D = 0.85000E+03
 Contour value E = 0.90000E+03
 Contour value F = 0.95000E+03
 Contour value G = 0.10000E+04
 Contour value H = 0.10500E+04
 Contour value J = 0.11000E+04
 Maximum = 0.10610E+04 at node 392
 Minimum = 0.70830E+03 at node 1

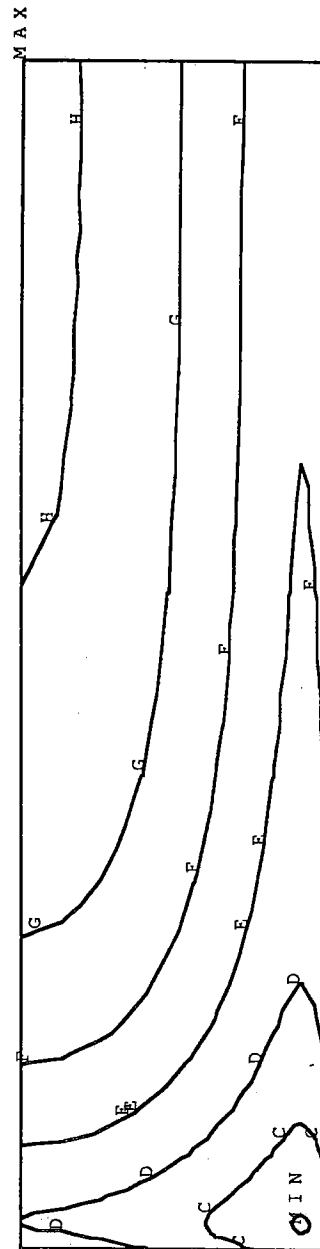


ridge2s cat contdata

Figure 46. Temperature contours at start of reheat.

Temperature contours at t=2413s in rehear

Contour value A =	0.70000E+03
Contour value B =	0.75000E+03
Contour value C =	0.80000E+03
Contour value D =	0.85000E+03
Contour value E =	0.90000E+03
Contour value F =	0.95000E+03
Contour value G =	0.10000E+04
Contour value H =	0.10500E+04
Contour value J =	0.11000E+04
Maximum =	0.10592E+04 at node 392
Minimum =	0.74519E+03 at node 31



ridge2s.csh contdata

Figure 47. Temperature contours after 10 seconds of rehear.

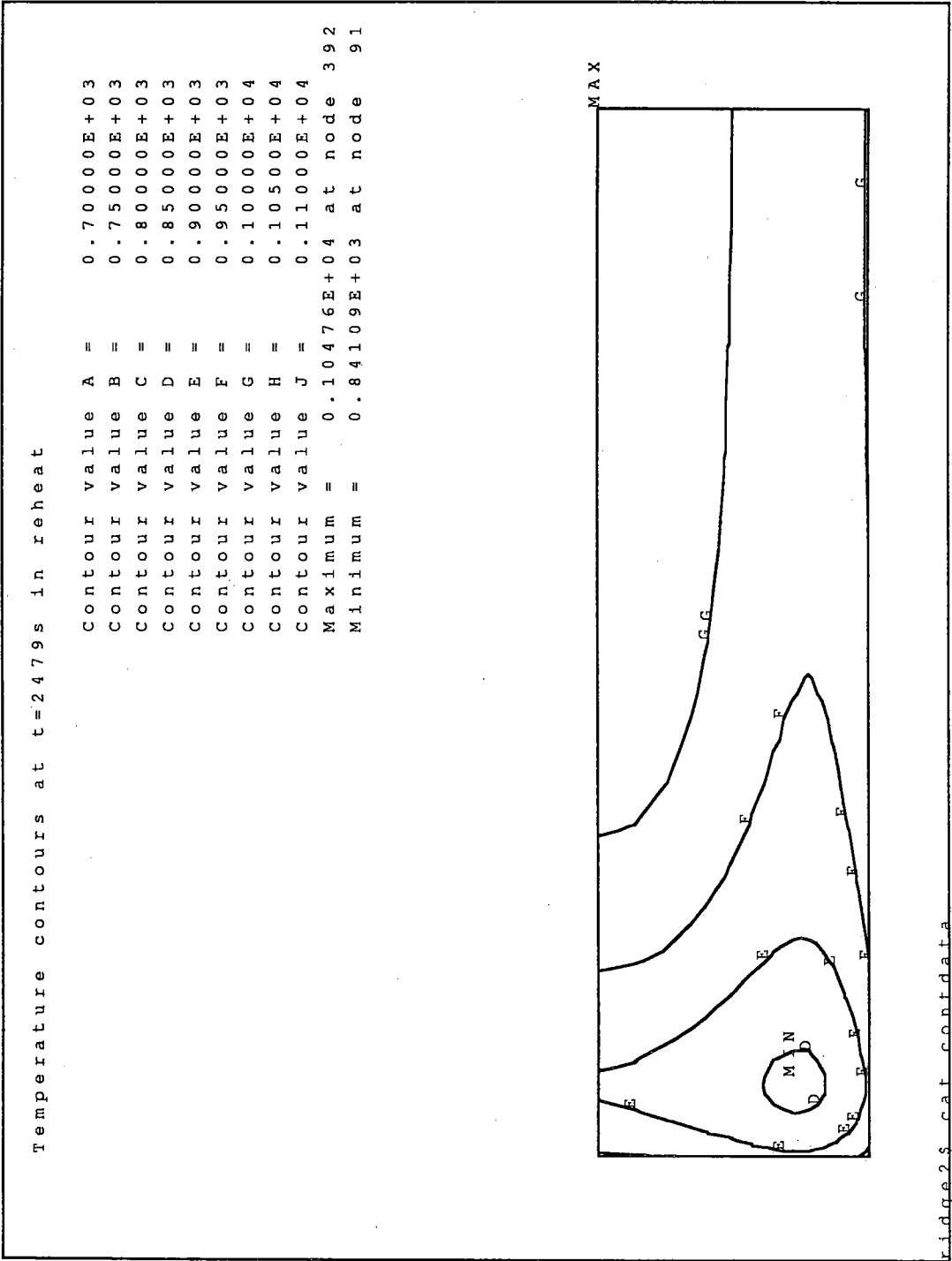


Figure 48. Temperature contours after 75 seconds of rehear.

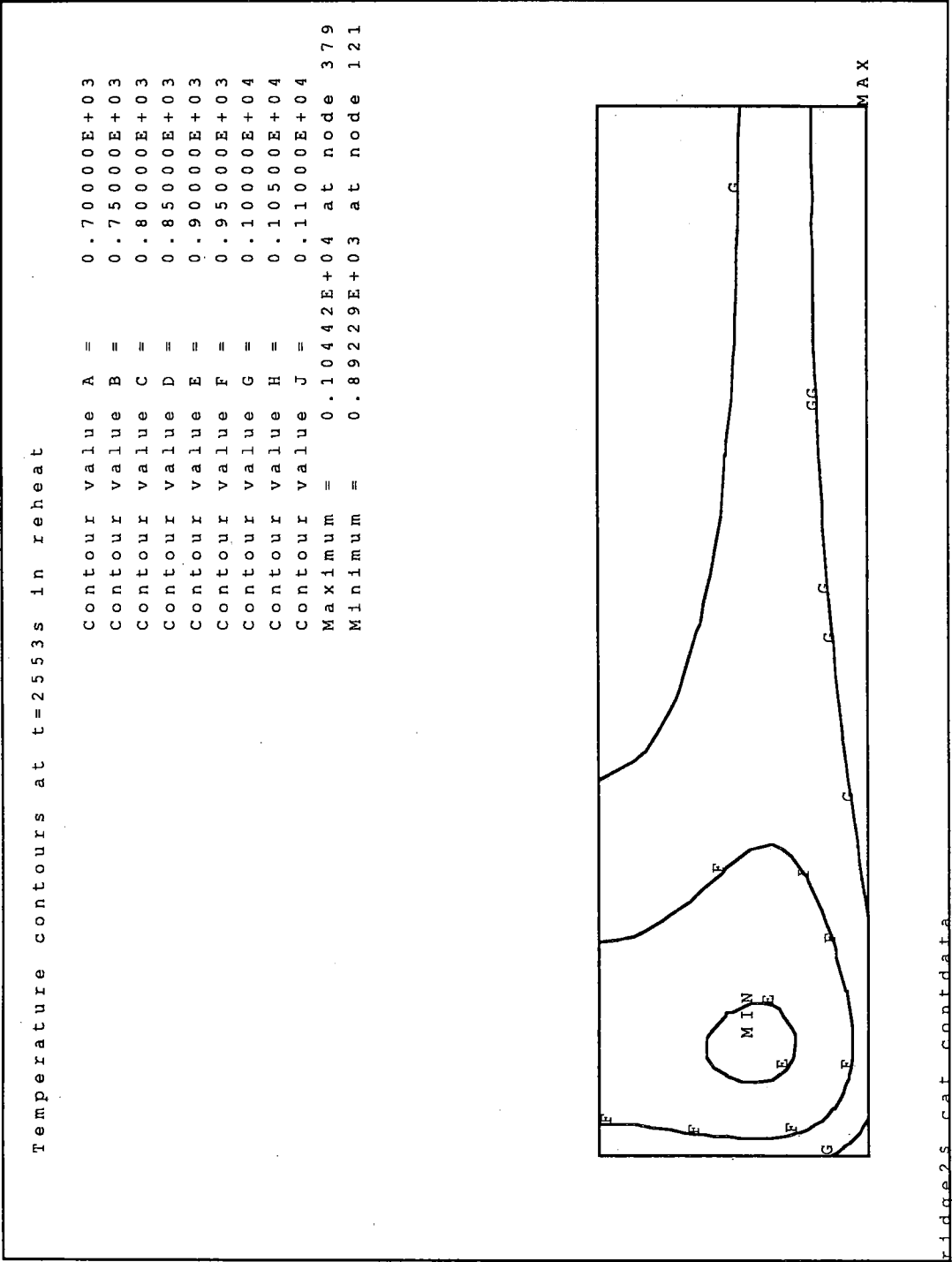


Figure 49. Temperature contours after 150 seconds of rehear.

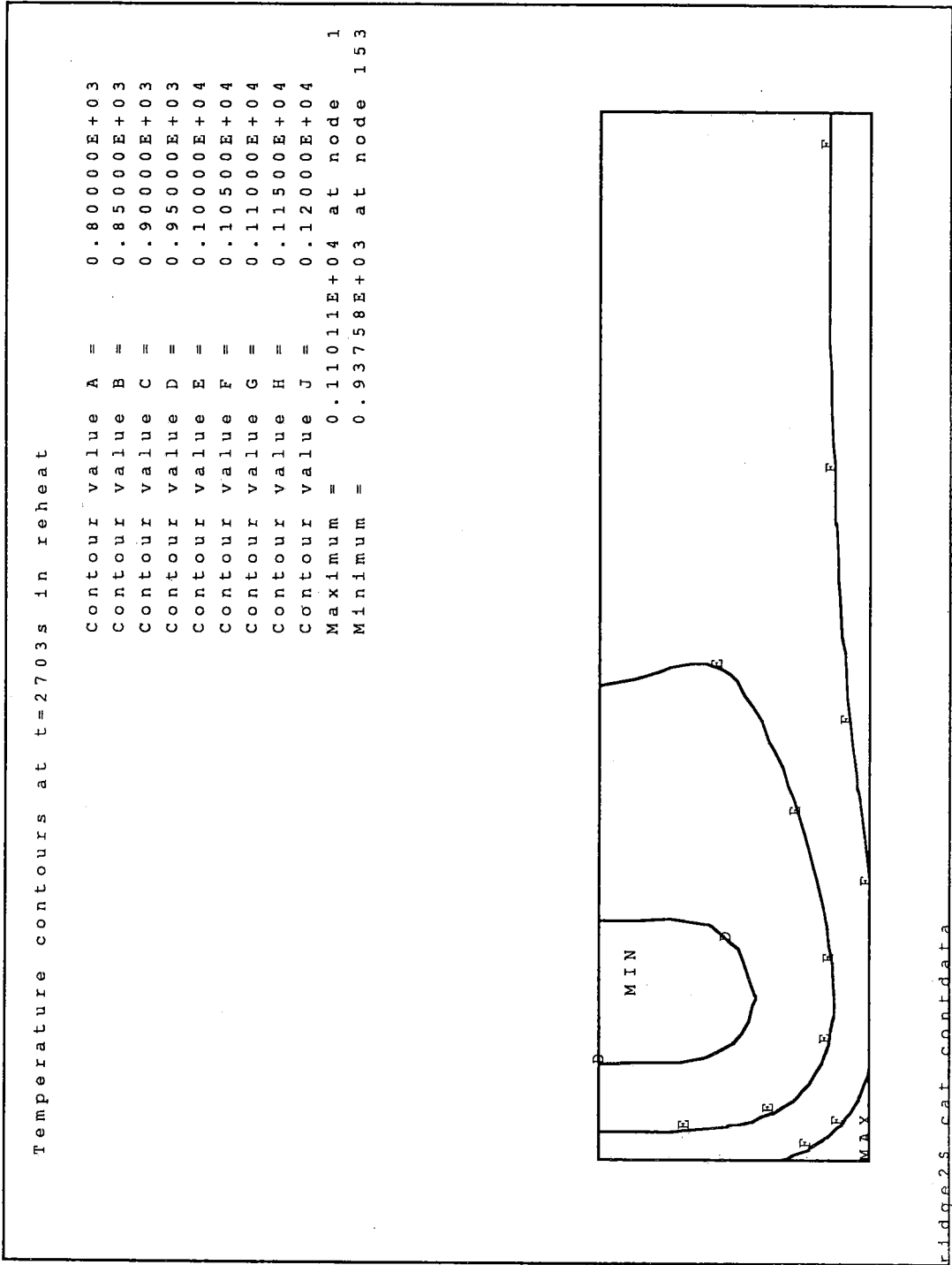


Figure 50. Temperature contours after 300 seconds of reheat.

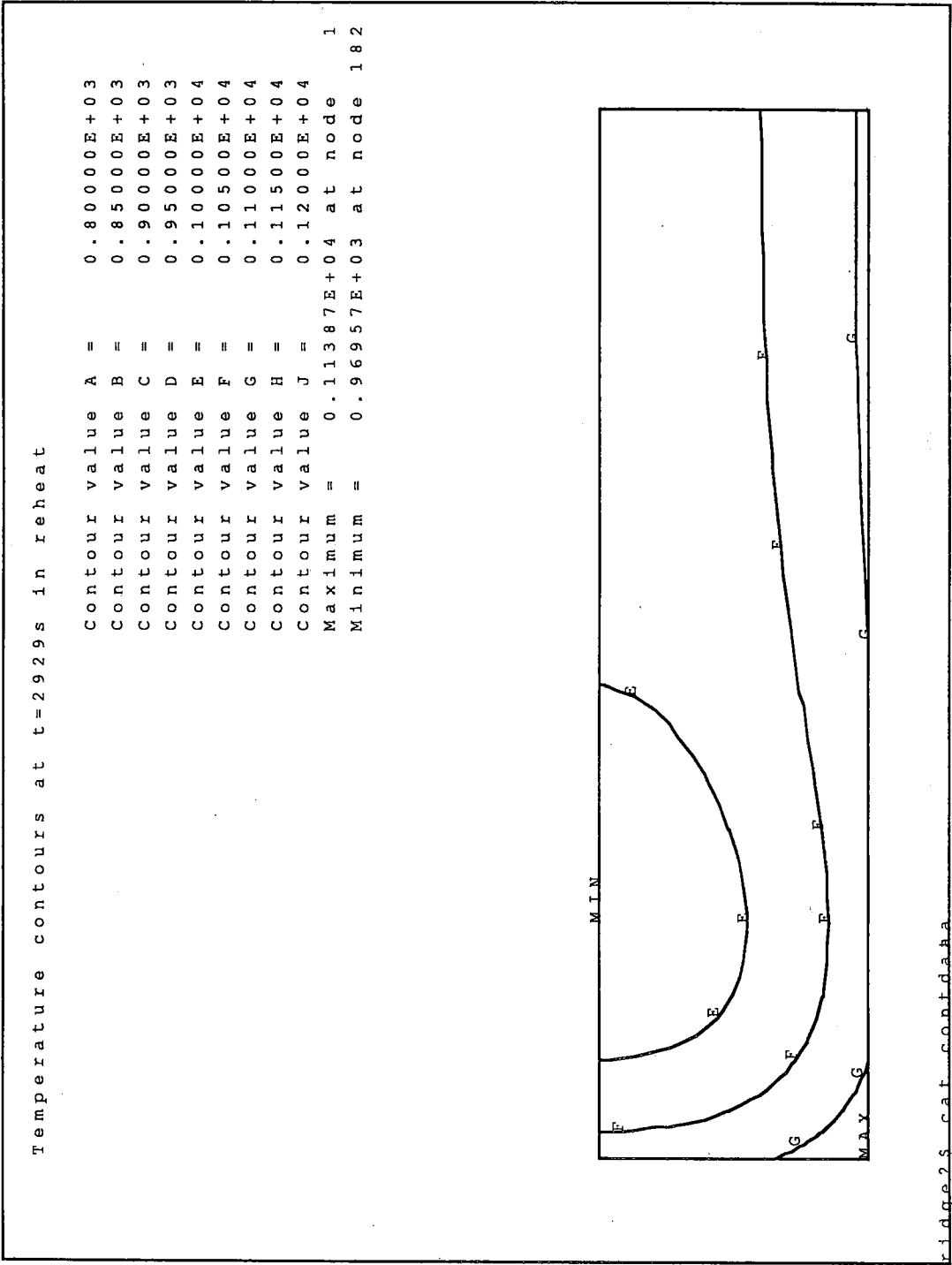


Figure 51. Temperature contours after 525 seconds of reheat.

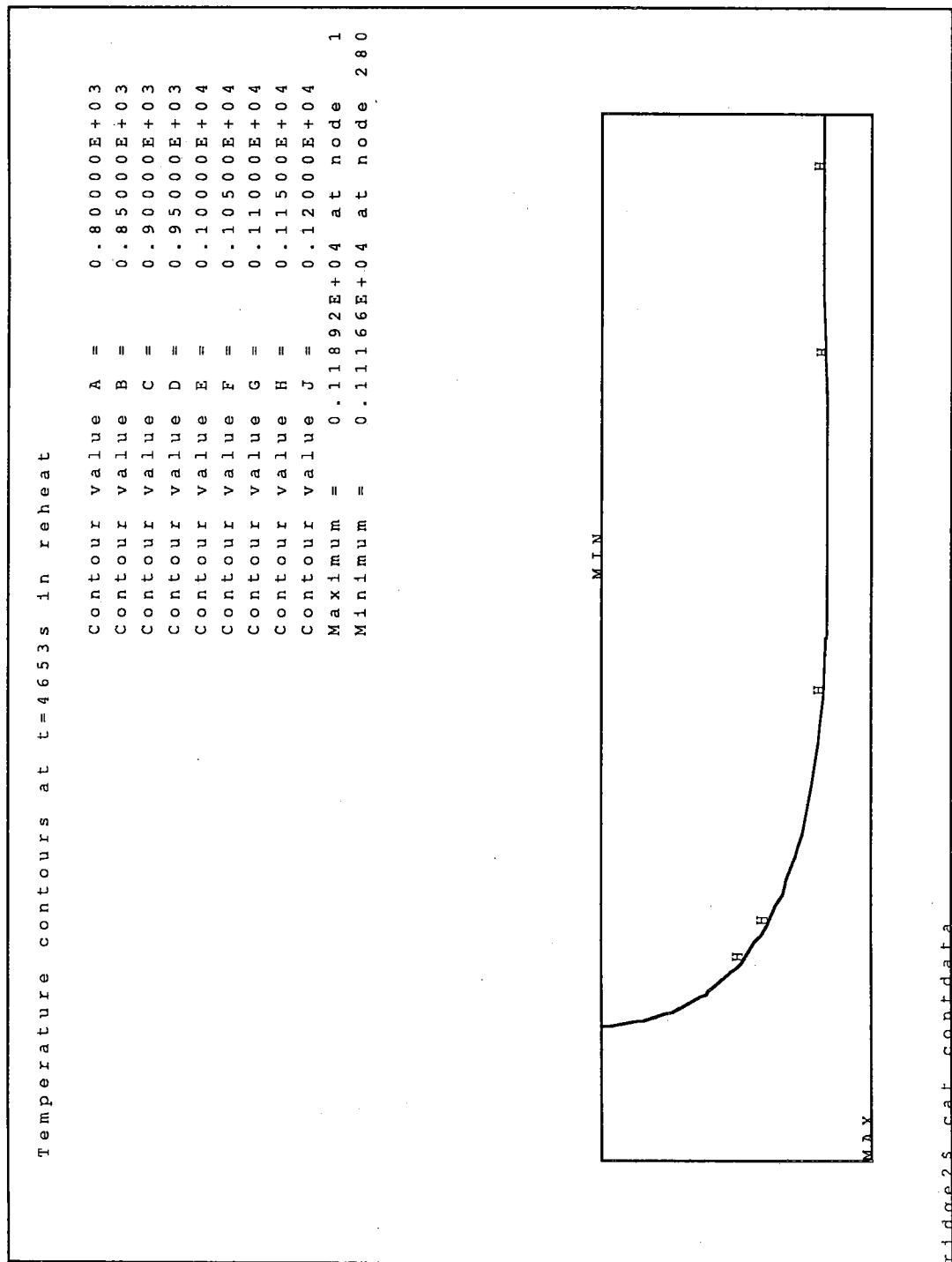
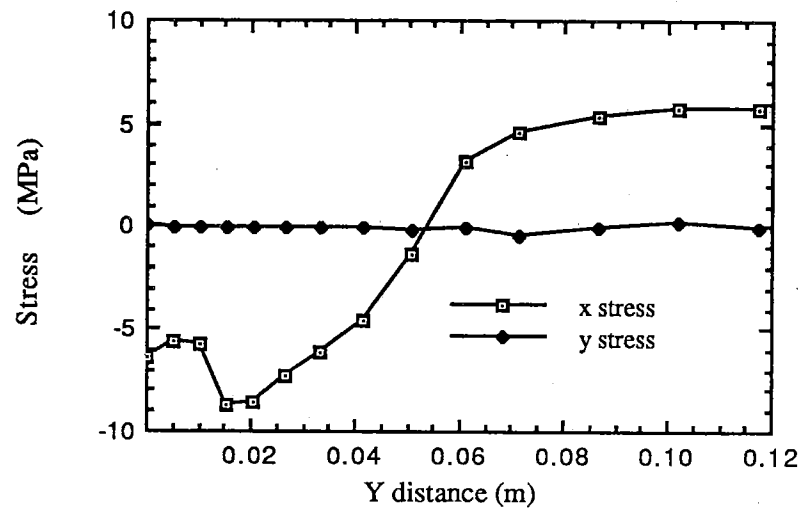
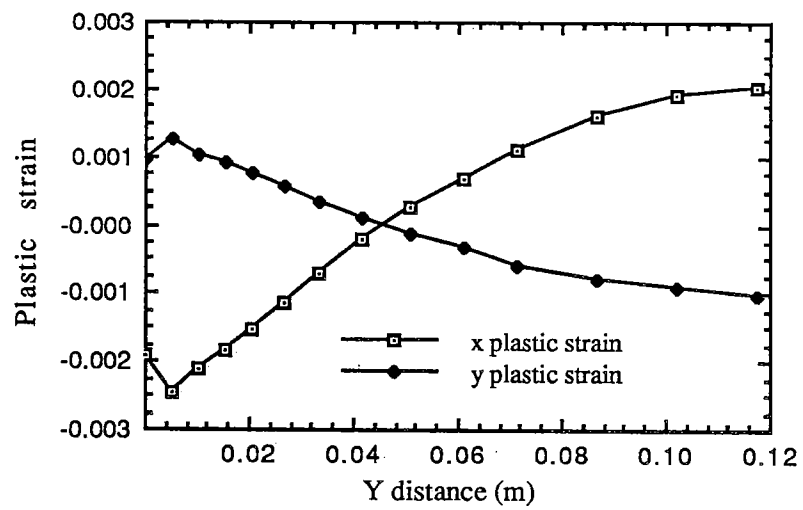


Figure 52. Temperature contours after 37.5 minutes of reheat.

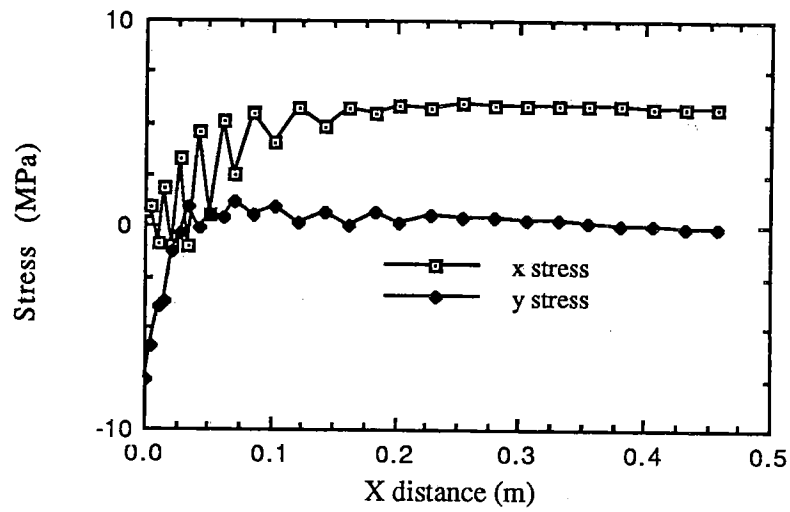


(a)

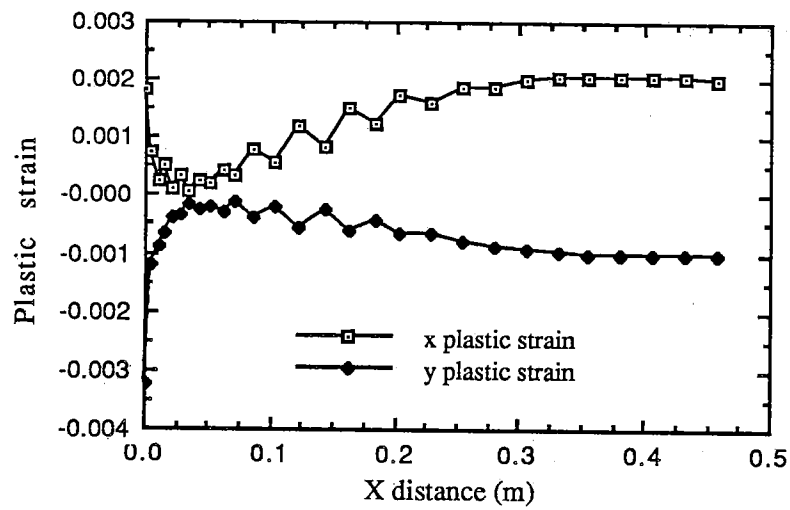


(b)

Figure 53. Stress (a) and plastic strain (b) along the centerline of the wide face at the start of reheat.



(a)



(b)

Figure 54. Stress (a) and plastic strain (b) along the centerline of the narrow face at the start of reheat.

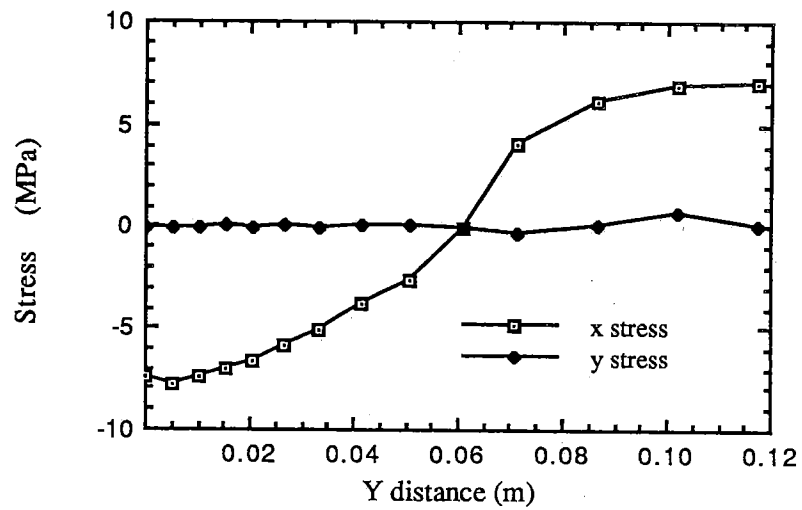
corresponding plots for the narrow face centerline appear in Figure 54(a) and 54(b). The stress is mildly compressive on the surface, and tensile in the interior. The plastic strain is more pronounced on the narrow face.

The stress and plastic strain along the centerline of the wide face after 300 seconds of reheating is shown in Figure 55(a) and 55(b), respectively. The corresponding plots for the narrow face centerline appear in Figure 56(a) and 56(b). The compressive band has widened and extends deeper into the slab, while the tensile interior stress increases, as shown in Figure 57. The plastic strain along both centerlines has increased considerably, however the distribution of the plastic strain is unchanged.

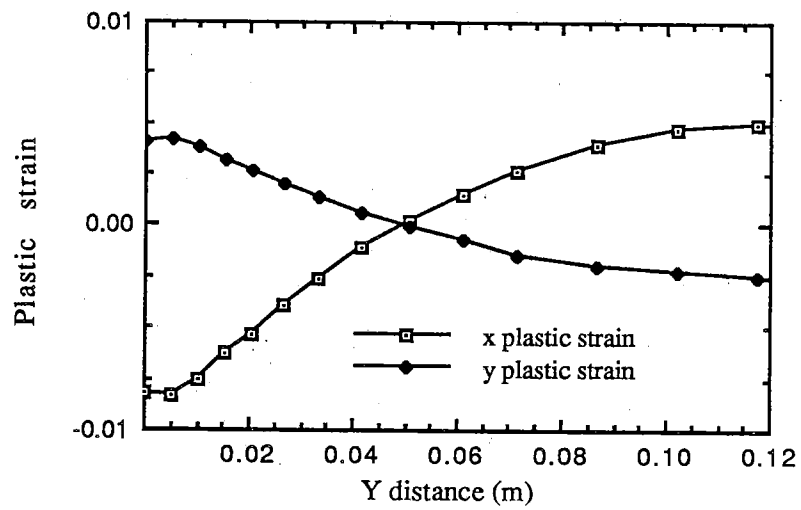
Finally, the stress and plastic strain along the wide face and narrow face centerlines at 2000 seconds is shown in Figures 58(a), 58(b), 59(a), and 59(b), respectively. Also, Figure 60 shows the effective stress contours for this time. The stress has dissipated somewhat, and the plastic strain has also reduced to a point quite similar to the start of reheat. Further heating of the slab and holding the slab at these high temperatures will allow these stresses to relax even more.

5.5 DISCUSSION

Any crack formed in the steel strand will not propagate unless it is put under tension. If a crack forms and then experiences compressive stress, then the crack may close, unless it has reached the surface and been exposed to the environment. It follows, then, that tension should be avoided where possible, and is permissible only at times when the steel is highly ductility and not susceptible to cracks.

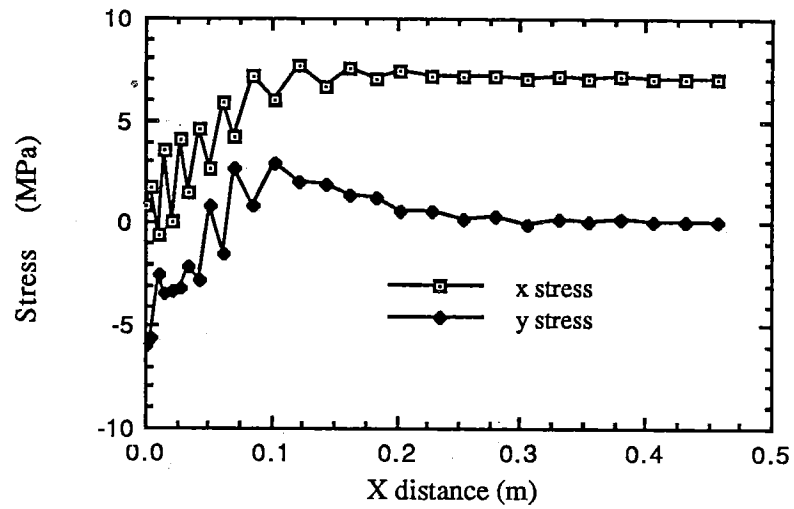


(a)

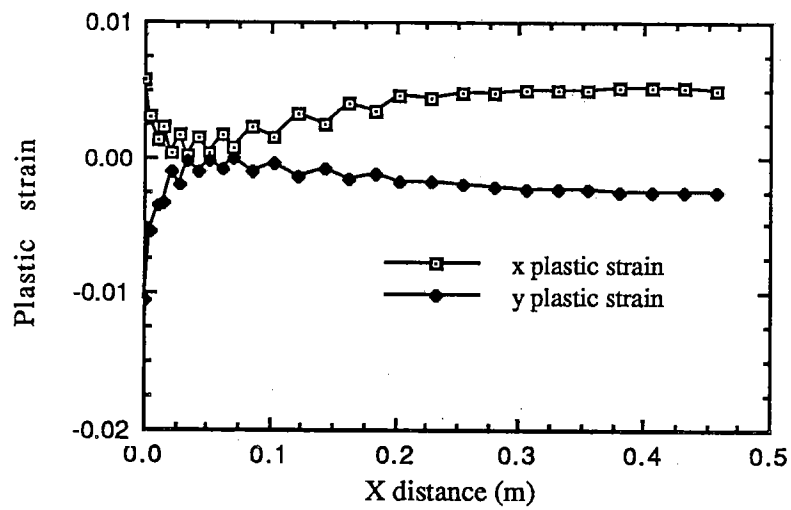


(b)

Figure 55. Stress (a) and plastic strain (b) along the centerline of the wide face at 300 seconds from the start of reheat.



(a)



(b)

Figure 56. Stress (a) and plastic strain (b) along the centerline of the narrow face at 300 seconds from the start of reheat.

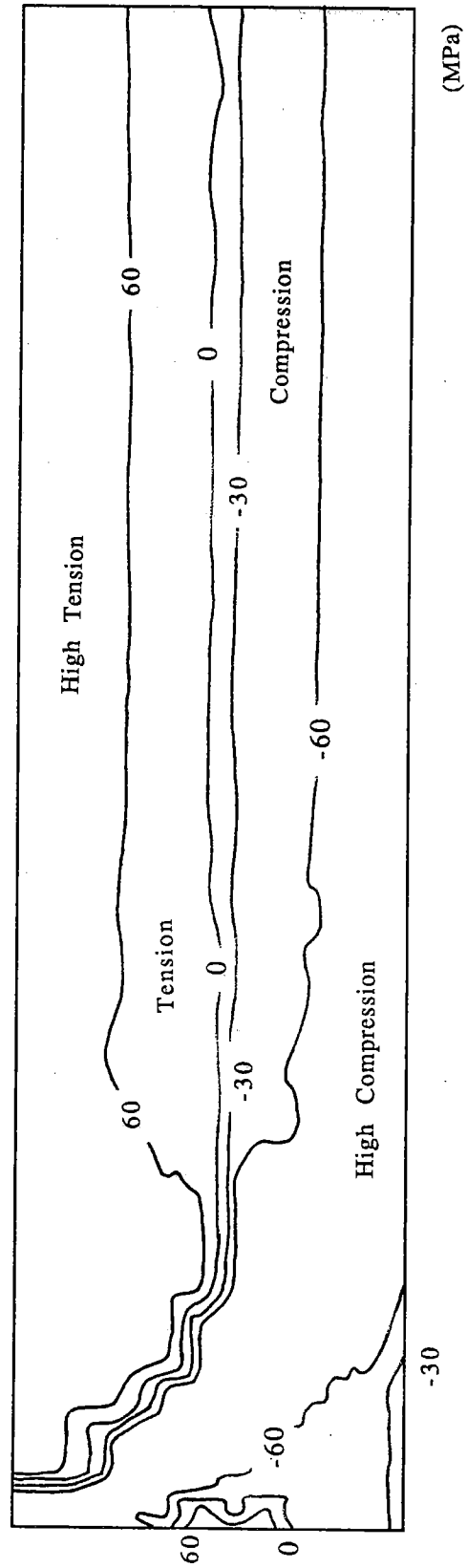
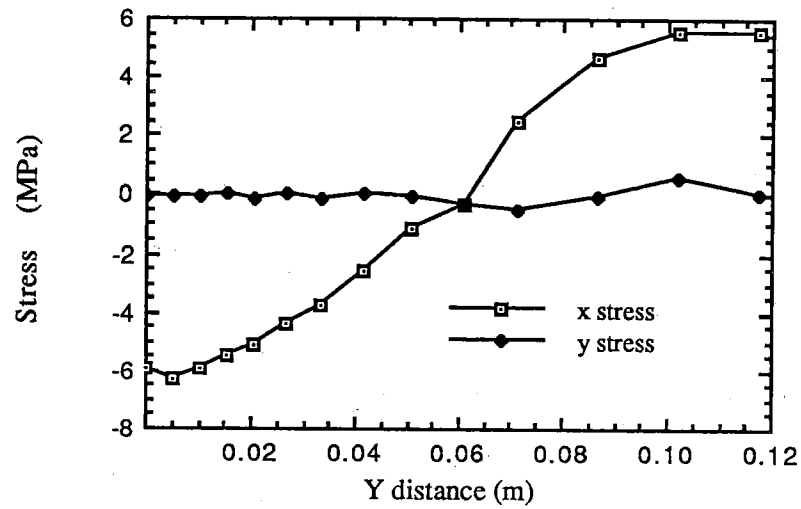
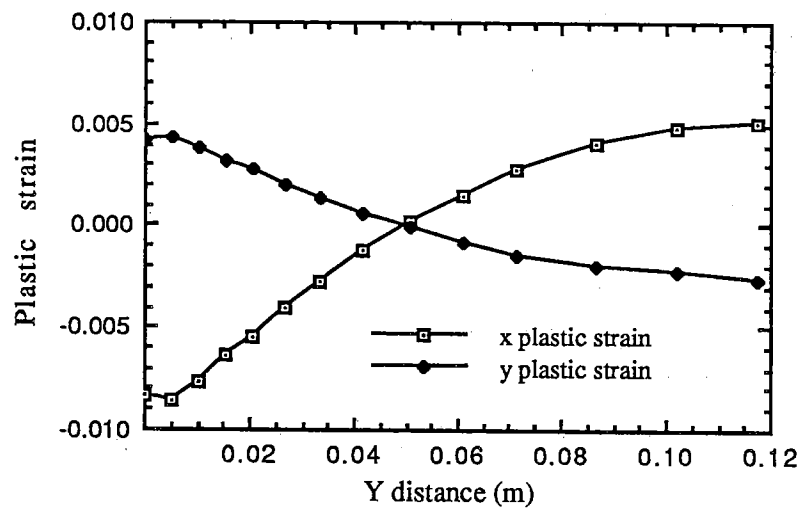


Figure 57. Effective Stress contours at 300 seconds from start of reheat.

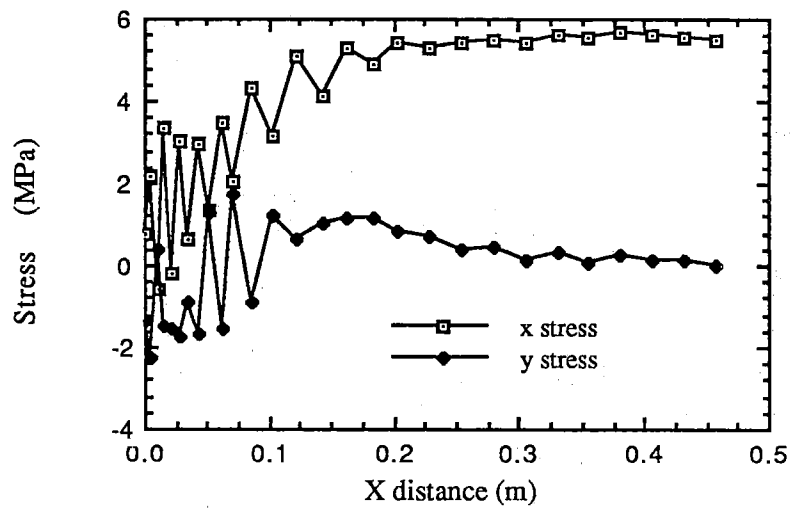


(a)

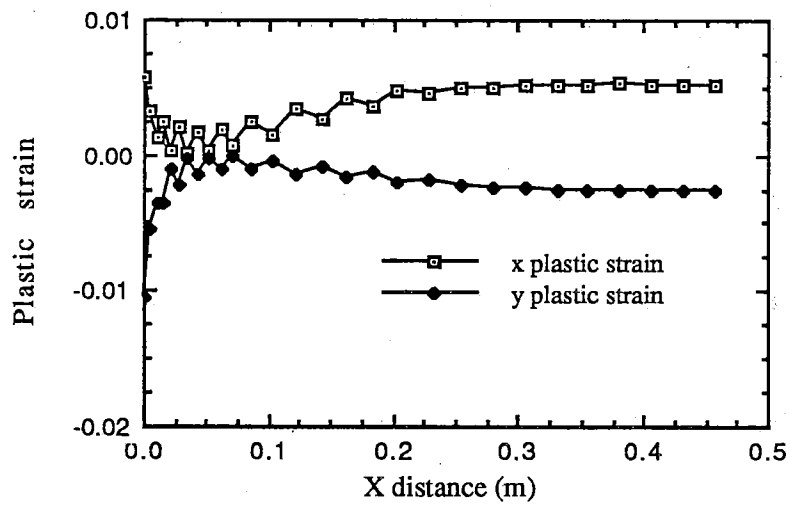


(b)

Figure 58. Stress (a) and plastic strain (b) along the centerline of the wide face at 2000 seconds from the start of reheat.



(a)



(b)

Figure 59. Stress (a) and plastic strain (b) along the centerline of the narrow face at 2000 seconds from the start of reheat.

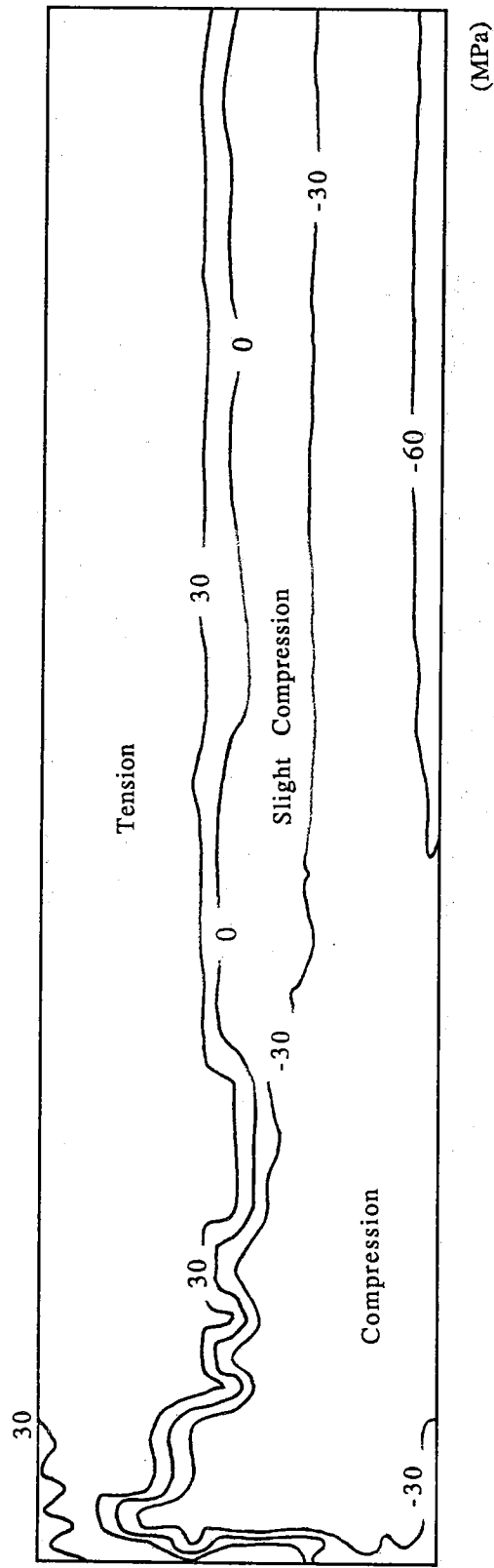


Figure 60. Effective Stress contours at 2000 seconds from start of reheat.

The rebound of surface temperature at caster exit is caused by the sensible heat stored in the much hotter interior of the slab. This reheating is very beneficial to the slab since the expanding surface "layer" is forced into compression. The center of the wide face shows a band of surface compression that extends 5cm into the strand. In fact, the simulation shows the wide face surface to be in compression almost all of the transfer time.

When reheating from an intermediate stage of transfer, the combination of loss of ductility and tensile stress caused by the heat flow reversal may increase the likelihood of cracking. The inverse relationship of track time versus susceptibility to cracking is well documented, and this may be attributed to the avoidance of reheating when the strand is undergoing a phase transformation. The volume change during the phase change from austenite to α can cause tension in the surrounding regions, possibly resulting in cracks or other defects if the steel in tension is also within the critical 700°C - 900°C ductility trough. Since some periods of surface tensile stresses are unavoidable if the temperature falls below the A_{r3} temperature, the stress model results imply that the slab should be prevented from becoming this cold.

The actual times for processing of the slab between the caster and the furnace are highly dependent on the set-up of the individual steel mill. If the reheat furnace is close to the caster, then only edge heaters may be needed to keep the slab from dropping below 900°C. Edge heating is always required to prevent the narrow face from cooling into the two phase zone, since even the model run that maximized the narrow face temperature leaving the caster found the narrow face to fall below 800°C within 12 minutes with no special reheating present.

As mentioned earlier, 35 minutes appears is available for transfer without losing surface temperature or using hoods for the casting conditions simulated. However, this short transfer time is logistically difficult unless some provision is made for continual transfer of slabs to the reheat furnace. Current slab transfer practice involves stacking the slabs on rail cars until enough have accumulated to warrant shipping to the furnace. With hotter temperatures at the caster exit, the safe uninsulated transfer time could be extended, using only narrow face heating. With hoods and insulated transfer cars, the safe transfer time may be lengthened to allow transfer to reasonably distant rolling mills.

The worst thermal processing sequence indicated from the current work would be to charge the slab after approximately one hour of open air transfer. Heating of the surface would cause the surface to expand. Depending on the size of the internal compressive band formed by the phase change, the tensile stress on the surface in combination with the ductility loss would likely initiate surface or subsurface cracking. Thus, this situation should be avoided through the control of heat loss and proper timing for hot charging.

6. CONCLUSIONS AND RECOMMENDATIONS

Finite element model simulations were performed to examine thermally-induced stress and strain during the continuous casting and hot charging of steel slabs and interpreted to predict processing practices with a potential for defect formation. Based on the model results and previous literature, several conclusions can be drawn:

- The mold region of the caster is very important to defect formation, since defects such as transverse cracks, longitudinal cracks, and star cracks are believed to start in the mold and develop later in the process. Clearly, the mold region is a highly critical area which requires a more detailed analysis than was achieved here.
- The spray zone of the caster is also a complex portion of the continuous casting process. Great temperature fluctuations (and thus surface stresses) are found which are highly dependent on the contact time of the roller on slab surface. Only qualitative elastic stress results could be obtained by the model in this region of the caster, due to the highly transient nature of these stresses. The addition of unbending and bulging to the caster analysis through a longitudinal slice model would be required before reasonable prediction of the true stress state at the exit of the caster could be made. However, the model used in this simulation was developed in such a way that any caster configuration can be modeled, and these future modifications could be incorporated.
- Results from the transfer / reheat portion of the current work show that stresses arising during these stages are generally quite low and are far less

than would be encountered during unbending. Thus, special precautions for hot charging need be taken only for the most crack prone steel grades containing nitride precipitates.

- For crack sensitive steel slabs, the model results show a need to avoid straining the slab while the phase transformation from austenite to ferrite/pearlite occurs, since both the highest stresses and lowest ductilities are found at this time. Reheating of the slab while the surface region is undergoing this transformation likely increases the susceptibility of the slab to cracking. Thermal sequences which avoid cooling the slab into the 700-900 °C temperature zone of embrittlement also show beneficial surface compression across the whole face and to a sufficient depth to prevent crack formation and/or propagation.

- The simulations predict substantial reheating of the slab after caster exit. This produces beneficial compressive stress at the surface and extends the "safe" transfer time by approximately 30 minutes even for uninsulated slab transfer.

- Reheating the slab quickly while the surface is completely above the transformation temperature maintains the surface in compression, thus preventing crack formation and also saving thermal energy. To produce hot slabs from the caster also requires high speed, low water flux casting practises which produce thinner and weaker shells, thereby demanding carefully aligned, closely spaced rollers.

- Alternatively, reheating a slab that has cooled completely below the transformation temperature again maintains the surface in compression, so should also be safe, although not as energy efficient. This finding

corresponds with industrial data which show decreased defect incidence as the hot charging temperature drops below the temperature range associated with ductility loss.

- To achieve these solutions also requires careful monitoring and knowledge of the temperature history of every slab. If a crack prone slab will be in the critical temperature range upon arrival at the reheat furnace, it should either be diverted from hot charging, or held until it cools out of that range. The presence of an insulated holding area would achieve this goal and also act as a buffer to allow some flexibility in processing and schedule matching.

- To efficiently implement hot charging, the caster must produce high temperature, defect free slabs. This involves higher casting speeds, softer cooling practices, and metallurgically clean steel from the tundish. Placement of the rolling mill in close proximity is ideal but this may only be feasible for new mills. Insulation of the narrow faces of the slab is required for almost any mill arrangement, since the model results found rapid cooling of the uninsulated narrow face to low temperatures even after the minimum possible narrow face cooling practice in the caster. For rolling mills located far away from the caster, more complete thermal insulation is required. The use of hoods, insulated transfer cars or even fueled heating lines may be required, depending on how hot the slab is at caster exit and how far the slab has to travel before hot charging.

- Although many aspects of the hot charging process are beyond the scope of the present work, it is clear that synchronization of the continuous caster with the hot rolling mill and indeed, with the whole plant, is also critical to the effective implementation of hot charging. If the defect-free, high

temperature slabs arrive at the reheat furnace, but are stored outside until the rolling mill is ready, then the advantages of hot charging are lost. Thus, the logistics of caster output, slab movement, and reheat furnace usage must be worked out such that bottlenecks or gaps in production do not occur. In addition, efficient methods of slab inspection, such as a quench tank for sample inspections, are needed to maintain slab quality without interrupting the casting process. Casting lines that are totally dedicated to hot charging may be needed, which requires increased efficiency in scheduling and in all aspects of the plant operation.

REFERENCES

- [1] American Iron and Steel Institute, Annual Statistical Report, AISI, Washington, DC, pp. 69, (1986).
- [2] S. Narita, M. Honda, K. Arima, K. Fujiki, W. Ohashi, Technologies on Continuous Casting - Direct Rolling, Fachberichte Hüttenpraxis Metallweiterverarbeitung, Vol. 23, No. 4, pp. 302-316, (1985).
- [3] H. Wiesinger, G. Holleis, K. Schwaha, H. Hirschmanner, Design of CC Machines for Hot Charging and Direct Rolling, McMaster Symposium on Iron and Steelmaking Proceedings, No. 13, pp. 42-73, (1985).
- [4] B. G. Thomas, J. K. Brimacombe, and I. V. Samarasekera, The Formation of Panel Cracks in Steel Ingots. A State of the Art Review. Part I--Hot Ductility of Steel, Iron and Steel Society Transactions, Vol. 7, 1986, pp. 7-20.
- [5] I. V. Samarasekera, J. K. Brimacombe, Thermal and Mechanical Behaviour of Continuous-Casting Billet Moulds, Ironmaking and Steelmaking, No. 1, pp. 1-15, (1982).
- [6] I. V. Samarasekera, J. K. Brimacombe, The Thermal Field in Continuous Casting Moulds, Canadian Metallurgical Quarterly, Vol. 18, pp. 251-266, (1979).
- [7] K. P. Michalek, Modeling of In-Mold Heat Transfer in Continuous Casting of Steel, Masters Thesis, University of Illinois, (1985).
- [8] K. Ho, R. D. Pehlke, Metal-Mold Interfacial Heat Transfer, Met. Trans, Vol. 16B, pp. 585-594, September (1985).
- [9] J. E. Kelly, K. P. Michalek, T. C. O'Conner, B. G. Thomas, J. A. Dantzig, Initial Development of Thermal and Stress Fields in Continuously Cast Steel Billets, Met Trans B, (in print).

- [10] K. E. Blazek, Mold Heat Transfer During Continuous Casting, Parts I-X, Iron and Steelmaker, Vol. 14, No. 9 - Vol. 15, No. 6, (Sept. 1987- June 1988).
- [11] H. Jacobi, G. Kaestle, K. Wünnunberg, Heat Transfer in Cyclic Secondary Cooling During Solidification of Steel, Ironmaking and Steelmaking, Vol. 11, No. 3, pp.132-145, (1984).
- [12] E. Mizikar, Spray Cooling Investigation for Continuous Casting of Billets and Blooms, Iron Steel Engineer, Vol. 47, pp. 53-60, (1970).
- [13] M. P. Ovcharenko, S. D. Razumov, V. I. Lebedev, D. P. Evteev, Investigations of Parameters of Water-Air Secondary Cooling in Continuous Casting Installations, Steel in the USSR, Vol. 16, pp. 19-21, January (1986).
- [14] J. K. Brimacombe, P. K. Agarwal, S. Hibbins, B. Prabhuker, L. A. Baptista, Spray Cooling in the Continuous Casting of Steel, Continuous Casting Vol. 2, ISS-AIME, pp. 109-123, (1984).
- [15] B. Krüger, I. W. Rahmfeld, I. P. Voss-Spiker, Dry Casting of Slabs on Bow-Type Continuous Casters, World Steel & Metalworking, Vol. 9 pp. 171-177, (1988).
- [16] T. Kohno, T. Shima, T. Kuwabara, T. Yamamoto, M. Wake, A. Tsuneoka, Improvement of Surface Cracks by Air-Water Mist Cooling in Strand Casting, Continuous Casting Vol. 2, ISS-AIME, pp. 133-137, (1984).
- [17] H. A. Wiesinger, K. L. Schwaha, O. Kriegner, Mathematical Analysis of the Solidification Process in High Speed Continuous Casting of Steel, Continuous Casting of Steel, Second PTC, pp. 86-94, (1981).
- [18] A. Etienne, B. Mairy, Heat Transfer in Continuously Cast Strands, CRM Publication No. 55, pp. 3-13, November (1979).
- [19] S. Kojima, T. Matsukawa, H. Ishihara, N. Takashiba, J. Yamasaki, M. Maeda, Heat Flow Analysis on Slab Surface in Secondary Cooling of Continuous Casting, Trans. of ISIJ, Vol. 20, No. 6, (1980).

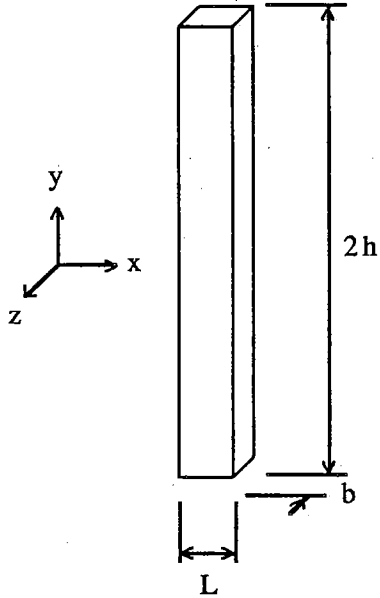
- [20] S. G. Hibbins, J. K. Brimacombe, Characterization of Heat Transfer in the Secondary Cooling System of a Continuous Slab Caster, Continuous Casting Vol. 2, ISS-AIME, pp. 139-151, (1984).
- [21] R. Davies, N. Blake, P. Campbell, Solidification Modelling - An Aid to Continuous Casting, 4th International Conference Continuous Casting (ICC), Preprints 2, pp. 645-654, (1988).
- [22] E. Upton, T. R. Satya Rao, P. Dauby, R. Knechtges, Physical Metallurgy and Mathematical Modelling as Tools for Continuous Casting Optimization at LTV Steel, 29th Mechanical Working and Steel Processing Proceedings, ISS-AIME, Vol. 25, pp. 317-325, (1987).
- [23] J. Savage, W. H. Pritchard, The Problem of Rupture of the Billet in the Continuous Casting of Steel, Journal of Iron & Steel Inst., Vol. 178, pp. 269-277, (1954).
- [24] M. Uehara, I. V. Samarasekera, J. K. Brimacombe, Mathematical Modelling of Unbending of Continuously Cast Steel Slabs, Ironmaking and Steelmaking, Vol. 13, No. 3, pp. 138-153, (1986).
- [25] B. Barber, B. A. Lewis, B. M. Leckenby, Finite Element Analysis of Strand Deformation and Strain Distribution in Solidifying Shell During Continuous Slab Casting, Ironmaking and Steelmaking, Vol. 12, No. 4, pp. 171-175, (1985).
- [26] S. Forrest, K. Wilson, The Requirements for Hot Charging Cast Slabs at Stelco's Lake Erie Works, Iron & Steelmaker, Vol. 12, No. 10, pp. 28-34, (1985).
- [27] Y. Maehara, K. Yasumoto, H. Tomono, K. Gunji, Surface Cracking Mechanisms of Low Carbon Low Alloy Steel Slabs, CONCAST Workshop on Slab Casting, Kashima, Japan, May, (1987).
- [28] H. Suzuki, S. Nishimura, S. Yamaguchi, Physical Simulation of the Continuous Casting of Steels, CANMET Symposium, Canada, May, (1988).

- [29] CONCAST Technology Technical Note, Bloom Surface Defects after Rolling in Connection with Hot Charging, CONCAST Service Union AG, Wo/FR177 - 60.361 September, (1984).
- [30] B. G. Thomas, I. V. Samarasekera, J. K. Brimacombe, Mathematical Model of the Thermal Processing of Steel Ingots: Part 1. Heat Flow Model, Met. Trans, Vol. 18B, pp. 119-130, March (1987).
- [31] B. G. Thomas, I. V. Samarasekera, J. K. Brimacombe, Mathematical Model of the Thermal Processing of Steel Ingots: Part 2. Stress Model, Met. Trans, Vol. 18B, pp. 131-145, March (1987).
- [32] B. G. Thomas, Investigation of Panel Cracking Formation in Steel Ingots Using Mathematical and Physical Models, Ph. D. Thesis, University of British Columbia, Vancouver, BC, Canada, (1985).
- [33] A. W. D. Hills, Journal of Iron Steel Institute, Vol. 203, pp. 18-26, (1965).
- [34] B. G. Thomas, I. V. Samarasekera, J. K. Brimacombe, Comparison of Numerical Modeling Techniques for Complex, Two-Dimensional, Transient Heat-Conduction Problems, Met. Trans, Vol. 15B, pp. 307-318, June (1984).
- [35] O. C. Zienkiewicz, The Finite Element Method, McGraw-Hill Company, London, 3rd Ed. (1977).
- [36] R. D. Cook, Concepts and Applications of Finite Element Analysis, John Wiley and Sons, New York, 2nd Ed. (1981).
- [37] L. J. Segerlind, Applied Finite Element Analysis, John Wiley and Sons, New York, 2nd Ed. (1984).
- [38] D. L. Logan, A First Course in the Finite Element Method, PWS Engineering Publishers, Boston, (1986).

- [39] A. Mendelson, PLASTICITY: Theory and Application, R. E. Krieger Publishing, New York, (1983).
- [40] B. A. Boley, J. H. Weiner, Theory of Thermal Stresses, R. E. Krieger Publishing, Malabar, Florida, (1985).
- [41] I. Saucedo, Inland Steel, private correspondence, (1987).
- [42] J. A. Azzi, Preliminary Steps in the Development of a 3-D Thermal-Stress Model of Continuous Casting, Masters Thesis, University of Illinois, (1988).
- [43] F. P. Incropera, D. P. DeWitt, Fundamentals of Heat Transfer, John Wiley and Sons, New York, pp. 441-442, 445, (1981).
- [44] R. E. Smelser, O. Richmond, Constitutive Model Effects on Stresses and Deformations in a Solidifying Circular Cylinder, 4th Engineering Foundation Conference on Modeling of Casting and Welding Processes, Palm Coast, FL, April, (1988).

APPENDIX A: Analytical Solution to Verification Problem

Analytical Solution to the Thermally Loaded Beam Problem [4]



Material Properties

$$E = 200 \text{ GPa}$$

$$\nu = 0.25$$

$$\alpha = 12 \text{ e-6/}^\circ\text{C}$$

$$A = 1 \text{ e-13 /Pa s}$$

Geometry

$$h = 0.01\text{m}$$

$$L = 0.0008\text{m}$$

$$b \ll h$$

Stress State

Plane Stress

The temperature history is as follows:

$$t > 0 \quad T = a_0 + a_1 y + a_2 y^2 + a_3 y^3 \quad (\text{E1})$$

Initial Elastic Solution

From Boley and Weiner [40], pp. 279-281:

$$\sigma_z = 0 \quad (\text{E2})$$

$$\sigma_y = 0 \quad (\text{E3})$$

$$\tau_{xy} = 0 \quad (\text{E4})$$

$$\sigma_x = -\alpha E T + \frac{\alpha E}{2h} \int_{-h}^h T dy + \frac{3\alpha E}{2h^3} y \int_{-h}^h T y dy \quad (\text{E5})$$

Using the standard strain-stress relationships:

$$\epsilon_x = \frac{1}{E} [\sigma_x - \nu(\sigma_y + \sigma_z)] + \alpha T \quad (E6)$$

$$\epsilon_y = \frac{1}{E} [\sigma_y - \nu(\sigma_z + \sigma_x)] + \alpha T \quad (E7)$$

$$\epsilon_z = \frac{1}{E} [\sigma_z - \nu(\sigma_x + \sigma_y)] + \alpha T \quad (E8)$$

these can be simplified to the following equations by substituting Eqs. E2- E5:

$$\epsilon_x = \frac{\alpha}{2h} \int_{-h}^h T dy + \frac{3\alpha}{2h^3} y \int_{-h}^h Ty dy \quad (E9)$$

$$\epsilon_y = \epsilon_z = (1 + \nu) \alpha T - \frac{\alpha \nu}{2h} \int_{-h}^h T dy + \frac{3\alpha \nu}{2h^3} y \int_{-h}^h Ty dy \quad (E10)$$

The displacements u and v may be derived from ϵ_x and ϵ_y by the following substitutions:

$$\epsilon_x = \frac{\partial u}{\partial x} \Rightarrow \partial u = \epsilon_x \partial x \quad (E11)$$

$$\epsilon_y = \frac{\partial v}{\partial y} \Rightarrow \partial v = \epsilon_y \partial y \quad (E12)$$

Finally, the following equations are formed:

$$u = x \left[\frac{\alpha}{2h} \int_{-h}^h T dy + \frac{3\alpha}{2h^3} y \int_{-h}^h Ty dy \right] \quad (E13)$$

$$v = (1 + \nu) \alpha \int_0^y T dy - \frac{\alpha \nu}{2h} y \int_{-h}^h T dy - \frac{3\alpha \nu}{4h^3} (x^2 + \nu y^2) \int_{-h}^h Ty dy \quad (E14)$$

Now, using the temperature distribution in Eq. E1 above, Eqs. E9,E10,E13,E14 reduce to the following after integration:

$$\epsilon_x = \alpha \left[a_0 + \frac{1}{3} a_2 h^2 + a_1 y + \frac{3}{5} a_3 h^2 y \right] \quad (E15)$$

$$\epsilon_y = \epsilon_z = \alpha v \left[a_2 (y^2 - \frac{1}{3} h^2) + a_3 y (y^2 - \frac{3}{5} h^2) \right] + \alpha T \quad (E16)$$

$$\sigma_x = \alpha E \left[a_2 (\frac{1}{3} h^2 - y^2) + a_3 y (\frac{3}{5} h^2 - y^2) \right] \quad (E17)$$

$$u = x \alpha \left[a_0 + \frac{1}{3} a_2 h^2 + a_1 y + \frac{3}{5} a_3 h^2 y \right] \quad (E18)$$

$$v = \alpha \left[(a_0 y + \frac{a_1}{2} y^2 + \frac{a_2}{3} y^3 + \frac{a_3}{4} y^4) + v (\frac{1}{2} a_1 y^2 + \frac{1}{3} a_2 y (y^2 - h^2) + \frac{1}{4} a_3 y^4) - v (x^2 + v y^2) (\frac{1}{2} a_1 + \frac{3}{10} a_3 h^2) \right] \quad (E19)$$

By choosing a problem where $u = \epsilon_x = 0$, then the coefficients a_0 , a_1 , a_2 , and a_3 can be related. By arbitrarily choosing $a_0 = 100.0$, and $a_1 = 3000.0$, then we have $a_2 = -3 \text{ e}6$, and $a_3 = -50 \text{ e}6$. These coefficients were used in the analytical solution to the verification problem.

Plastic Solution

The following are the stress-strain relations for plane stress:

$$\epsilon_x = \frac{\sigma_x}{E} + \alpha T + \epsilon_x^p \quad (E20)$$

$$\epsilon_y = \epsilon_z = -\sigma_x \frac{v}{E} + \alpha T + \epsilon_y^p \quad (E21)$$

Differentiation of Eqs. E20 and E21 yields:

$$\frac{d}{dt} \epsilon_x = \frac{1}{E} \frac{d}{dt} \sigma_x + \dot{\epsilon}_x^p \quad (E22)$$

$$\frac{d}{dt} \epsilon_y = -\frac{v}{E} \frac{d}{dt} \sigma_x + \dot{\epsilon}_y^p \quad (E23)$$

However, by using the Prandtl-Reuss Flow relations, the following substitutions can be made:

$$\epsilon_x^p = A\sigma_x \quad (E24)$$

$$\epsilon_y^p = -0.5 \sigma_x \quad (E25)$$

By inserting the boundary condition $\frac{d}{dt}\epsilon_x = 0$, the equations can be reduced to:

$$\sigma_x = \sigma_{x0} \exp[-EA(t - t_0)] \quad (E26)$$

$$\epsilon_x = \epsilon_{x0} \quad (E27)$$

$$\epsilon_y = \epsilon_z = \epsilon_{y0} + \frac{1}{2} \frac{\sigma_{x0}}{E} (1 - 2\nu)(\exp[-EA(t - t_0)] - 1) \quad (E28)$$

Now, the governing equations for the plastic strain must be formulated:

$$\epsilon_x^p = \int_{t_0}^t \epsilon_y^p dt = \int_{t_0}^t A\sigma_x dt = \frac{\sigma_{x0}}{E} (1 - \exp[-EA(t - t_0)]) \quad (E29)$$

$$\epsilon_y^p = \epsilon_z^p = -\frac{1}{2} \epsilon_x^p = \frac{\sigma_{x0}}{2E} (\exp[-EA(t - t_0)] - 1) \quad (E30)$$

Thus, all of the necessary equations have been formulated for the thermally loaded beam problem.

The following pages contain the results from the analytical solution and the model predictions for the problem discussed in the text. The first page is the X-stress for the bottom, center and top node of the beam. The second and third page are for the x-plastic strain and y-plastic strain, respectively.

X-Stress TOT

Time (sec)	SigX Bottom	SigX Center	SigX Top	CALC SigX B	CALC SigX C	CALC SigX T	% error in B	% error in C	% error in T
0	420.600000	-239.900000	510.900000	432.000	-240.000	528.000	-2.639	-0.042	-3.239
1	344.394000	-195.946000	418.527000	353.690	-196.500	432.290	-2.628	-0.282	-3.184
2	281.998000	-160.038000	342.891000	289.580	-160.880	353.930	-2.618	-0.523	-3.119
3	230.941000	-130.711000	280.973000	237.090	-131.710	289.770	-2.594	-0.758	-3.036
4	189.160000	-106.759000	230.280000	194.110	-107.840	237.250	-2.550	-1.002	-2.938
5	154.966000	-87.196700	188.774000	158.920	-88.291	194.240	-2.488	-1.239	-2.814
6	126.981000	-71.220000	154.787000	130.120	-72.287	159.030	-2.412	-1.476	-2.668
7	104.074000	-58.171600	126.954000	106.530	-59.183	130.200	-2.305	-1.709	-2.493
8	84.712200	-47.164800	103.419000	87.219	-48.455	106.600	-2.874	-2.663	-2.984
9	68.975800	-38.241300	84.278200	71.409	-39.672	87.278	-3.407	-3.606	-3.437
10	56.184300	-31.007000	68.710600	58.465	-32.480	71.457	-3.901	-4.535	-3.843
11	45.785300	-25.142200	56.046600	47.867	-26.593	58.504	-4.349	-5.456	-4.200
12	37.330100	-20.387500	45.743000	39.190	-21.772	47.899	-4.746	-6.359	-4.501
13	30.454100	-16.532800	37.358100	32.086	-17.826	39.216	-5.086	-7.255	-4.738
14	24.861500	-13.407800	30.533300	26.270	-14.594	32.108	-5.362	-8.128	-4.904
15	20.311800	-10.874300	24.976900	21.508	-11.949	26.288	-5.562	-8.994	-4.987
16	16.589700	-8.808720	20.427700	17.609	-9.783	21.522	-5.789	-9.958	-5.085
17	13.564100	-7.136320	16.726600	14.417	-8.010	17.621	-5.916	-10.903	-5.076
18	11.104000	-5.782220	13.714600	11.804	-6.558	14.427	-5.930	-11.825	-4.938
19	9.176020	-4.726630	11.351200	9.664	-5.369	11.812	-5.051	-11.964	-3.901
20	7.594060	-3.864450	9.410120	7.912	-4.396	9.671	-4.023	-12.088	-2.695

X Plastic Strain TOT

Time (sec)	EpsXp Bottom	EpsXp Center	EpsXp Top	CALC EpsXp B	CALC EpsXp C	CALC EpsXp T	% error in B	% error in C	% error in T
0	0.000000	0.000000	0.000000	0.000000	0.000000	0.000000	0.000	0.000	0.000
1	0.000386	-0.000220	0.000469	0.000392	-0.000218	0.000479	-1.396	1.131	-1.984
2	0.000702	-0.000400	0.000853	0.000712	-0.000396	0.000870	-1.391	1.020	-1.956
3	0.000961	-0.000546	0.001168	0.000975	-0.000541	0.001191	-1.385	0.918	-1.924
4	0.001173	-0.000666	0.001426	0.001189	-0.000661	0.001454	-1.370	0.825	-1.898
5	0.001347	-0.000764	0.001638	0.001365	-0.000759	0.001669	-1.364	0.740	-1.864
6	0.001489	-0.000844	0.001811	0.001509	-0.000839	0.001845	-1.347	0.661	-1.827
7	0.001606	-0.000909	0.001953	0.001627	-0.000904	0.001989	-1.334	0.591	-1.795
8	0.001704	-0.000965	0.002074	0.001724	-0.000958	0.002107	-1.133	0.710	-1.580
9	0.001785	-0.001009	0.002172	0.001803	-0.001002	0.002204	-1.016	0.758	-1.443
10	0.001850	-0.001045	0.002252	0.001868	-0.001038	0.002283	-0.942	0.753	-1.355
11	0.001903	-0.001075	0.002317	0.001921	-0.001067	0.002347	-0.900	0.729	-1.301
12	0.001947	-0.001099	0.002370	0.001964	-0.001091	0.002400	-0.873	0.687	-1.264
13	0.001982	-0.001118	0.002414	0.002000	-0.001111	0.002444	-0.866	0.631	-1.240
14	0.002011	-0.001134	0.002449	0.002029	-0.001127	0.002479	-0.863	0.583	-1.227
15	0.002035	-0.001146	0.002478	0.002052	-0.001140	0.002509	-0.863	0.524	-1.217
16	0.002054	-0.001157	0.002502	0.002072	-0.001151	0.002532	-0.860	0.481	-1.203
17	0.002070	-0.001165	0.002521	0.002088	-0.001160	0.002552	-0.855	0.434	-1.192
18	0.002083	-0.001172	0.002537	0.002101	-0.001167	0.002568	-0.857	0.397	-1.185
19	0.002093	-0.001177	0.002550	0.002112	-0.001173	0.002581	-0.874	0.336	-1.192
20	0.002102	-0.001181	0.002561	0.002120	-0.001178	0.002592	-0.880	0.295	-1.195

Time (sec)	Y plastic Strain TOT										
	EpsYp Bottom	EpsYp Center	EpsYp Top	CALC EpsYp B	CALC EpsYp C	CALC EpsYp T	% error in B	% error in C	% error in T		
0	0.000000	0.000000	0.000000	0.000000	0.000000	0.000000	0.000	0.000	0.000	0.000	0.000
1	-0.000193	0.000110	-0.000235	-0.000196	0.000109	-0.000239	-1.395	1.132	-1.983	1.132	-1.983
2	-0.000351	0.000200	-0.000427	-0.000356	0.000198	-0.000435	-1.388	1.020	-1.953	1.020	-1.953
3	-0.000481	0.000273	-0.000584	-0.000487	0.000271	-0.000596	-1.381	0.921	-1.922	0.921	-1.922
4	-0.000587	0.000333	-0.000713	-0.000595	0.000330	-0.000727	-1.370	0.828	-1.889	0.828	-1.889
5	-0.000673	0.000382	-0.000819	-0.000683	0.000379	-0.000834	-1.357	0.742	-1.854	0.742	-1.854
6	-0.000745	0.000422	-0.000906	-0.000755	0.000419	-0.000922	-1.341	0.665	-1.817	0.665	-1.817
7	-0.000803	0.000455	-0.000977	-0.000814	0.000452	-0.000994	-1.323	0.594	-1.780	0.594	-1.780
8	-0.000852	0.000482	-0.001037	-0.000862	0.000479	-0.001053	-1.123	0.713	-1.564	0.713	-1.564
9	-0.000892	0.000505	-0.001086	-0.000901	0.000501	-0.001102	-1.001	0.758	-1.425	0.758	-1.425
10	-0.000925	0.000523	-0.001126	-0.000934	0.000519	-0.001141	-0.927	0.758	-1.339	0.758	-1.339
11	-0.000952	0.000537	-0.001159	-0.000960	0.000534	-0.001174	-0.883	0.731	-1.273	0.731	-1.273
12	-0.000974	0.000549	-0.001185	-0.000982	0.000546	-0.001200	-0.858	0.690	-1.242	0.690	-1.242
13	-0.000991	0.000559	-0.001207	-0.001000	0.000555	-0.001222	-0.845	0.640	-1.215	0.640	-1.215
14	-0.001006	0.000567	-0.001225	-0.001014	0.000564	-0.001240	-0.837	0.590	-1.191	0.590	-1.191
15	-0.001018	0.000573	-0.001239	-0.001026	0.000570	-0.001254	-0.834	0.536	-1.182	0.536	-1.182
16	-0.001027	0.000578	-0.001251	-0.001036	0.000576	-0.001266	-0.834	0.492	-1.165	0.492	-1.165
17	-0.001035	0.000583	-0.001261	-0.001044	0.000580	-0.001276	-0.832	0.448	-1.148	0.448	-1.148
18	-0.001042	0.000586	-0.001269	-0.001050	0.000584	-0.001284	-0.826	0.406	-1.137	0.406	-1.137
19	-0.001047	0.000589	-0.001276	-0.001056	0.000587	-0.001291	-0.837	0.351	-1.149	0.351	-1.149
20	-0.001051	0.000591	-0.001281	-0.001060	0.000589	-0.001296	-0.847	0.307	-1.145	0.307	-1.145

APPENDIX B: Location of rollers

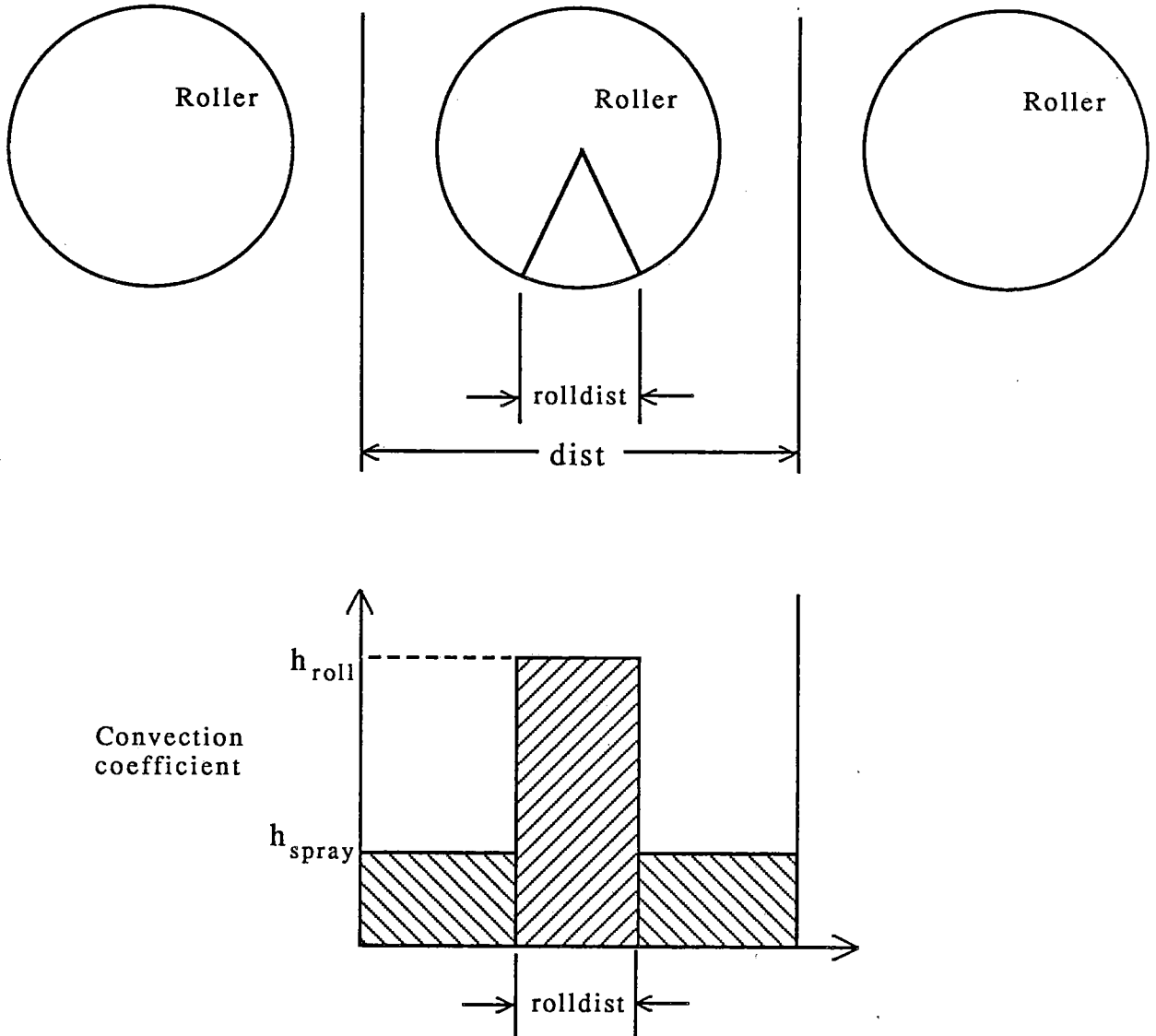
Roller No.	Distance of centerline from meniscus (m)	
1	0.770	Zone 1
2	1.038	
3	1.235	
4	1.432	
5	1.628	
6	1.825	Zone 2
7	2.022	
8	2.218	
9	2.415	
10	2.612	
11	2.860	
12	3.159	
13	3.459	
14	3.758	
15	4.058	
16	4.357	
17	4.657	
18	4.956	
19	5.226	
20	5.555	Zone 3
21	5.855	
22	6.154	
23	6.454	
24	6.753	
25	7.053	
26	7.352	
27	7.652	
28	7.951	
29	8.251	
30	8.550	
31	8.890	
32	9.270	
33	9.650	
34	10.030	
35	10.410	
36	10.790	
37	11.170	Zone 4
38	11.550	
39	11.930	
40	12.310	
41	12.690	
42	13.070	
43	13.450	

Roller No.	Distance of centerline from meniscus (m)	
44	13.881	
45	14.361	
46	14.843	
47	15.324	
48	15.805	
49	16.286	
50	16.767	
51	17.248	
52	17.729	
53	18.210	
54	18.691	
55	19.172	
56	19.653	
57	20.134	
58	20.615	Zone 5
59	21.096	
60	21.577	
61	22.058	
62	22.539	
63	23.020	
64	23.501	
65	23.982	
66	24.463	
67	24.944	
68	25.425	
69	25.906	
70	26.387	
71	26.868	
72	27.349	
73	27.830	

APPENDIX C: Determination of roll contact

Explanation of roller boundary condition

Objective: Determine the heat transfer coefficient due to the roller, knowing the fraction of total heat extracted by the roller and the water spray.



where: $\text{dist} = \frac{\text{Total length of zone}}{\text{Number of rollers in zone}}$

$$\text{rolldist} = (2)(\pi)(\text{Roller radius})\left(\frac{\text{Degrees of contact}}{360^\circ}\right)$$

h_{roll} = heat transfer convection coefficient for rollers

h_{spray} = heat transfer convection coefficient for sprays

Performing a heat balance in one roll "cycle",

$$h_{\text{spray}} (\text{dist} - \text{rolldist}) + h_{\text{roll}} (\text{rolldist}) = h_{\text{ave}} (\text{dist})$$

$$\begin{array}{ccc} \text{A (spray part)} & \text{B (roll part)} & \text{C (total)} \end{array}$$

But we know from the percentages of heat removed by the rollers and by the sprays from the literature [19]:

$$B = (\text{fracroll}) C$$

$$A = (1 - \text{fracroll}) C$$

$$C = A + B$$

where fracroll is the fraction of heat removed by the roller. By manipulating these equations, this yields:

$$A = (1 - \text{fracroll})(A + B)$$

$$A - A(1 - \text{fracroll}) = B(1 - \text{fracroll})$$

$$A(\text{fracroll}) = B(1 - \text{fracroll})$$

$$B = A \left(\frac{\text{fracroll}}{1 - \text{fracroll}} \right)$$

Plugging in:

$$(h_{\text{roll}})(\text{rolldist}) = (h_{\text{spray}})(\text{dist} - \text{rolldist}) \left(\frac{\text{fracroll}}{1 - \text{fracroll}} \right)$$

$$\therefore h_{\text{roll}} = (h_{\text{spray}}) \left(\frac{\text{dist} - \text{rolldist}}{\text{rolldist}} \right) \left(\frac{\text{fracroll}}{1 - \text{fracroll}} \right)$$

APPENDIX D: Natural convection calculations

Natural convection calculations

Vertical wall

Churchill and Chu [35] recommend the following correlation for all ranges of the Rayleigh number, Ra :

$$Nu_L = \frac{\bar{h}L}{K} = \left\{ 0.825 + \frac{.387Ra_L^{1/6}}{[1 + (0.492/Pr)^{9/16}]^{8/27}} \right\}^2$$

Incropera and DeWitt [35] recommend the following for a surface facing up that is hotter than T_∞ :

$$Nu_L = \frac{\bar{h}L}{K} = 0.15 Ra_L^{1/3} \quad 10^7 \lesssim Ra_L \lesssim 10^{10}$$

Note: All properties are evaluated at $T_{film} = (T_s + T_\infty)/2$

$T_{surface}$ (°C)	T_{film} (°C)	β (K ⁻¹)	ν (m ² /s)	α (m ² /s)	K (W/mK)	Pr
500	262.5	1.8674e-3	43.604e-6	63.800e-6	42.972e-3	.68345
700	362.5	1.5736e-3	54.871e-6	79.916e-6	48.888e-3	.68661
900	462.5	1.3596e-3	73.972e-6	105.810e-6	54.175e-3	.69910

Also, characteristic lengths are needed:

For vertical plate: $L_c = 9.25" = 0.235m$

For horizontal plate: $L_c = 36.0" = 0.9144m$

Calculate h for each case:

1. $T_s = 500^\circ\text{C}$, $T_\infty = 25^\circ\text{C}$

Vertical wall : $Ra_L = 4.05935e7$

$$Nu_L = \frac{\bar{h}L}{K} = \left\{ 0.825 + \frac{.387Ra_L^{1/6}}{[1 + (0.492/Pr)^{9/16}]^{8/27}} \right\}^2$$

$$= 46.5406$$

$$\therefore \bar{h} = Nu_L \frac{k}{L} = (46.5406) \left(\frac{42.972e-3}{.235} \right) = 8.510 \text{ W/m}^2\text{K}$$

Vertical wall : $Ra_L = 4.05935e7$

$$Nu_L = 0.15 Ra_L^{1/3} = 200.591$$

$$\therefore \bar{h} = Nu_L \frac{k}{L} = (200.591) \left(\frac{42.972e-3}{.9144} \right) = 9.427 \text{ W/m}^2\text{K}$$

For radiation:

$$h_{rad} = \epsilon \sigma (T + T_\infty)(T^2 + T_\infty^2) \quad T \text{ in Kelvin}$$

$$= (0.8)(5.67e-8)(773 + 298)(773^2 + 298^2) = 33.342 \text{ W/m}^2\text{K}$$

Since $h_{conv} \approx 21\%$ of total, it is not negligible!

2. $T_s = 700^\circ\text{C}$, $T_\infty = 25^\circ\text{C}$

From similar calculations as above:

Vertical wall: $\bar{h} = 8.9403 \text{ W/m}^2\text{K}$

Horizontal wall: $\bar{h} = 9.7856 \text{ W/m}^2\text{K}$

For radiation:

$$h = 59.701 \text{ W/m}^2\text{K}$$

Now, $h_{conv} \approx 13\%$ of total

3. $T_s = 900^\circ\text{C}$, $T_\infty = 25^\circ\text{C}$

From similar calculations as above:

Vertical wall:	$\bar{h} = 8.6755$	$\text{W/m}^2\text{K}$
Horizontal wall:	$\bar{h} = 9.2838$	$\text{W/m}^2\text{K}$

For radiation:

$$h = 97.734 \text{ W/m}^2\text{K}$$

Now, $h_{\text{conv}} \approx 8\%$ of total

Because the results don't vary considerably from 500°C to 900°C , an average over the temperature range was assumed adequate.

Vertical wall:	$\bar{h} = 8.70$	$\text{W/m}^2\text{K}$
Horizontal wall:	$\bar{h} = 9.50$	$\text{W/m}^2\text{K}$

